Heterogeneity and crystalline defects at complex oxide interfaces

Kazuhiro Kawashima

Abstract

Complex transition metal oxides show a variety of fascinating physical properties such as Mott insulators, metal-insulator transitions, multiferroics, colossal magnetoresistance and high-temperature superconductivity as well as charge, spin and orbital ordering. This diversity of the properties is based on the strong correlation between charge, spin and orbital degrees of freedom of electrons in the 3d orbitals. The investigation of these complex oxides is important for understanding the collective phenomena and the fundamental mechanisms underlying in the strongly correlated electron systems, in addition, novel applications are also the intriguing aspects of the complex oxides. In this thesis, high temperature superconductor $YBa_2Cu_3O_{7-d}$ (YBCO) and colossal magnetoresistive ferromagnet $La_{1-x}Ca_xMnO_{3-\delta}$ (LCMO) thin films as well as heterostructures composed of them were investigated. The goal of this work is to understand a role of crystalline defects as represented by oxygen vacancies and interface heterogeneity indicating structural mismatches in terms of lattice constants and chemical compositions between adjacent layers in the complex oxides. The functional properties of the YBCO and LCMO compounds are sensitively influenced by the oxygen vacancies and the lattice strain, therefore this system is an appropriate candidate for that purpose. As a result, it was shown that the interface heterogeneity and the crystalline defects are interrelated with each other, and they play a crucial role in determination of the properties of these complex oxide thin films as well as the heterostructures of them. These consequences are not only a mandatory information to grab a precise picture of the YBCO/LCMO heterostructures, but also a fundamental understanding of the nature of the complex oxide thin films in the real system.

Contents

1 Introduction and motivation **1**

2 High T_C superconducting $YBa_2Cu_3O_{7-d}$ and ferromagnetic $La_{0.7}Ca_{0.3}MnO_3$ **7**

2.1 High temperature superconducting $YBa_2Cu_3O_{7-d}$ 7

2.2 Colossal magnetoresistive ferromagnetic $La_{0.7}Ca_{0.3}MnO_3$ 13

2.3 YBCO/LCMO Heterostructures 21

3 Sample preparation and analysis techniques **27**

3.1 Pulsed laser deposition and thin film growth 27

3.2 Reflection High-Energy Electron Diffraction 32

3.3 Atomic Force Microscope 38

3.4 X-ray diffractometry 39

3.5 Photoconductivity measurement 42

3.6 VSM SQUID magnetometry 44

3.7 AC susceptibility measurement 47

4 Results **49**

4.1 Interrelation of epitaxial strain and oxygen deficiency in $La_{0.7}Ca_{0.3}MnO_{3-\delta}$ thin films 49

4.1.1 Background 49

4.1.2 Experiments 50

4.1.3 Results and discussions 51

4.1.4 Summary of the section 77

4.2 Superconductivity in $YBa_2Cu_3O_{7-d}/La_{1-x}Ca_xMnO_3$ bilayers (x=0.3, 0.45, 0.55 and 0.8) 78

4.2.1 Overview of this section 78

4.2.2 Experiments 79

4.2.3 Results 81

4.2.4 Discussion 88

4.2.5 Summary of the section 93

4.3 Persistent photoconductivity in oxygen deficient YBCO/LCMO superlattices 94
4.3.1 Background of the photoconductivity in YBCO and LCMO 94
4.3.2 Sample preparation 100
4.3.3 Structural analysis 100
4.3.4 Persistent photoconductivity in oxygen deficient YBCO/LCMO superlattices 105
4.3.5 Summary of the section 115

5 Conclusion **116**

Acknowledgement **119**

Publication list **121**

Chapter 1

Introduction and motivation

Complex transition metal oxides display a variety of fascinating physical properties such as Mott insulators, metal-insulator transitions, multiferroics, colossal magnetoresistance and high-temperature superconductivity as well as charge, spin, and orbital ordering. The basis for the diversity of the properties is a nature of d electrons of the transition metals. In a free transition metal atom, the $3d$ orbitals are composed of five degenerated orbitals, namely, d_{xy}, d_{yz}, d_{zx}, $d_{\mathrm{x^2-y^2}}$ and $d_{\mathrm{3z^2-r^2}}$. These $3d$ orbitals have spatially-anisotropic distributions and are stretched in the specific crystallographic orientations. This anisotropy of the wavefunctions as well as strong on-site Coulomb interactions cause an interplay of electron conduction and localization in these compounds. In addition, a similarity in energy scales of underlying mechanisms such as Hund coupling, Jahn-Teller splitting, and crystal field splitting also supports their rich functionalities. According to these characteristics of d electrons, the transition metal oxides acquire a strong entanglement of the charge, spin, and orbital degrees of freedom, resulting in a rich electronic and magnetic phases.

The investigation of these complex oxides is important for understanding fascinating collective phenomena and the fundamental mechanisms underlying in the strongly correlated electron systems, in addition, novel applications are other intriguing aspects of the complex oxides [1,2]. The fact that the properties of the oxides are extremely sensitive to structural distortions and a shift of chemical compositions sheds light on a pathway to engineering novel functionalities. Among a wide range of crystalline structures of the complex transition metal oxides, extensive attention has been devoted to a specific family so-called perovskite oxides, whose chemical composition is denoted as ABO_3 where the A and B sites are metal cations, generally with smaller ionic radius

for B than A atom, and O is an oxygen atom. According to the choice of the A and B atoms, the average cation size and valence are influenced, giving rise to a various physical phenomena as well as a change of the functional properties. A contribution of the cation sizes is often parameterized by the Goldschmidt tolerance factor $t = (r_A + r_O)/\sqrt{2}(r_B + r_O)$, where r_A, r_B and r_O are the atomic radii of A, B cations and oxygen, respectively. The tolerance factor is an important parameter of the perovskite oxides, which has an impact on the physical properties [3].

Taking into account of strong correlation between charge, spin and orbital degrees of freedom, heterostructures composed of transition metal oxides is an unique stage to design new artificial materials whose electrical, magnetic and optical properties can be modified by a subtle manipulation of d electrons and orbital occupancy of them [4, 5]. When two complex oxides are put in touch with each other, charge transfer takes place due to differences in the chemical potentials of both oxides. Charge transfer induces electronic reconstruction at the interface, and possibly causes a new electronic phase. Epitaxial strain will also play a role at the interface between different compounds. Due to a strong coupling between charge, spin and orbital states in the complex oxides, the lattice strain not only influences the functional properties quantitatively but also causes the electronic and magnetic phase transitions. These consequences are based on a nature of the complex oxides, and motivate the research on the artificial heterostructures and their interfacial effects. In the following, the examples of the prominent interface phenomena at the complex oxides are going to be presented.

First example is induced conducting and even superconducting states at the interface of two insulating oxides; $SrTiO_3$ (STO) and $LaAlO_3$ (LAO). Both compounds are band insulators, however, when a LAO layer is deposited on a TiO_2 terminated STO substrate, the interface shows a metallic transport and even becomes superconducting below 0.3 K [6, 7]. The metallic state at the interface occurs when the LAO film thickness exceeds 3 unit cells [8]. There are several scenarios proposed to explain the origin of the conductive LAO/STO interface. One possible explanation is a charge accumulation driven by polar discontinuity at the interface [7]. This assumption called *polar catastrophe* scenario is based on a difference of the polarity in STO and LAO. STO is composed of two different stacking atomic layers, namely, SrO and TiO_2. The valence states are Sr^{2+}, Ti^{4+} and O^{2-}, therefore SrO and TiO_2 layers are neutral. On the other hand, LAO is composed of the LaO and AlO_2 layers. Taking account of the valence state of La^{3+} and Al^{3+}, LaO and AlO_2 layers have a charge of +1 e and -1 e, respectively, and these atomic layers are polar. When the LAO layer was deposited on the TiO_2 terminated STO substrate, the polar discontinuity takes

place between the $Ti^{4+}O_2^{2-}$ and $La^{3+}O^{2-}$ layers at the interface of STO and LAO. According to stacking of the atomic layers in LAO, an electric potential is promoted with the thickness of the LAO layer. To avoid the divergence of the electric potential, charge of -1/2 e is added to the TiO_2 layer at the interface. By this charge, the electric field in the LAO layer oscillates around zero and the electric potential remains finite. The transferred electrons enter into the Ti d orbitals at the interface, contributing on the metallic conductivity. Another possible explanation is based on a cation intermixing at the interface. It was shown in scanning transmission electron microscopy [9] and surface X-ray diffraction [10] that the STO/LAO interface is not chemically sharp, and there exists a La/Sr and Ti/Al intermixing between STO and LAO, resulting in a formation of a $(La_{1-x}Sr_x)TiO_3$ layer at the interface, which could be responsible for the conductive transport. Finally, the oxygen vacancies could also contribute to the conductivity at the interface. It is well-accepted that the conductivity shows a clear dependence on the deposition condition, especially on the oxygen pressure during the deposition of the LAO layer [11, 12]. For instance, a LAO layer with a thickness of 60 Å deposited on a STO substrate at an oxygen background pressure of 10^{-6} torr shows a sheet resistance of 10^{-2} $\Omega/\Box$ at a low temperature, and in the sample with the same structure deposited at 10^{-5} torr a sheet resistance reaches $\sim 10^2 - 10^3$ $\Omega/\Box$ [7]. The fact implicates that the oxygen vacancies are induced into the STO substrates depending on the oxygen pressure during growth, and they contribute as dopants. Yet these assumptions are waiting to be confirmed by the subsequent measurements, and the research on this system is in progress.

The next prominent example of the interface phenomena at the complex oxides is a long range proximity effect observed in the heterostructures composed of a high temperature superconductor $YBa_2Cu_3O_{7-d}$ (YBCO) with T_C of ∼92 K and a ferromagnetic half metal $La_{0.7}Ca_{0.3}MnO_3$ (LCMO) with Curie temperature $T_{Curie} \sim 270$ K [13]. This field was initially inspired by the discovery of $RuSr_2GdCu_2O_8$ as a ferromagnetic superconductor with a Curie temperature T_{Curie} higher than the superconducting transition temperature T_C [14]. YBCO/LCMO superlattices have been used as a model system to explore the interaction between superconductivity and ferromagnetism in oxide thin films. The research was supported by a successful fabrication of the YBCO/LCMO heterostructures, and immediately a large suppression of T_C in these structures was found [15–17]. This reduction of T_C is a consequence of competition between two antagonistic order parameters; superconductivity in YBCO and ferromagnetism in LCMO, indicating a robust interplay at the YBCO/LCMO interface. The successive experiments revealed fascinating features taking place at the YBCO/LCMO interfaces, such as

extremely long range lattice proximity effect [18], long range spin charge transfer [15,19,20] and spin-polarized quasiparticle transfer [21,22], possible contribution due to exotic spin triplet superconductivity [23,24] and related mechanisms. Still intensive research efforts are being devoted to clarify the origin of the nature of the YBCO/LCMO long-range interplay. The YBCO/LCMO system is in the focus of study in this thesis.

The primary motivation of the study on the YBCO/LCMO heterostructures is to investigate interplay between two antagonistic states: superconductivity and ferromagnetism, in the strongly correlated oxide systems. In order to evaluate precisely the properties of the YBCO/LCMO heterostructures, one needs to understand the role of the crystalline defects and interface heterogeneity in addition to the interplay between superconductivity and ferromagnetism. It should be noted, however, that there is no comprehensible study concerning the role of the crystalline defects and interface heterogeneity in conjunction with an interrelation between them.

Crystalline defects are often classified according to its dimensionality. The zero-dimensional defects are point defects, which include missing ions from the lattice sites (vacancies), ions occupying interstitial crystallographic sites (interstitials) and substitutional impurities. The one-dimensional (line) defects are represented by dislocations. Dislocations indicate the termination of the crystalline atomic plane within a crystal. The two-dimensional defects include planar defects such as grain boundaries, antiphase boundaries and stacking faults, and the three-dimensional defects can indicate macroscopic defects such as precipitates. Among these crystalline defects, point defects as represented by the oxygen vacancies play an important role in the oxides. Oxygen vacancies influence the functional as well as structural properties in a convoluted way. In the strongly correlated oxide systems, oxygen vacancies not only modify quantitatively the physical properties such as resistivity, magnetic moment and phase transition temperatures, but also induces phase transitions, such as the insulator to superconductor transition in YBCO. This remarkable contribution of oxygen vacancies inspires to control the properties of the complex oxides by manipulating the oxygen vacancies [25]. Thus, the oxygen vacancies in the oxides are admitted as one of the central topics in the oxide physics.

Interface heterogeneity indicates a mismatch between two adjacent thin layers from the structural aspects including the lattice constants and the chemical compositions. The lattice constant mismatch, which causes an epitaxial lattice strain in the adjacent layer, is a key factor in respect of the thin film study. The deformation of the crystalline lattice influences the electron orbitals, resulting in the significant change of the

properties of the complex oxides due to the strong correlation between orbital, charge and spin degrees of freedom. Since, in many cases, the thin film fabrication is done by a hetero-epitaxial growth, which means, the thin film is grown on the substrate with a different chemical composition (just to name a few, YBCO grown on a $SrTiO_3$ substrate, LCMO grown on a $NdGaO_3$ substrate, etc.), the lattice mismatch between the thin film and the substrate should be always taken into account.

The interrelation between the lattice strain and the crystalline defects has been studied, and it is accepted that their contributions cannot be decoupled [26–28]. The lattice strain causes an elastic energy in the crystalline structure, and the elastic energy is going to be accommodated via an introduction of the crystalline defects to realize an equilibrium state of the system. This means, it is not likely that the thin films can be fabricated with the perfect crystalline structure without any defect, and the crystalline defects as represented by the oxygen deficiency are inevitable in the real oxide thin films. In conjunction with the importance of the oxygen vacancies in the complex oxides, the lattice strain as well as the interrelation between them is necessary to understand the real property of the oxide thin films. In the YBCO and LCMO compounds, their electronic and magnetic properties are sensitive to the oxygen deficiency and the lattice strain. Therefore these systems are appropriate candidates to investigate the interrelation between the crystalline defects and interface heterogeneity.

In the case of heterostructures of the oxide thin films, the situation becomes more complicate. Not only the mutual epitaxial strain between different layers and strain-related defects, but also the interface properties caused by charge transfer and electronic and magnetic proximity effects. Therefore, in order to understand the precise picture of the genuine properties of the complex oxide heterostructures, the following issues have to be considered simultaneously.

1. The role of the interfaces in terms of electronic and magnetic functionalities.

2. The role of the crystalline defects in complex oxides as represented by the oxygen deficiency.

3. The role of the interface heterogeneity indicating structural and chemical mismatches at the interface.

In this thesis, single YBCO and LCMO thin films as well as YBCO/ LCMO heterostructures have been studied [29–31]. They were characterized by several techniques such as a transport measurement including photoconductivity analysis, magnetometry, high-resolution X-ray diffraction measurement, mutual inductance, atomic force micro-

scope, etc. An ultimate goal of this work is to investigate the YBCO and LCMO thin films as well as heterostructures composed of them based on the guidelines described above, and extract the information about the interface heterogeneity and oxygen vacancies in the YBCO and LCMO system, in order to understand the details of the fabrication and the physics in these oxide thin films.

As a result, it was shown that the interface quality has an impact on the functionality at the interface and its mechanism, and that the interface heterogeneity in conjunction with the oxygen deficiency plays an important role in the YBCO and LCMO thin films as well as the heterostructures. These consequences are a mandatory information not only to understand the YBCO/LCMO heterostructure, but also to shed light on the nature of the oxide thin films in the practical system.

Chapter 2

High T_C superconducting $YBa_2Cu_3O_{7-d}$ and ferromagnetic $La_{0.7}Ca_{0.3}MnO_3$

2.1 High temperature superconducting $YBa_2Cu_3O_{7-d}$

A compound, Yttrium Barium Copper oxide ($YBa_2Cu_3O_{7-d}$ or YBCO in short), is a representative of high temperature superconducting cuprates. Here, the d is an oxygen deficiency, which can alter from 0 to 1, and $7-d$ indicates the oxygen content. YBCO is the most investigated compound in the high temperature superconducting cuprate family because YBCO has a simple structure compared to the other cuprates and it is uncomplicated to fabricate specimens via the classical sintering method.

The superconducting transition temperature (T_C) is dependent on the oxygen content. When the oxygen content changes, the superconductivity is influenced by two parameters: (1) the hole doping in a CuO_2 plane which is responsible for superconductivity in the compound and (2) the change in flatness of the CuO_2 plane due to a rearrangement of the atomic configuration. The electronic transport property varies from superconductor with the transition temperature of ~ 92 K for $d = 0.07$ to a Mott insulator for $d = 1$. Not only the functional properties, but also structural property is dependent on the d value. The lattice structures of YBCO for $d = 0$ and $d = 1$ are depicted in Fig.2.1. Fully oxygenated YBCO with $d = 0$ (the left figure in Fig.2.1) has an orthorhombic crystal structure. The YBCO unit cell is often denoted as a layered structure composed of several characteristic layers along the [001] axis. An yttrium atom is sitting at the center of the unit cell,

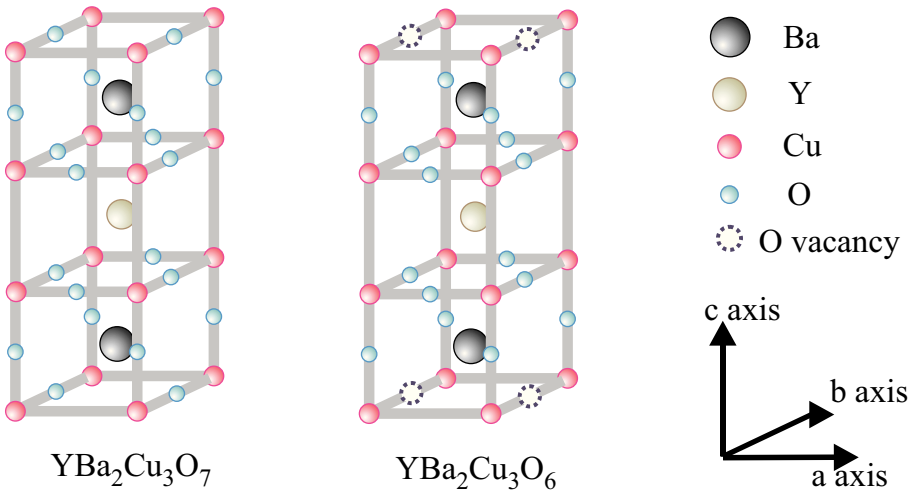

Figure 2.1: Unit-cell lattice structures of $YBa_2Cu_3O_7(d = 0)$ and $YBa_2Cu_3O_6(d = 1)$.

surrounded by two CuO_2 planes. At the top and the bottom of the unit cell, so-called CuO chain layers exist. In this layer, Cu and O atoms are aligned alternately along the b-axis. In-between the CuO_2 plane and CuO chain layer, a BaO layer is embedded. On the other hand, a completely deoxygenated YBCO where $d = 1$ has a tetragonal crystal structure (see the right figure in Fig.2.1). According to the deoxygenation, all the oxygen atoms in CuO chain layer disappear, and the vacant cite is called an oxygen vacancy. The oxygen atoms in the CuO_2 plains are stabler. The presence or absence of the oxygen atoms in the chain layers modifies the lattice constants. The lattice constants are a=3.82 Å, b=3.89 Å and c=11.68 Å for $d = 0$, and $a = b$ =3.86 Å and c=11.82 Å for $d = 1$ [32]. In reality, the oxygen deficiency d changes continuously between 0 and 1, and the lattice parameters as well. The oxygen content dependence of the lattice parameters are shown in Fig.2.2. In the orthorhombic phase, b-lattice parameter is larger than a-lattice parameter. This anisotropy occurs due to the existence of the oxygen atoms only in b-axis. Upon the decrease of d from 1, at $d \sim 0.6$, the structural transition from tetragonal to orthorhombic occurs.

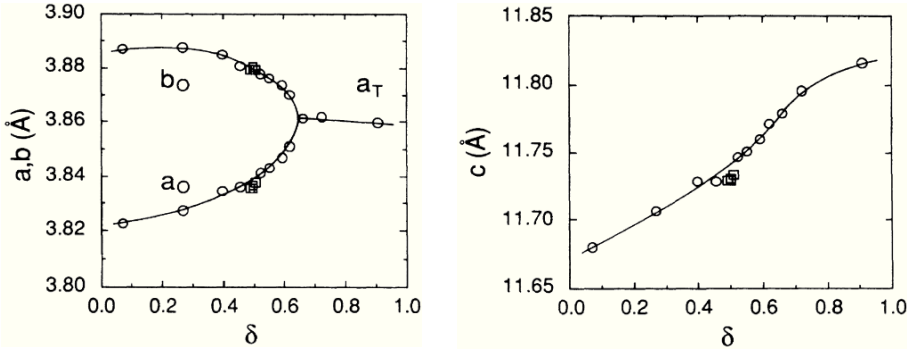

Figure 2.2: (From Ref. [32]) Oxygen deficiency dependence of the lattice parameters of YBCO. The a- and b-lattice parameters are shown in the left figure, where the subscripts O and T denote orthorhombic and tetragonal crystal structures. The right figure gives the c-lattice parameter.

The oxygen content influences not only the structural configuration but also the superconducting properties; $T_{\rm C}$ and the superfluid density. Here, a generic phase diagram of high-$T_{\rm C}$ superconducting cuprates as a function of temperature and doping level which indicates the hole concentration in the CuO_2 plane is given in Fig.2.3. The superconducting phase appears in dome-like shape. The maximum of $T_{\rm C}$ corresponds to the optimal doping level. In the high temperature region above $T_{\rm C}$, a metallic conductivity with a linear temperature dependence is observed. This phase is known as a strange metal phase because of its linearity of $R(T)$ [33–35]. The higher and lower doping levels are overdoped (OD) and underdoped (UD), respectively. As the doping level decreased from the optimal value, the superconductivity gets suppressed and finally the transition from a superconductor to an antiferromagnetic insulator occurs.

The high-$T_{\rm C}$ cuprates exhibits a pseudogap state which has been studied intensively. Pseudogap denotes the non-superconducting normal state which shows partially opened gap on Fermi surface. (For review of pseudogap, see [36, 37].) In general, pseudogap appears in the range of $T^* > T > T_{\rm C}$. T^* shifts to the high temperature according to the reduction of the hole concentration in CuO_2 plane as seen in Fig.2.3. This pseudogap phase of cuprates was first observed in NMR [38, 39], and then the existence of T^* was reported in a variety of measurements such as neutron scattering [40,41], electrical resistivity [42,43], Hall coefficient [44], specific heat [45], angle-resolved photoelectron spectroscopy (ARPES) [46]. The origin of pseudogap is still controversial. Currently

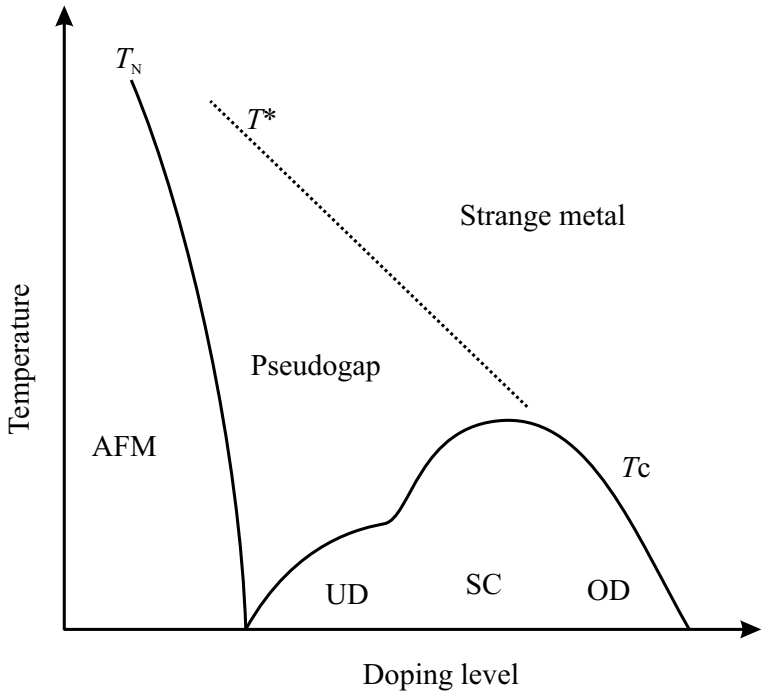

Figure 2.3: Generic phase diagram of YBCO as a function of temperature and doping level. SC denotes the superconducting phase. UD and OD mean underdoped and overdoped, respectively. AFM indicates an antiferromagnetic state, and T_{N} is Neel temperature which corresponds to an AFM to paramagnetic transition temperature. T^* shows the boundary between the strange metal and pseudogap phase.

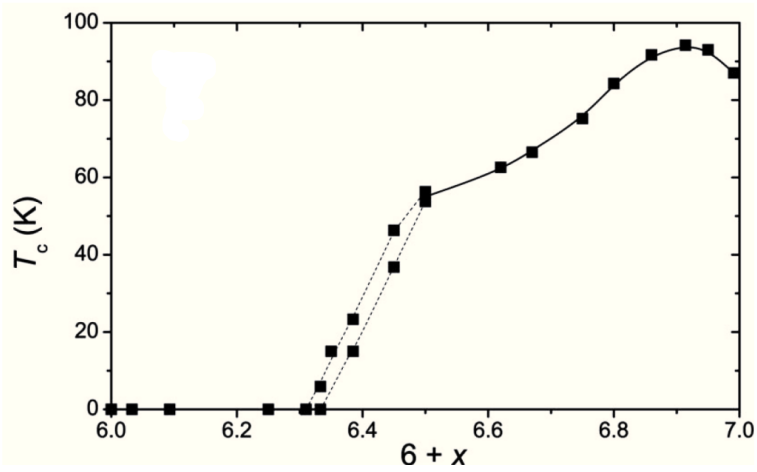

Figure 2.4: (From Ref. [47]) The oxygen content dependence on T_{C} in single crystal YBCO. Here, x is related to d according to $6 + x = 7 - d$

the main question is whether the pseudogap is a precursor of superconductivity or another phase. In the case that the pseudogap is a precursor of superconductivity, pseudogap is not a certain phase and is a crossover from the normal state to the superconducting state. In the case that pseudogap is a phase independent from superconductivity, quantum critical point for pseudogap phase should exist. Then the next question is whether pseudogap and superconductivity are supporting each other or competing orders. To unveil the origin of pseudogap might give us a hint about the mechanism of high temperature superconductivity, therefore pseudogap is one of the most attractive research topics in cuprates.

For YBCO, the doping level is controlled by the oxygen content. Fig. 2.4 shows the phase diagram for the YBCO compound as a function of the oxygen content, where x is related to d by $6 + x = 7 - d$. T_{C} reaches the highest value of 92 K at $x \sim 0.93$ ($d \sim 0.07$). This level of the oxygen content corresponds to the optimal doping level. Both the increase and decrease of the oxygen concentration from the optimal level suppress T_{C}. The further doping with $x > 0.93$ and less doping with $x < 0.93$ are overdope and underdope, respectively. The dependence of T_{C} vs. the oxygen content has a characteristic two plateau behavior. One plateau corresponds to the top of T_{C} vs. the oxygen content curve around $x = 0.93$. The second plateau appears in the underdoped region at $6.5 < 6 + x < 6.7$. The reason of the second plateau is presumably because at this oxygen content YBCO forms the ortho-II phase with alternating full and empty chains, and additional oxygen ions fill the empty chains, which makes a relatively small contribution to the hole

doping level [47]. The deviation existing at $0.3 < 6 + x < 0.5$ originates from the fact that T_C and the oxygen content are not unique correspondent because of a coexistence of ortho-I and ortho-II phases with this oxygen content. At less than ~ 6.3, superconductivity disappears and YBCO compound shows insulating behavior. From the viewpoint of electronic structure, CuO_2 plane and CuO chain layer play complementary roles with each other. CuO chain layer supplies hole to CuO_2 layer and the hole concentration in CuO_2 plane increases. Eventually superconductivity appears in CuO_2 plane. When $d > 0.7$, CuO chain layer cannot provide enough holes, and then the electronic transport property turns to an insulator.

YBCO belongs to type-II superconductors, which means Ginzburg-Landau parameter κ satisfies $\kappa = \lambda/\xi > 1/\sqrt{2}$, where λ and ξ are London penetration depth and coherence length, respectively. Type-II superconductor has the upper and lower critical fields H_{C1} and H_{C2} ($> H_{C1}$). When YBCO compound is exposed to an external magnetic field larger than H_{C1}, the magnetic field penetrates into superconducting YBCO in form of Abrikosov vortices, with the density proportional to the external field. Superconductivity is destroyed by the magnetic field more than H_{C2}. In YBCO, H_{C1} is 250 ± 20 Oe for a field perpendicular to a c-axis and 850 ± 40 Oe for a field parallel to c-axis, and H_{C2} are 674 T and 122 T for perpendicular and parallel, respectively [48]. The large anisotropy originates from a layered structure of the YBCO unit cell. Superconducting coherence length is $0.1 \sim 0.3$ nm in c direction and ~ 1.5 nm in the a-b plane [49]. Cooper pair has d-wave symmetry as a consequence of anisotropy of the electronic structure in conjunction with the lattice structure.

In a study of YBCO thin films, the thickness dependence of T_C is an important topic to understand what occurs near the interface. Fig.2.5 shows resistance vs. temperature curves for the YBCO films with different thicknesses grown on (001) STO substrates. In Fig.2.5, the YBCO thin film with the thickness of 24 Å is not superconducting, and the boundary in the thickness of superconducting and non-superconducting YBCO is ~ 25 Å. The reason of the existence of this critical thickness is attributed to disorder from the substrate [51]. A ultrathin YBCO layer sandwiched between insulating $PrBa_2Cu_3O_{7-d}$ layers shows the increase of T_C abruptly at ~ 15 Å [52]. The issue is still under debate in conjunction with the electronic reconstruction at the interface.

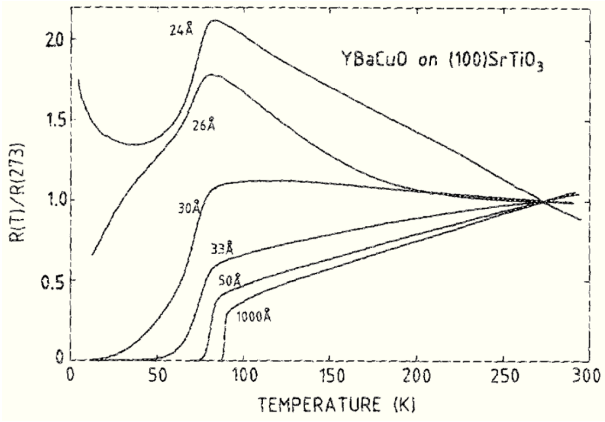

Figure 2.5: (From Ref. [50]) Normalized resistance R(T)/R(273 K) vs. temperature for YBCO films of different thicknesses on (001) STO. The accuracy of the thickness determination of the ultrathin films is about 10 %.

2.2 Colossal magnetoresistive ferromagnetic $La_{0.7}Ca_{0.3}MnO_3$

A Ca doped lanthanum manganite described as $La_{1-x}Ca_xMnO_{3-\delta}$ is another one of the representatives of strongly correlated oxide system. The undoped parent compound, $LaMnO_3$, is an antiferromagnetic Mott-insulator. By a partial substitution of trivalent La^{+3} ions by divalent Ca^{2+} ions, the compound shows several phase transitions. Depending on the concentration x, a characteristic property so-called colossal magnetoresistance (CMR) emerges [13,53]. Besides CMR effect, LCMO shows a couple of intriguing features, which originate from their intrinsic nature, namely, strong correlation between spin, charge, orbital degrees of freedom.

The lattice structure of LCMO has an orthorhombic crystal system with lattice parameters of $a_O = 5.4717$ Å, $b_O = 5.4569$ Å and $c_O = 7.7112$ Å [54]. A pseudo cubic approximation is applicable with a pseudo cubic lattice parameter $a \approx a_O/\sqrt{2} \approx b_O/\sqrt{2} \approx c_O/2 \approx 3.86$Å. A pseudo cubic perovskite structure is depicted in Fig. 2.6. A trivalent La^{+3} ion and divalent Ca^{2+} ion locate at the corners of the unit cell. Mn ion at around the center is surrounded by six oxygen ions, forming so-called 6-fold oxygen octahedron, MnO_6. The tolerance factor $t \equiv (r_A + r_O)/\sqrt{2}(r_B + r_O)$ influences the properties of perovskite manganites predominantly [3] as a consequence of strong correlation as shown in Fig.2.7. In the experiment shown in Fig.2.7, the carrier con-

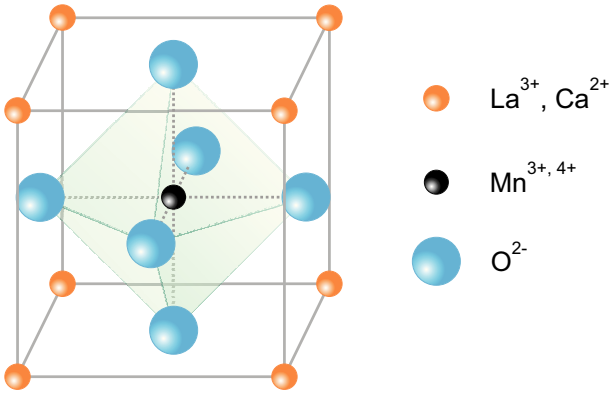

Figure 2.6: Unit-cell lattice structure of a pseudo cubic $La_{0.7}Ca_{0.3}MnO_3$.

centration was fixed and a direct relationship between the Curie temperature and the average ionic radius of the La site $\langle r_A \rangle$, which is varied by substituting different rare earth ions for La. Actually the change of $\langle r_A \rangle$ influences the magnetic order and the magnetoresistance property dramatically.

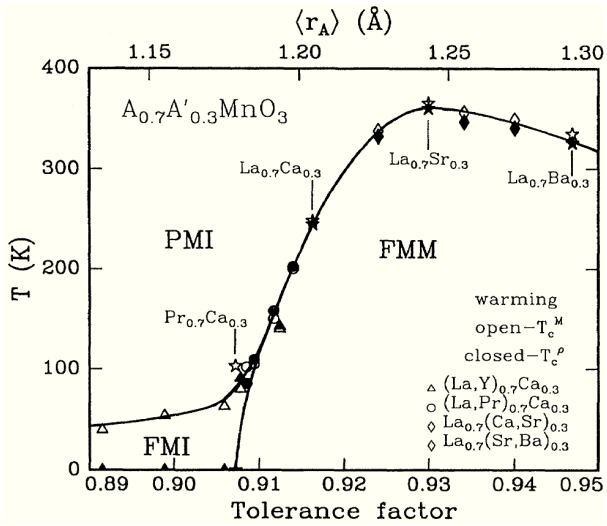

Figure 2.7: (Ref. [3]) Phase diagram of temperature vs. tolerance factor for the system $A_{0.7}A'_{0.3}MnO_3$, where A is a trivalent rare earth ion and A′ is a divalent alkali earth ion. Open symbols denote Curie temperature measured at 100 Oe in a heating process. PMI: paramagnetic insulator. FMI: ferromagnetic insulator. FMM: ferromagnetic metal.

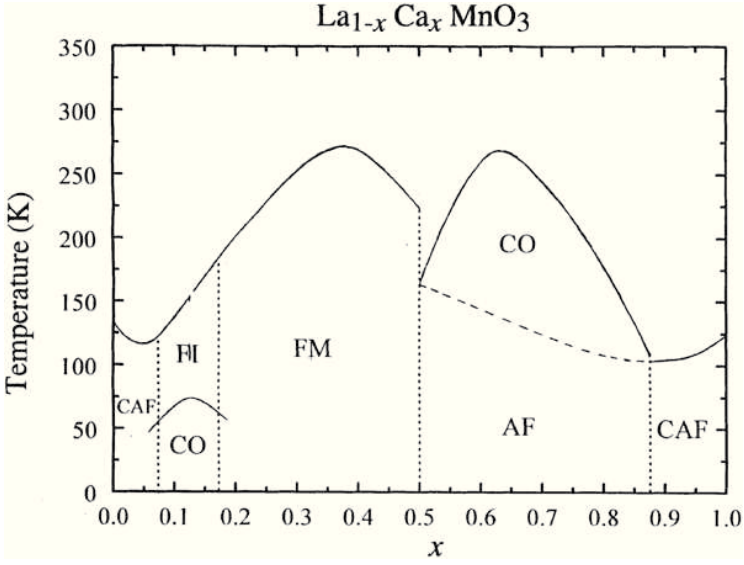

Figure 2.8: (From Ref. [55]) Phase diagram of LCMO as a function of doping x and temperature. FM: ferromagnetic metal, FI: ferromagnetic insulator, AF: antiferromagnetic, CAF: Canted AF, and CO: Charge/Orbital ordreing. FI and/or CAF could be a spatially inhomogeneous state with FM and AF coexistence.

Fig.2.8 shows a schematic phase diagram as a function of doping x and temperature presented in Ref. [55]. Both $LaMnO_3$ and $CaMnO_3$, corresponding x=0 and x=1, respectively, are antiferromagnetic insulators. However, a mixture of two parent phases realizes various characteristic phases. For around $0.1 < x < 0.2$, the phase is a ferromagnetic insulator and a charge ordered state. For $0.2 < x < 0.5$, LCMO shows paramagnetic insulator to ferromagnetic metal transition with a colossal magnetoresistance. The Curie temperature reaches as high as ~ 270 K in a bulk system. For $0.5 < x < 0.9$, a charge ordered antiferromagnetic phase appears.

In order to understand the nature of LCMO, one needs to consider electrons in d orbitals of the Mn ions. A free Mn ion has five degenerated $3d$ orbital states, namely, d_{xy}, d_{yz}, d_{zx}, $d_{x^2-y^2}$ and $d_{3z^2-r^2}$ orbitals. Mn^{4+} possesses three electrons on $3d$ orbital, and Mn^{3+} has four electrons. When the Mn ion is present in a crystalline lattice, the degeneracy of the $3d$ orbitals is lifted by the crystal field (static electric field) due to the neighboring O^{2-} ions. In case of MnO^6, five degenerated $3d$ orbitals split into three t_{2g} orbitals with lower potential and two e_g orbitals with higher potential (Fig.2.9). The splitting energy Δ_{CF} between t_{2g} and e_g

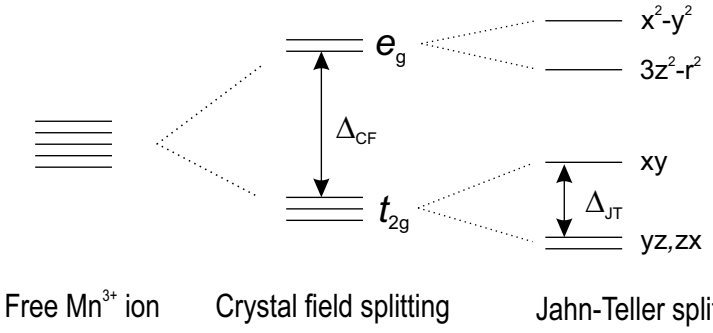

Figure 2.9: Schematic potential diagram of the $3d$ orbitals. The left figure is the degenerated $3d$ orbital states in free Mn ion. The center figure denotes the crystal field splitting to t_{2g} and e_g orbitals. The right figure shows Jahn-Teller splitting in Mn^{3+}.

is 1.5 eV [56]. In case of a Mn^{4+} ion, all of three electrons enter into the lower t_{2g} orbitals in order to form the lowest energy state. According to Hund coupling, which requires the parallel spin alignment by the exchange energy of 2.5 eV [56], the spins of the three electrons in t_{2g} orbitals align in a parallel way (ferromagnetic alignment). In case of a Mn^{3+} ion, there are four electrons in 3d orbitals and they are forced to align in one direction due to the Hund rule. Since Hund coupling energy 2.5 eV is smaller than the crystal field splitting energy, one electron is lifted to e_g level with same spin alignment as the other t_{2g} electrons. Since the e_g orbitals have strong correlation with O^{2-} ligand compared to the t_{2g} orbitals, the 3d orbitals introduce further splitting of the energy level. This splitting of the degeneracy and induced distortion of the orbital due to the interrelation between the ligand and the orbital electrons is called Jahn-Teller distortion. The Jahn-Teller splitting of the e_g level is in the range of $\Delta_{JT} = 0.5 \sim 0.6$ eV in various Mn^{3+} compounds [13].

The $d_{3z^2-r^2}$ orbital is stretched towards the neighboring O^{2-} ion, and it overlaps directly with the p orbital of the oxygen. Thus it enables the $d_{3z^2-r^2}$ electron to transfer from $d_{3z^2-r^2}$ of one Mn to an empty e_g orbital of another Mn site via oxygen p orbital. Importantly there is no spin-flip on the electron during the transfer from one Mn site to the other, namely the charge transfer is ferromagnetic coupling. This dynamics, which explains ferromagnetic conduction in the doped manganite, is referred to as double exchange mechanism originally proposed by Zener [57]. The double exchange mechanism is a key factor of the paramagnetic-insulator to ferromagnetic-metal transition. Note that the double exchange interaction occurs at $Mn^{4+} - O - Mn^{3+}$ configuration. On the other hand,

the overlap between Mn t_{2g} orbital and O p orbitals are small, and t_{2g} electrons tend to form a localized t_{2g} ion core. The electron transfer from t_{2g} core to the adjacent Mn ion leads to antiparallel exchange coupling, since only the antiparallel orbital is available for the coming electron. The probability of the e_g electron transfer from Mn^{3+} to the adjacent Mn^{4+} is defined by transfer integral $t = t_0 \cos(\theta/2)$ [58], where θ is the angle between the Mn spins and t_0 is the normal transfer integral depending on the spatial wave functions. The equation demonstrates that the double exchange interaction is most enhanced when the spin alignment of Mn ions are parallel.

Electronic and magnetic structure of LCMO is governed by two main mechanisms: a double exchange interaction and Jahn-Teller distortion. The double exchange interaction is responsible for the metallic conduction and ferromagnetic spin alignment. To the contrary, Jahn-Teller distortion localizes electrons and induces the insulating ground state. A competition of these mechanisms determines a resulting functional property of this compound. And, the most complexity occurs from the fact that these mechanisms are slightly or significantly affected by any single stimulus such as chemical doping, lattice strain, tolerance factor, crystalline defects, and so on. For instance, a multiple phase separation between ferromagnetic metallic, ferromagnetic insulating, and nonferromagnetic insulating region was observed in Mn nuclear magnetic resonance experiments [59]. It was shown that the localized charge is enhanced as the film thickness goes down. The authors attributed the phase separation to nanoscopic disorder caused by the interface [60] and/or strain. The strain-induced phase separation occurs in thin (2-6.5nm) compressive strained LCMO/LSAO [61]. A magnetic and/or electronic dead layer around the interface is often discussed. This fact makes LCMO so interesting, and so complicated to understand the intrinsic nature.

Colossal magnetoresistance (CMR) is a prominent property of LCMO. Fig.2.10 shows a standard CMR effect observed in LCMO thin film on a LSAT substrate. The resistance decreases drastically by applying an external magnetic field, and the resistant peak corresponding to insulator to metal transition shifts to a higher temperature. This phenomenon was initially found in $Nd_{0.5}Pb_{0.5}MnO_3$ [62], and it was revealed that CMR is a general feature seen in similar manganites. LCMO thin film was also shown to exhibit a large effect [53]. As a first approximation, CMR effect was explained by the enhancement of double exchange interaction. As shown before, the transfer integral of double exchange mechanism is expressed by $t = t_0 \cos(\theta/2)$. The external field decreases the difference of the angle between the neighboring Mn ions, thus the transfer inte-

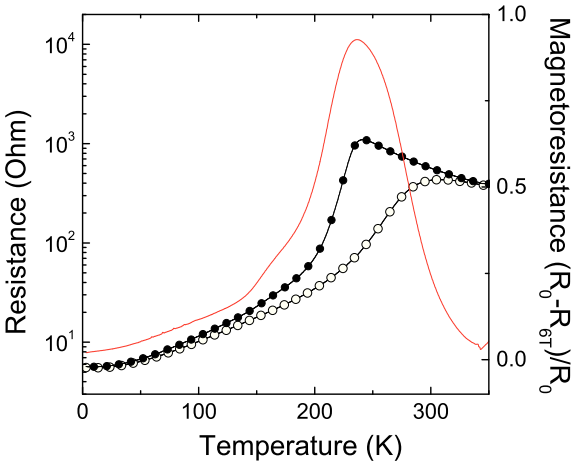

Figure 2.10: CMR effect observed in 1000 Å LCMO thin film on a LSAT substrate. The filled circle indicates the resistance vs. temperature without an external field. The open circle denotes the resistance vs. temperature under the external field of 6 tesla perpendicular to the plane. The solid line is a magnetoresistance ratio defined by $(R_0 - R_{6\mathrm{T}})/R_0$, where R_0 and $R_{6\mathrm{T}}$ are the resistance without and with the external field, respectively.

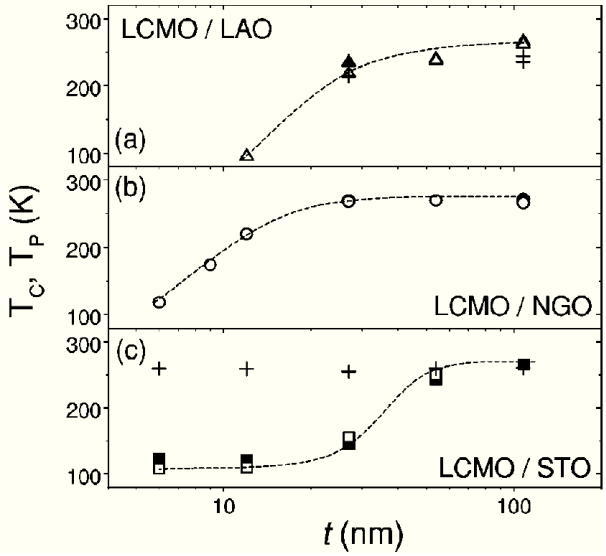

Figure 2.11: (From Ref. [66]) Thickness dependence of T_{Curie} (solid symbols) and of the metal to insulator transition temperature (open symbols) for the LCMO films grown on (a) LAO, (b) NGO and (c) STO.

gral is enhanced. The calculated resistivity taking account of the double exchange and Hunds coupling showed the dependence of ρ on the magnetization by the simple expression $\rho/\rho_0 = 1 - C(M/M_{\mathrm{Sat}})^2$ [63], where M and M_{Sat} are magnetic moment and saturation magnetization, respectively. C is the temperature-independent coefficient. The variable range hopping model was also applied to calculate the magnetoresistance ratio of LCMO [64]. The result described the magnetization dependence of the resistivity successfully by $\ln(\rho/\rho_\infty) = [T_0(1-(M/M_{\mathrm{Sat}})^2)/T]^{1/4}$. Another explanation could be the percolative conduction of the magnetically disordered clusters [65]. CMR effect indicates that the system possesses strong correlation between charge and spin degree of freedom.

The properties of the LCMO thin films depend on the thickness and used substrates. Fig.2.11 shows the thickness dependence of the Curie temperature and of the metal to insulator transition temperature for the LCMO films on the different substrates. On all substrates, T_{Curie} reduces as the thickness decreases. Magnetic ordering disappears in the LCMO on LAO when the thickness is less than 12 nm, where the LCMO films on the other substrates still show the transition. On the other hand, in the LCMO on the STO substrate, the reduction of T_{Curie} starts at the high temperature compared with the LCMO films on LAO and NGO

substrates. The LCMO on NGO substrate shows most robust and stable ferromagnetism in respect of the change of the thickness. The result clearly indicates the correlation between the thickness and the epitaxial strain, resulting from the strong correlation between lattice and orbital degrees of freedom.

2.3 YBCO/LCMO Heterostructures

The motivation on the YBCO/LCMO heterostructure was initially inspired by the discovery of $RuSr_2GdCu_2O_8$ as a ferromagnetic superconductor with a Curie temperature higher than the superconducting transition temperature [14]. YBCO/LCMO superlattices have been used as a model system to explore the interaction between superconductivity and ferromagnetism in oxide thin films. The research was supported by development of the fabrication methods of the YBCO/LCMO heterostructures, and immediately a large suppression of T_C in these structures was found [15–17]. This reduction contradicts an understanding that superconductivity of YBCO should not be sensitive to an adjacent layer because of its short superconducting coherence length ($0.1 \sim 0.3$ nm).

According to the comprehensive studies by using micro- and macroscopic analyses, several mechanisms have been proposed at the YBCO/ LCMO interface. First of all, one of the results from the transmission electron microscope measurement is shown in Fig.2.12. The specimen is a [8:6 nm]×20 YBCO/LCMO superlattice grown by pulsed laser deposition. The interfaces are atomically sharp and epitaxial, indicating a successful fabrication of the YBCO/LCMO superlattice structure. One can clearly distinguish each layer of YBCO and LCMO. In the image with low-resolution, the interfaces look more or less wavy. This wavy behavior of the interface is ascribed to a strain relaxation.

Based on the improved fabrication technology of the YBCO/LCMO heterostructures, the interface functionality was investigated in details. And it was revealed that there are several mechanisms participate in the physics at the YBCO/LCMO interface. One of the main participants is charge transfer where electrons move from LCMO to YBCO, conversely holes in YBCO are transferred to LCMO [17,67,68]. As a result, a hole concentration of CuO_2 plane in YBCO decreases, and then T_C is suppressed. Especially in case of a junction of YBCO and half metal $La_{0.7}Ca_{0.3}MnO_3$, the electrons injected to YBCO are fully spin-polarized. And a further suppression of superconductivity is expected to occur according to injection of spin-polarized carriers [15, 19, 20] and spin-polarized quasiparticles [21, 22]. The ferromagnetic-ordered spins transferred into YBCO scatter superconducting Cooper pairs and diminishes a concentration of them, because parallel spin-alignment is competing order to an antiparallel spin-combination which is necessary for a formation of a spin-singlet Cooper pair. The spin diffusion length was estimated as 10 nm [69] to 30 nm [70,71]. There is also a report suggesting a long range electron charge transfer from YBCO to LCMO [72], where surprisingly the direction of electron transfer is opposite to the

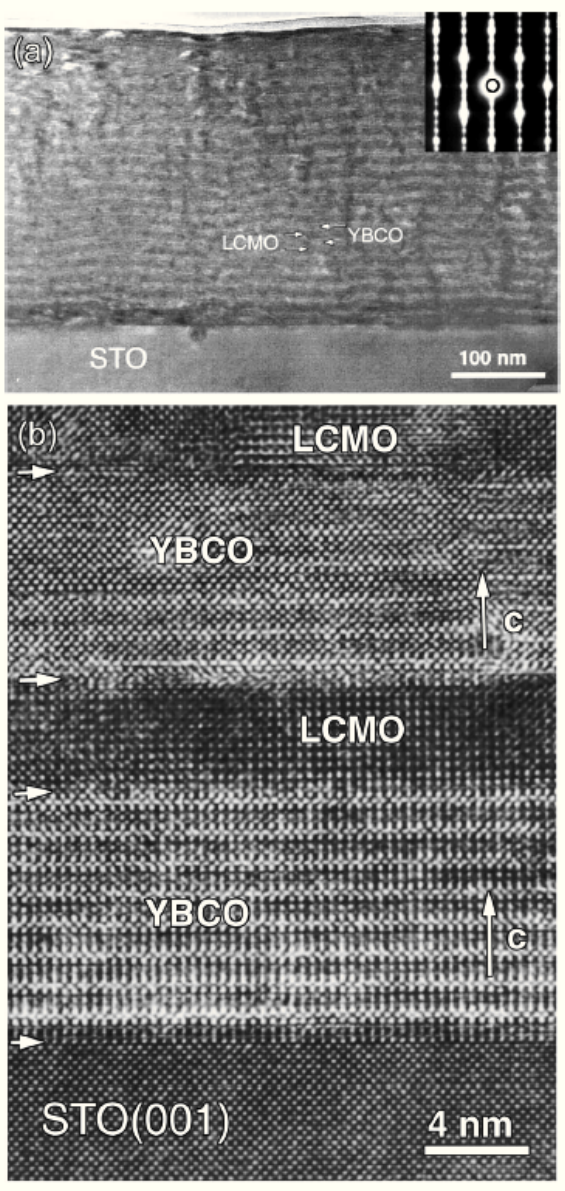

Figure 2.12: (From Ref. [17] (a) Low-resolution and (b) high-resolution transmission electron microscope and electron diffraction (shown in inset) images of a [8:6 nm]×20 superlattices.

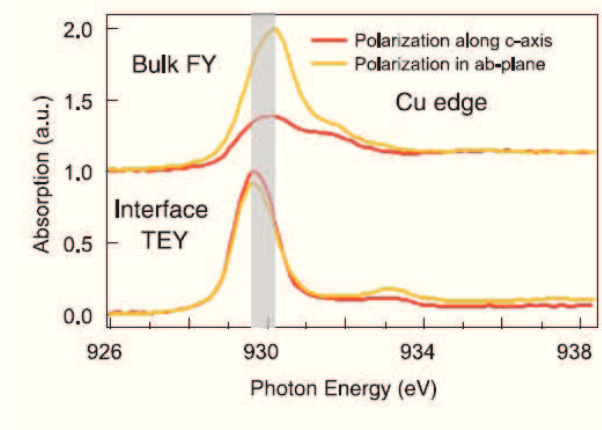

Figure 2.13: (From Ref. [74]) Normalized X-ray absorption spectra at the Cu L_3 absorption edge, taken in bulk-sensitive (FY, top panel) and interface-sensitive (TEY, bottom panel) detection modes with varying photon polarization as indicated in the legend.

previous one. A reason of the discrepancy might be attributed to a difference in microstructure and stacking configuration due to different sample deposition methods [67], or to a difference of an electronic transparency at the interface related to an interface roughness [72, 73].

The charge transfer mechanisms are closely related to an orbital reconstruction at the interface [74], where the transferred electrons modify an orbital occupancy at the interface, and magnetic proximity effect [75–77], where the electron transfer accompanies a redistribution of a magnetic moment around the interface. The orbital reconstruction was observed in a resonant X-ray absorption spectroscopy shown in Fig.2.13. Here, the absorption spectra gives information about the orbital occupancy. The absorption peak around 931 eV corresponds to the intra-ionic transition $2p^6 3d^9 \rightarrow 2p^5 3d^{10}$. The experiment was done in the total electron yield (TEY) mode which is sensitive to the buried interface, and in the fluorescence yield (FY) mode which is sensitive to the bulk. The absorption spectra in the bulk-sensitive FY mode shows a large difference between two different polarization of the X-ray. This is an indication that Cu $d_{3z^2-r^2}$ orbitals are occupied by electrons and there are holes in Cu $d_{x^2-y^2}$ orbitals. On the other hand, at the interface, TEY mode shows nearly same absorption spectra in both polarizations: along c-axis and in ab-plane, indicating the similar occupancy in $d_{3z^2-r^2}$ and $d_{x^2-y^2}$ orbitals in the Cu atom at the interface. The authors attributed this transition of the orbital occupancy from the bulk to the interface to the orbital reconstruction driven by the charge transfer.

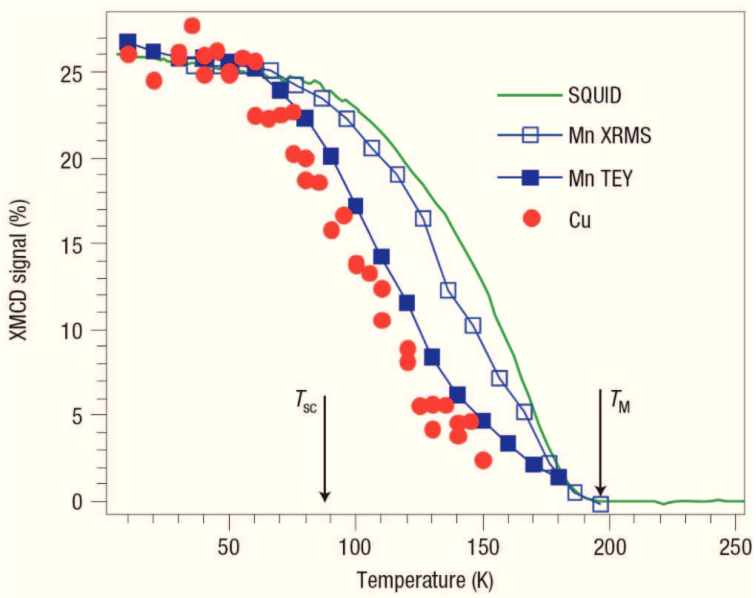

Figure 2.14: (From Ref. [76]) Temperature dependence of the XMCD signals of Cu and Mn compared with the bulk magnetization (simple line). All curves are normalized to the value of dichroism on Mn. TEY: surface-sensitive total electron yield mode. XRMS: bulk-sensitive X-ray resonant magnetic scattering mode.

The magnetism at the interface was also investigated in details, showing an intriguing result. Fig.2.14 gives the result of X-ray magnetic circular dichroism (XMCD) measurement. XMCD is a difference between absorption spectra for left- and right-polarized X-rays, defined by $I^+ - I^-$, where I^+ and I^- denote the absorption curves measured with photon helicity parallel and antiparallel to the magnetization direction. In Fig.2.14, the temperature dependence of the XMCD signal in Mn and Cu taken at the resonant $L_{2,3}$ edges are shown. The SQUID magnetometry and XMCD results obtained with surface-sensitive total electron yield mode and bulk-sensitive X-ray resonant magnetic scattering mode show the ferromagnetic transition with Curie temperature of 170 K. The issue is that, the Cu atom, which does not have any spin contribution, also exhibits the ferromagnetic signal in the same behavior of Mn atoms with Curie temperature of ∼170 K. The induced moment in Cu atoms was attributed to the Mn-O-Cu superexchange interaction across the interface.

Another intriguing aspect of the YBCO/LCMO interface is that the long range nature of the YBCO/LCMO interplay would be related to

an exotic superconducting state with spin triplet pairing induced by a superconductor/ferromagnet interface [23, 24]. Spin triplet Cooper pair has strong compatibility with ferromagnetic spin alignment. Therefore, the Cooper pair can penetrate by much longer scales than the spin singlet Cooper pair, and the long range proximity effect is expected to occur at the superconductor/ferromagnet interface. Unfortunately a clear evidence of this effect has not been observed.

Besides the observations mentioned above, there are more to be noted. An extremely long-range transfer of electron-phonon coupling in YBCO/LCMO superlattices was shown in a Raman scattering measurement [18]. The length scale of this effect was estimated as several tens of nanometers. This effect was attributed to a consequence of long-range Coulomb forces in conjunction with an orbital reconstruction at the interface. A giant magnetoresistance was observed in LCMO/YBCO/LCMO trilayer and superlattices [71], and an analogous structure [78]. The giant magnetoresistance is supposed to be induced due to a spin imbalance resulting from an antiparallel or parallel alignment of the ferromagnetic layers sandwiching YBCO layer in-between. The thermoelectric power measurement also showed completely different behavior in the YBCO/LCMO superlattices compared to the single YBCO and LCMO layers [79]. Fig.2.15 shows the measured Seebeck coefficients of the YBCO and LCMO single layers as well as the YBCO/LCMO superlattice. Whereas the YBCO and LCMO thin films exhibit negative Seebeck coefficients, which are in good agreement with data of bulk compounds, the superlattice sample shows positive Seebeck coefficient. The authors attributed the sign reversal of the Seebeck coefficient to a long-range electronic reconstruction nucleated at the YBCO/LCMO interfaces.

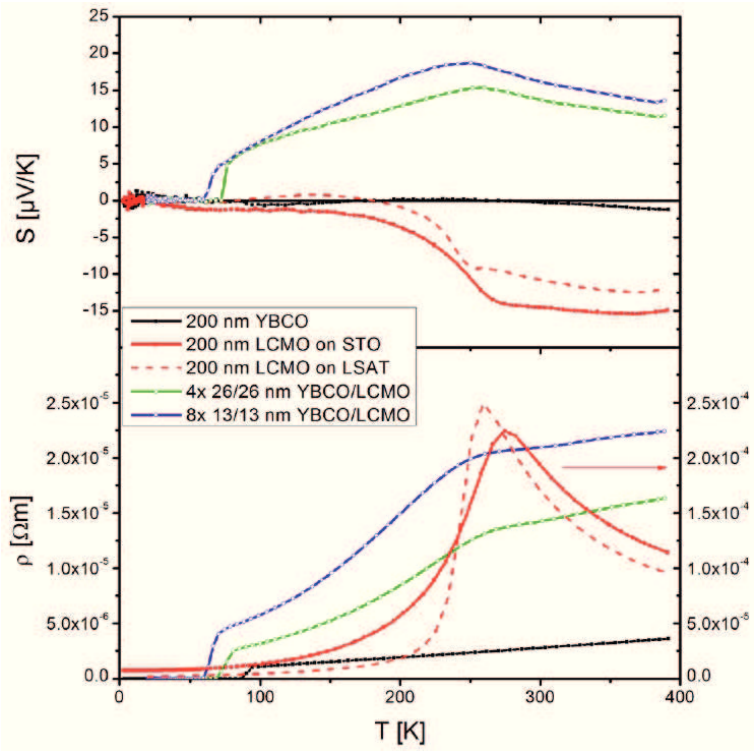

Figure 2.15: (From Ref. [79]) Temperature dependent Seebeck coefficient, S, and resistivity ρ, for different samples. The structures of the films are shown in the figure.

Advanced analyses are still being conducted to understand the microscopic mechanism of the long range interplay between high temperature superconductor YBCO and ferromagnetic half-metal LCMO. This could support our further understanding of high T_C superconductivity in conjunction with the relation between high T_C superconductivity and magnetism in oxides, and allow us to play with the charge, spin and orbital order via a controlled fabrication of an artificial material.

Chapter 3

Sample preparation and analysis techniques

3.1 Pulsed laser deposition and thin film growth

All thin film samples in this work were fabricated by pulsed laser deposition (PLD). Fig.3.1 gives a schematic layout of the PLD system. In a typical PLD process, a ceramic target is adopted as a source of ablation. A high energetic pulsed laser with the duration time of a few nano-seconds comes through a quartz glass window towards the target mounted on a rotatable holder in the chamber. The laser is focused on the target due to a collective lens on the laser path. In general, excimer laser of ArF (λ=193 nm), KrF (λ=248 nm) or Nd:YAG laser (λ=1064 nm) would be applied for the ablation of complex oxides. When the pulsed photon beam is absorbed by the target, the temperature at the surface immediately increases up to more than 5000 K within a few nano seconds [80] and the surface of the target is ablated. Due to the high density of the ablated species, the dense plasma, so-called a plume, with many species such as ablated molecules, atoms, ions, clusters, electrons and photons, is produced. The ablated materials are transferred to the substrate. They are deposited on the substrate, which is typically located perpendicular to the plume, and a thin film is formed on the substrate. A configuration of the thin film can differ as, for instance, amorphous or crystalline structure with single or multiple phases depending on the deposition condition. The functional property of the deposited compound is also significantly influenced by the deposition condition. According to the aimed compound and configuration of the thin film, the deposition is done in the ultra-high vacuum (UHV) or in a certain pressure with an appropriate type of gas, for instance, O_2, N_2O, NO_2, O_3 and so on.

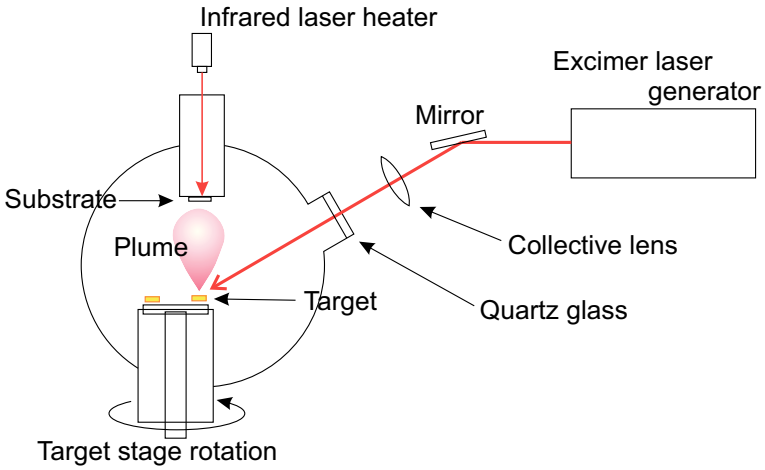

Figure 3.1: Layout of a pulsed laser deposition system.

Some characteristic features of the PLD method are listed in follows.

- In PLD process, it is possible to grow thin films with the same stoichiometry as the target.
- PLD is suitable to vary deposition speed by changing the laser fluency and the pulse frequency. This enables us to control thickness down to one unit-cell level.
- By using PLD method, one can fabricate different heterostructures and multilayers by changing the targets.
- The type of gas and the pressure during a sample growth can be easily altered for fabrication of the desired compound.
- A control of the variable parameters: the laser fluency, the laser pulse frequency, the type of gas and its pressure during a sample growth, enables us to make fine-tuning of a growth mode and the microstructure of the sample.
- PLD is suitable to evaporate complex oxides which have wide band gap and high melting point.

Typically the thin films are grown on crystalline substrates. The atomic arrangement of the film mimics the crystal structure of the substrate, and this growth is called *epitaxial* growth or *epitaxy*. There are two types of epitaxy; homoepitaxial and heteroepitaxial growth. In homoepitaxial growth, the deposited film has the same chemical formula as the substrate, and the crystalline structure of the film is well matched to

the crystalline structure of the substrate. In heteroepitaxial growth, the substrate and the deposited material are different compounds, accordingly the crystal structures of the film and the substrate are different. This lattice mismatch between the substrate and the film could accommodate by epitaxial misfit strain induced in the thin film. In the strongly correlated oxide systems, to vary epitaxial strain is one of the methods to engineer functional properties of the complex oxides.

The growth conditions, *i.e.* substrate temperature, gas pressure, laser fluency, distance between the target and the substrate, an area of focused laser beam on the target, lattice parameters of the substrate, etc., have to be fine-tuned to achieve necessary quality of the films and heterostructures. The choice of the substrate is one of the important factors that influence on the growth. The lattice parameters of the substrate should be close to those of the films. If the substrate has large lattice mismatch with the film, the crystalline structure of the grown film can be strongly defective and even amorphous. The substrate temperature and the gas pressure during growth are the other important parameters. For instance, Fig.3.2 shows the phase diagram of the YBCO compound, exhibiting the range of oxygen pressure and temperature, where the stable YBCO compound can be grown. An wrong deposition condition leads decomposition of YBCO compound to, for instance, $Y_2BaCuO_5 + CuO + BaCuO$ [81].

In addition, in order to optimize formation of a crystalline structure, a growth mode should be taken into account. Here some representative growth modes, which are experimentally well-recognized, are demonstrated in followings.

- Frank-van der Merwe (layer-by-layer) growth mode : In this growth mode, adatoms nucleate islands at the beginning of the deposition. As more adatoms reach to the substrate, they diffuse on the surface and migrate to spaces between islands. The islands get combined (coalescence), and finally a mono-layer is completed. The process of mono-layer formation is repeated for subsequent layers. In this manner, crystalline mono-layers are constructed on top of one another.

- Volmer-Weber (Island) growth mode : The beginning of the growth is same as layer-by-layer growth, that is, the growth starts from formation of islands. In this growth mode, however, the adatoms do not complete a mono-layer and they start forming new islands on the previous islands. This could happen, for instance, when the adatoms do not have enough mobility and/or when the deposition rate is too high. This growth mode is not favorable from the viewpoint of fabrication of flat thin films since the surface is expected

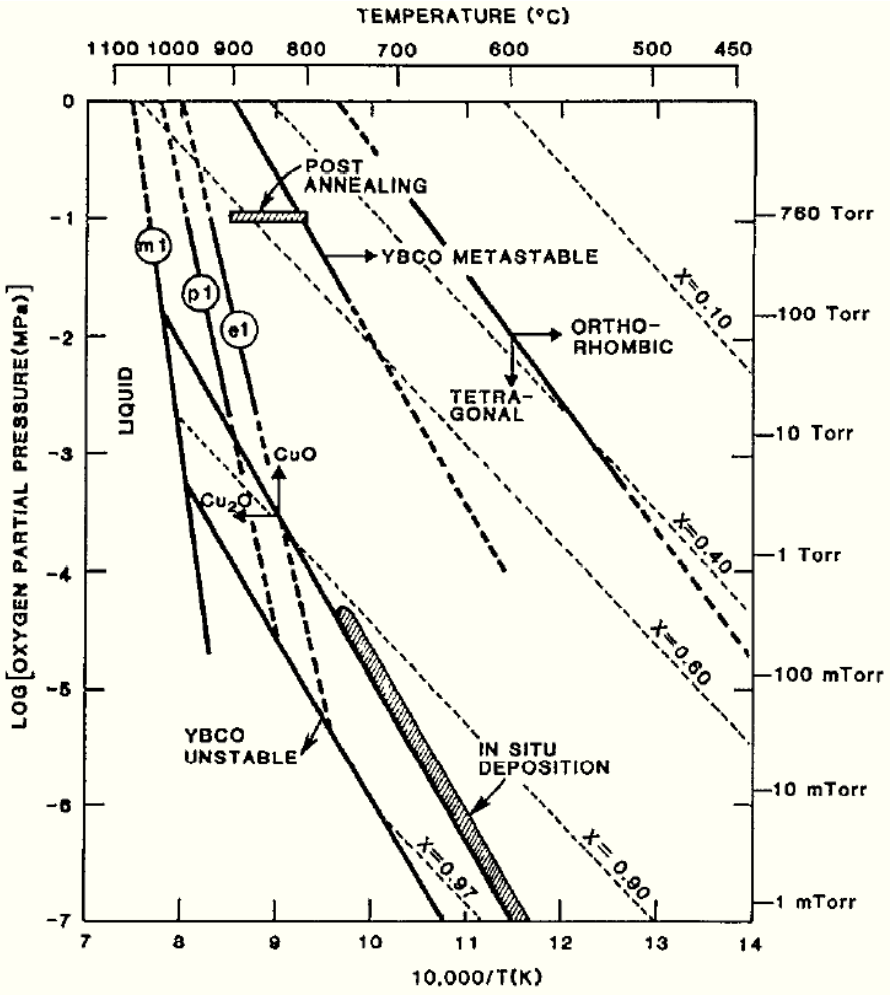

Figure 3.2: (From Ref. [82]) Phase stability diagram of YBCO compound.

to be rough due to 3-dimensional nature of island growth.

- Stranski-Krastanov (layer-plus-island) growth mode : This mode is defined as an intermediate between layer-by-layer growth mode and island one. In general, this growth mode occurs in case of heteroepitaxial growth where there is a lattice mismatch between the deposited material and the substrate. The initial growth is supposed to be layer-by-layer regime. However the elastic energy due to epitaxial strain rises as the film thickness increases. And in order to accommodate the growing elastic energy, nucleation of the islands begins from a certain thickness, so-called a critical thickness. Stranski-Krastanov growth is a quite important phenomenon to understand the physical and chemical properties between the substrate and the deposited compound.

- Step flow mode : In general, a surface of a crystalline substrate could possess atomic steps originating from a miscut of a crystalline substrate. A miscut substrate has atomically flat terraces between one step to the next step. The step flow mode happens when the adatoms diffuse through a terrace and settle down at the step edge without nucleating an island somewhere in the terrace. This mode occurs in case that the mobility of adatoms is high due to an elevated substrate temperature or that a width of terrace is narrow due to large miscut angle.

It is important to have sharp interfaces between different layers and well-defined layer thicknesses. In this sense, 2-dimensional growth modes such as layer-by-layer or step flow are highly recommended. The growth condition should be optimized according to an in-situ surface analysis and post analyses such as sample surface roughness and crystalline structural quality. A proper investigation will begin with those samples fabricated under a proper growth condition.

3.2 Reflection High-Energy Electron Diffraction

Reflection high-energy electron diffraction (RHEED) is a technique to characterize crystalline structure of a sample surface in real time. When an electron beam is incident to the surface of a crystalline sample, incoming electrons are scattered via electrons bound to the atom of the surface. The scattered electrons cause diffraction according to a periodicity of the crystal structure of the surface. Therefore the diffraction pattern enables us to understand the crystallography of the sample surface. In RHEED process, the glancing angle of the incident electron beam is set to 1∼5 degree. This configuration gives us an opportunity to combine the RHEED system with the PLD process, and then in-situ RHEED observation during growth is realized.

A schematic RHEED setup of our system is given in Fig.3.3. The electron beam is generated from a filament with a current of 2 Ampere. The electron beam is accelerated by 20 kV in our system. An atmospheric pressure around the RHEED filament needs to be less than 10^{-2} Pa, so that the filament avoids to be burned. On the other hand, the oxygen pressure in the main chamber where the sample locates could be elevated to 0.2∼0.5 mbar for the deposition of oxide thin films. Such a significant difference in the pressure between the main chamber and the filament part can be realized by applying a differential pumping system. In a differential pumping system, the beam path from the filament to the main chamber is separated by apertures into three parts. The diameters of the aperture on the filament side and on the main chamber side are 0.2 and 0.5 mm, respectively. Each part is pumped by a turbo pump separately, so that a differential background pressure is obtained. The electron beam passes through the first aperture, and the pathway is fine-tuned by an electromagnet coil, so-called a scan coil, towards the second aperture and then the sample surface within 1-2 unit cells. The electron beam is lead to the sample, and the electrons are diffracted at the sample surface with a glancing angle of 1∼5 degree. The diffracted electrons go to a fluorescence screen, and the pattern appearing on the screen is captured by a CCD camera.

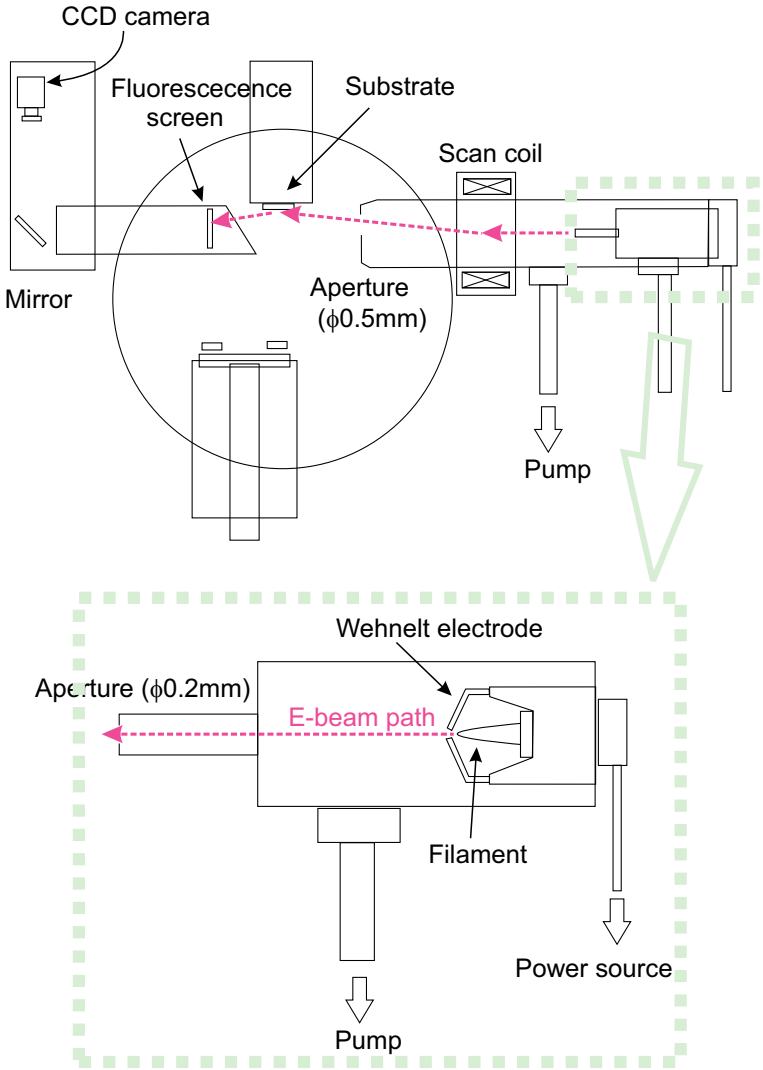

Figure 3.3: Schmatics of RHEED system with differential pumping configuration.

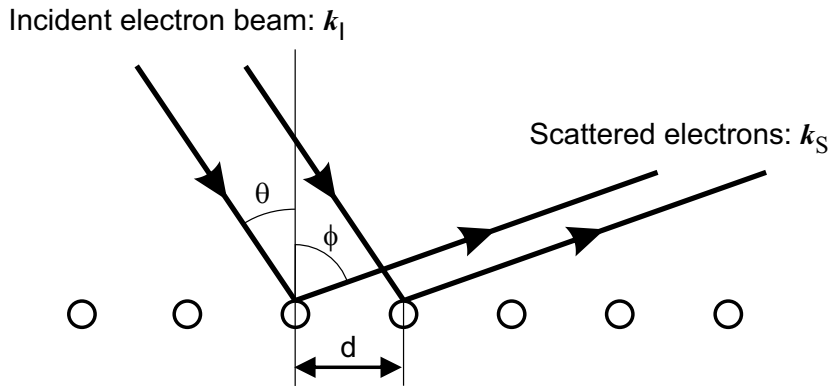

Figure 3.4: Electron diffraction from a one-dimensional atomic surface.

Theoretical background of RHEED is given here. Let us take a simplest example, that is, diffraction via one-dimensional atomic line depicted in Fig. 3.4. Incident and reflection angles are θ and ϕ, respectively. d is the atomic distance. $k_{\rm I}$ and $k_{\rm S}$ are wave number vectors of the incident wave and scattered wave, respectively. Since the constructive diffraction occurs when the path difference is equal to a multiple of wave length λ, the diffraction requires the following relationship.

$$d\sin\theta - d\sin\phi = n\lambda, \tag{3.1}$$

where n is an integer. Momentum conservation is given by

$$|\boldsymbol{k}_{\rm I}| = |\boldsymbol{k}_{\rm S}| = \frac{2\pi}{\lambda}. \tag{3.2}$$

Taking account of

$$|\boldsymbol{k}_{\rm I//}| = |\boldsymbol{k}_{\rm I}|\sin\theta, \tag{3.3}$$
$$|\boldsymbol{k}_{\rm S}| = |\boldsymbol{k}_{\rm S//}|\sin\phi, \tag{3.4}$$

and the reciprocal lattice vector, $d^* = 2\pi/d$, Eq.(3.1) becomes as follows.

$$|\boldsymbol{k}_{\rm I//}| - |\boldsymbol{k}_{\rm S//}| = nd^*. \tag{3.5}$$

The wave number $\boldsymbol{k}_{\rm I}$ is a wave number of the incident electron, which is a fixed parameter. Therefore this equation indicates a restriction on the wave number of the scattered electron, which is described as reciprocal lattice rods. On the other hand, momentum conservation between the initial and final states, Eq.(3.2), gives another restriction, which is described as so-called Ewald sphere. (In a case of one-dimensional atomic

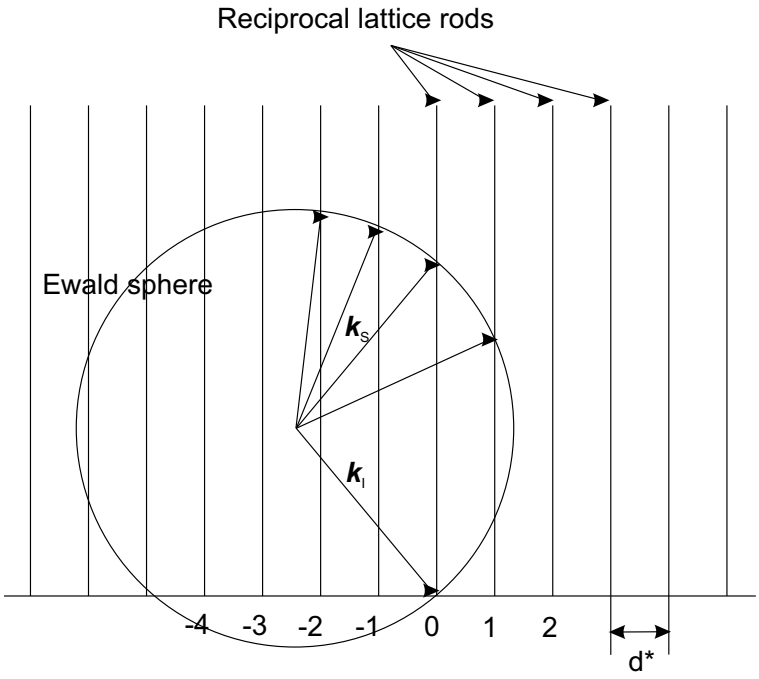

Figure 3.5: Relation of Ewald sphere and reciprocal lattice rods.

line, Ewald sphere appears as a circle.) Ewald sphere is defined as a sphere with radius of $|\boldsymbol{k}_\mathrm{I}|$. One end of the vector $\boldsymbol{k}_\mathrm{I}$ sits on the center of Ewald sphere, and the other end is defined as zeroth Laue zone. Fig.3.5 shows a relation between Ewald sphere and reciprocal lattice rods as well as Laue zones. The intersection point of Ewald sphere and reciprocal lattice rod gives the wave vectors which satisfy the energy conservation and the condition of diffraction. It is possible to expand one-dimensional atomic line to two-dimensional atomic plane. A two-dimensional atomic plane corresponds to a sample surface in a real measurement. In this case, Ewald sphere is literally a sphere, and reciprocal lattice rods appear as a two-dimensional grid.

The diffraction intensity is strongly affected by the surface morphology. Fig.3.6 shows the evolution of the diffraction intensity during ideal layer-by-layer growth mode. An atomically smooth surface (a top in Fig.3.6(a)) makes optimal diffraction with high intensity. As the deposition goes on, adatoms are supplied on the surface. The adatoms at the beginning contribute on scattering the electron beam, which causes a reduction of the diffraction intensity (Fig.3.6(b)). When the surface roughness is maximised, the RHEED intensity reaches the minimum value (Fig.3.6(c)). After this point, the surface is recovered and RHEED

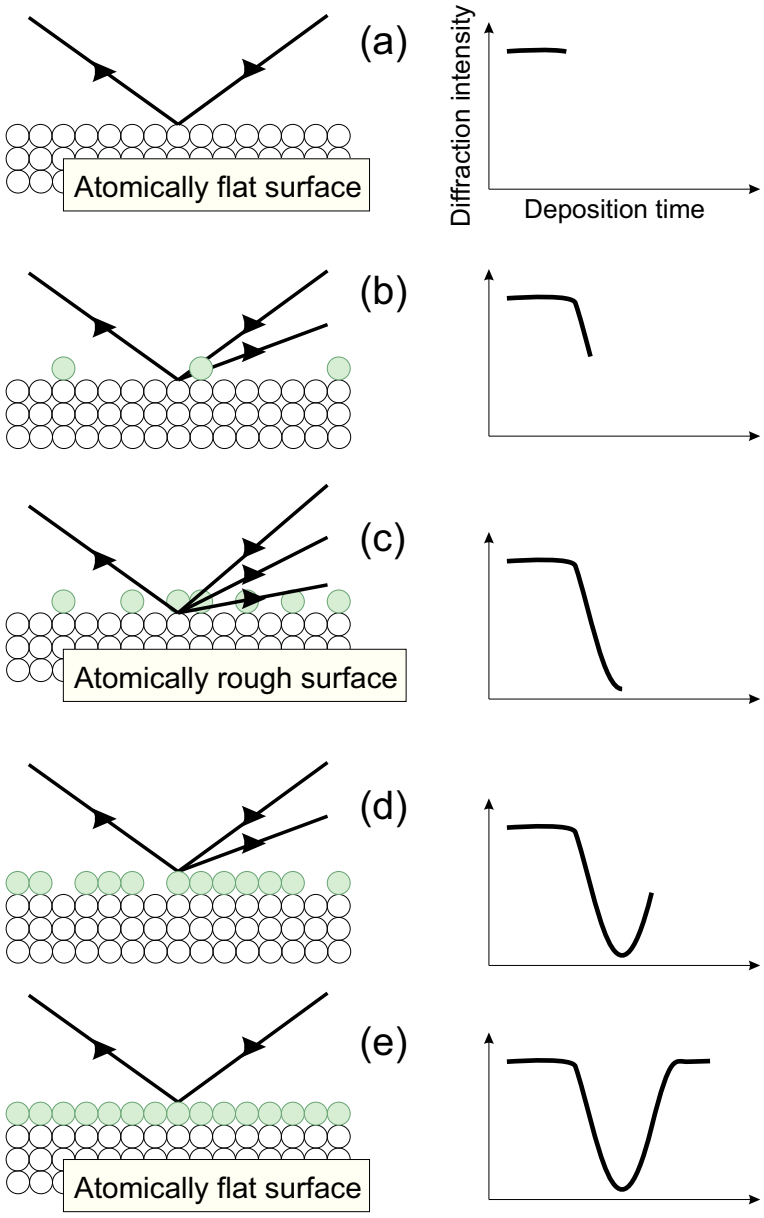

Figure 3.6: Evolution of a layer-by-layer growth during deposition in conjunction with the corresponding intensity of the RHEED.

intensity increases (Fig.3.6(d)). When the one layer is completed, the intensity comes back to the initial value (Fig.3.6(e)). In this manner, one can count the number of layers during deposition by counting the number of the oscillation of the RHEED intensity.

3.3 Atomic Force Microscope

In general, a technique to scan a surface of a sample by a probe with a sharp tip and map a certain physical property of the surface is called scanning probe microscope (SPM). According to a choice of the probe, a specific physical property is observed. In case of an atomic force microscope (AFM), an atomic force between a specimen surface and a tip of a cantilever is detected. A magnitude of the atomic force is sensitive to a distance between them. Accordingly, measuring the atomic force it is possible to derive a surface morphology of a sample with a scale of a tip radius of curvature which is in the order of nanometers.

A schematic of the representative AFM system is shown in Fig.3.7. When the cantilever is adjacent to the sample surface, the cantilever undergoes a deflection due to the atomic force between the tip and the sample surface. Because of the deflection, the laser reflected from the top of the cantilever makes a shift of the position on the photodiode sensor. Measuring the shift of the position of the reflected laser, the degree of the deflection is obtained. The height of the sample stage is controlled to keep the deflection steady, which means, the distance from the tip to the sample surface is kept constant by moving the sample stage, and at the same time, the surface asperity and roughness are measured. Repeating a line scan, two-dimensional image of the sample surface can be obtained. From the AFM analysis, we acquire the information such as the surface roughness and surface morphology which help us to figure out a growth mode as well as a quality of the crystalline structure.

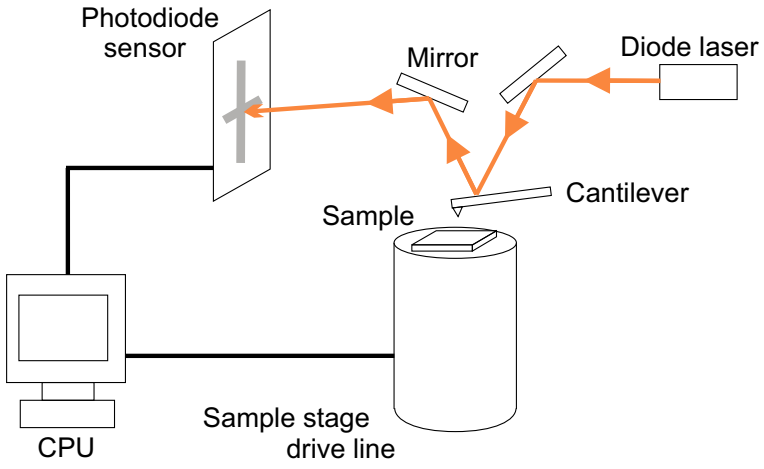

Figure 3.7: Schmatics of an atomic force microscope.

3.4 X-ray diffractometry

When X-ray is scattered by electrons bound by crystalline atoms, the diffraction of the X-ray occurs due to the periodic arrangement of the atoms. The diffraction pattern is determined by the structural periodicity of the sample. Therefore, by analyzing the diffraction pattern, the information of the crystalline structure is obtained.

Fig.3.8 shows a basic example of a diffraction from adjacent atomic layers. A flux of incident X-ray is supposed to be parallel. d is a spacing between two adjacent planes, θ is an angle between the incident X-ray and the scattering plane, and λ is a wave length of an incident wave. The diffraction occurs when the parameters satisfies Bragg equation relation,

$$2d \sin\theta = n\lambda \tag{3.6}$$

where n is an integer. The equation indicates that, when the θ is a specific glancing angle where the path difference between the incident and diffracted X-rays is a multiple of λ, interference and a peak of intensity of diffracted X-ray appear. From the equation and measured value of theta, one can calculate spacing of the layers, d. In $\theta - 2\theta$ scan, where 2θ is a scanning parameter, multiple diffraction peaks corresponding different n appear. Just for an example, Fig.3.9 shows a result of X-ray $\theta - 2\theta$ scan of a $YBa_2Cu_3O_7$ (YBCO) thin film on a (001)-oriented $SrTiO_3$ (STO) substrate. The X-ray diffraction peaks from the YBCO thin film corresponding to YBCO (00l) Bragg diffraction are present. In addition to the diffraction from YBCO, the STO substrate gives rise to the additional diffraction peaks corresponding to STO (00l) diffractions. From the analysis, the orientation of the YBCO thin film is identified.

In a thin film analysis, several kinds of diffractions possibly occur

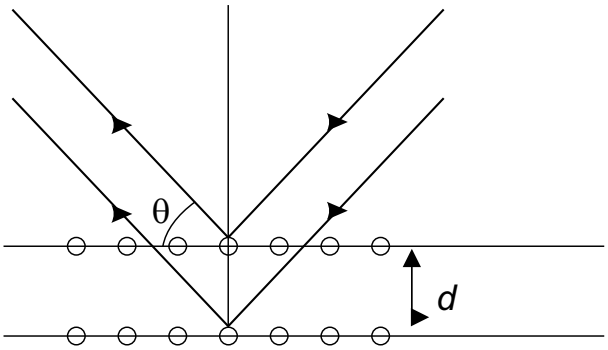

Figure 3.8: X-ray diffraction from adjacent one-dimensional atomic layers.

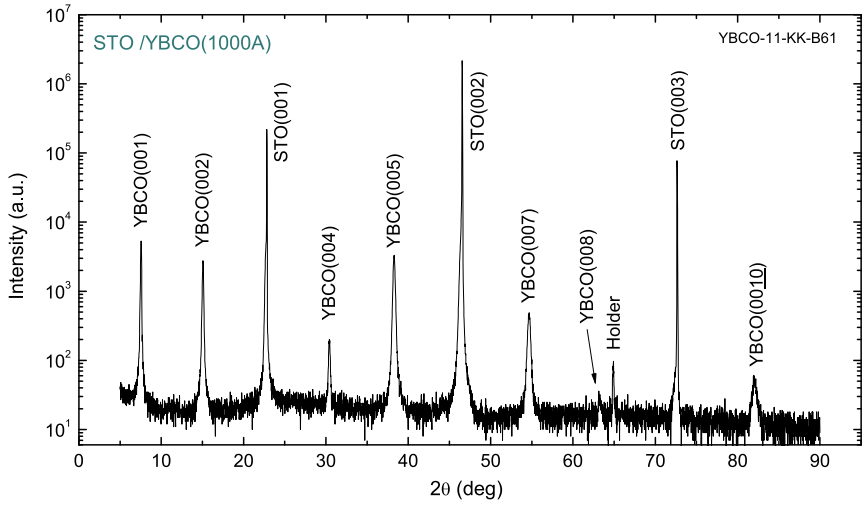

Figure 3.9: $\theta - 2\theta$ scan of the 1000 Å $YBa_2Cu_3O_7$ thin film on a $SrTiO_3$ substrate.

from different spacing. Simple diffraction demonstrated above is the diffraction originating from two adjacent atomic layers, where d corresponds to the crystalline lattice constant. The crystalline structure and phase purity can be evaluated from this measurement. Additional diffraction can happen around the diffraction peak of atomic layers, so-called Laue oscillation. A spacing of Laue oscillation corresponds to a total thickness of contributing crystalline layers. This means, Laue oscillation is available for estimation of the film thickness and as an indicator of a quality of crystalline structure. In a sample with superlattice structure which possesses the repetition of bilayer structure, another characteristic spacing corresponding to the thickness of bilayer exists. This gives rise to so-called superlattice peaks. Clarity of superlattice peaks depends on a quality of the interface. An existence of superlattice peaks is a principle indicator of a quality of the superlattice structure. Oscillations could be observed at the low angle region around $< 3 \sim 5$ deg in $\theta - 2\theta$ scan. These oscillations are called Kiessig oscillations which originate from diffraction between the surfaces of the substrate and of the sample. Therefore Kiessig oscillations give the information of a thickness and roughness of the sample surface. It should be noted that Kiessig oscillations are sensitive to a roughness of the surface or interfaces, and not to the crystalline structure. On the other hand, Laue oscillation is originated from the volume of crystalline structure.

So far the XRD analysis was discussed within the out-of-plane XRD

regime, where the diffraction occurs from the planes parallel to the surface of the sample. By measuring the diffraction peaks which originate from the crystallographic planes not perpendicular and/or parallel to lattice vectors, one can observe not only out-of-plane information but also in-plane one. Reciprocal space mapping (RSM) is one of those measurements. In RSM, a reciprocal lattice space is mapped around a certain diffraction peak in the in-plane and out-of-plane axes, and one can calculate the lattice parameters in both directions. The shape of the diffraction peak provides the information related to the strain state of the thin film.

XRD is a quite powerful tool to understand a structural property of a thin film sample. $\theta - 2\theta$ scan and RSM help to derive the in-plane and out-of-plane lattice parameters as well as a quality of a crystalline structure. Besides these techniques, homogeneity of an orientation can be evaluated by a rocking curve measurement. ϕ scan and pole figure measurement show mosaicity of a crystalline texture.

3.5 Photoconductivity measurement

Schematic of the optical cryostat, which is utilized for a photoconductivity measurement, is given in Fig.3.10. The optical cryostat is equipped with a transparent quartz window, through which an external light source illuminates a sample in the cryostat. The sample locates on the cooling finger, which is in contact with the helium line for cooling. During measurement, a helium flow is pumped from a helium dewar through a cooling finger with a constant rate.

A temperature of the sample is controlled by adjusting a power of a built-in heater sitting nearby the sample according to a simultaneously measured temperature by a built-in temperature sensor which is also mounted close to the sample. The measurement system is composed of a voltmeter and a current supply for the transport measurement, and another voltmeter connected to the temperature sensor for the temperature measurement. The electrical measurement is conducted by a standard four point contact method with evaporated Au electrodes on

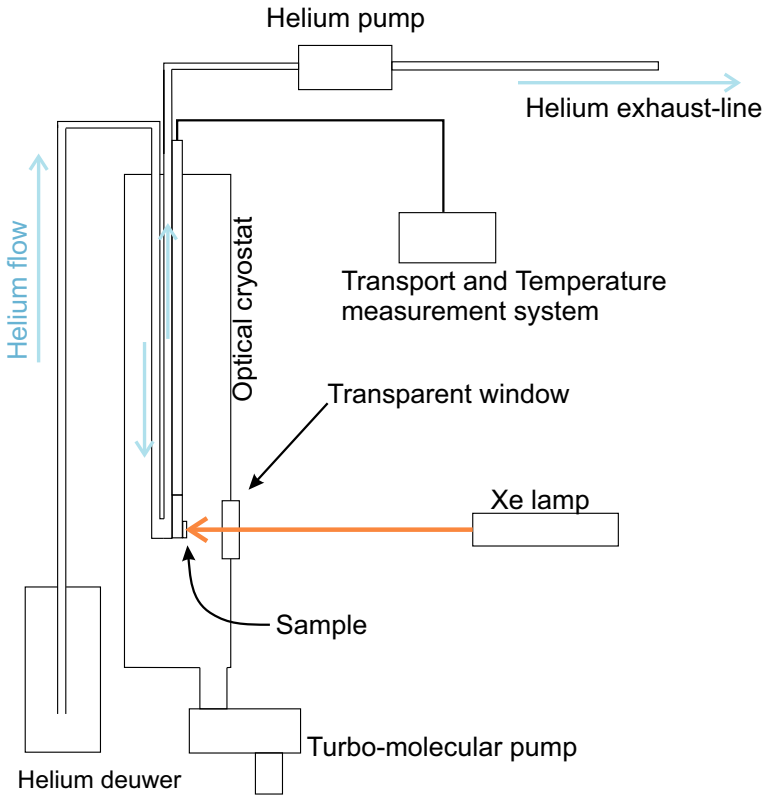

Figure 3.10: Schematic of a photoconductivity measurement set-up.

top of the sample.

In order to avoid a thermal conduction between the sample and surrounding atmosphere, the inside of the optical cryostat is kept in a high vacuum of 10^{-6} mbar by the use of a turbo-molecular pump. A Xe lamp, which has a spectral distribution from 200 nm to 2000 nm, is used as a light source. A transmission filter was placed between the quartz window and the Xe lamp to block an infrared part of the spectrum to reduce a heating effect.

3.6 VSM SQUID magnetometry

A vibrating Sample Magnetometer (VSM) was used to measure magnetic properties of our samples. A sample is mounted in an uniform magnetic field, and is vibrated with a certain amplitude and frequency. The vibration of the sample causes an induced voltage in a pick-up coil placed nearby the sample. The induced voltage is analyzed by a lock-in amplifier, and a magnetic moment of the sample is determined. In case that a superconducting quantum interference device (SQUID) is applied to detect a magnetic flux inductively coupled to the sample, a precision of the measurement can be highly improved due to an extreme sensitivity of a SQUID. The VSM setting combined to SQUID with high precision is called VSM SQUID.

Since VSM SQUID is quite sensitive to the existence of any stray magnetic field, the system should be designed carefully to avoid the influence of them. VSM SQUID is composed of :

1. Temperature control allowing to vary the sample temperature from 2 K to 400 K.
2. Facilities controlling the chamber atmosphere.
3. Magnetic field control generating external magnetic field on the sample up to 7 tesla.
4. Motion control oscillating the sample in the magnetic field
5. SQUID detection system sensing the induced signal collected by the pick-up coil

The temperature of the sample is controlled by cooling due to drawing cryogenic helium gas into helium flow inlet going adjacent to the sample position and heating via a heater. A flow rate of the helium gas is controlled according to a flow sensor mounted in the inlet to achieve a necessary supply of helium. The helium flow rate and the power on the heater should be controlled precisely according to the thermometers mounted around the sample holder.

During measurements, the chamber is held in a medium vacuum: $\sim$5 torr at a room temperature. In respect of the temperature control, the vacuum environment is required for the inside chamber, because the thermal radiation from the sample is avoided in the vacuum, then the sample and sample chamber wall can achieve a uniform temperature. It is also important that helium is the only gas in the chamber. Because the other gases such as water vapor, nitrogen and oxygen are going to

freeze at low temperatures, and they cause mechanical problems and artifacts in sensitive magnetic measurements.

The uniform magnetic field on the sample is generated by a superconducting Niobium-Titanium solenoid, equipped with a superconducting thermal quick switch. The solenoid covers the whole area around the sample to induce the uniform magnetic field on the sample. The switch is immersed in liquid helium, and a heater is mounted to heat up the switch above its superconducting critical temperature to start the persistent mode where the solenoid current and the magnetic field are extremely stable.

The vibrating motion of the sample during measurement is achieved by the motion control system. We are using 14 Hz for a vibration frequency, and the vibration amplitude can be altered from 0.5 mm to 8 mm depending on the sample dimension, mass and sample holder.

The SQUID detection system is the heart of the VSM SQUID system. SQUID detection is extremely sensitive to the magnetic signal from the sample itself, as well as stray fields inside and outside of the system. Therefore a careful attention is paid for a construction of this part. The superconducting detection coils are configured as a second-order gradiometer (shown in Fig.3.11), with counterwound outer loops which are responsible for a cancellation of uniform magnetic fields and linear magnetic field gradients. As the sample moves in an oscillatory way in the detection coil, a current is induced in the detection coil. This current is inductively coupled to the DC SQUID which is a magnetically-shielded. A digital lock-in amplifier is used to isolate the second harmonic signal from the SQUID voltage, and it is digitized by the instrument electronics. The resulting harmonic signal is connected to the sample vibration, and the amplitude corresponds to a magnetic moment of the sample via a scaling factor.

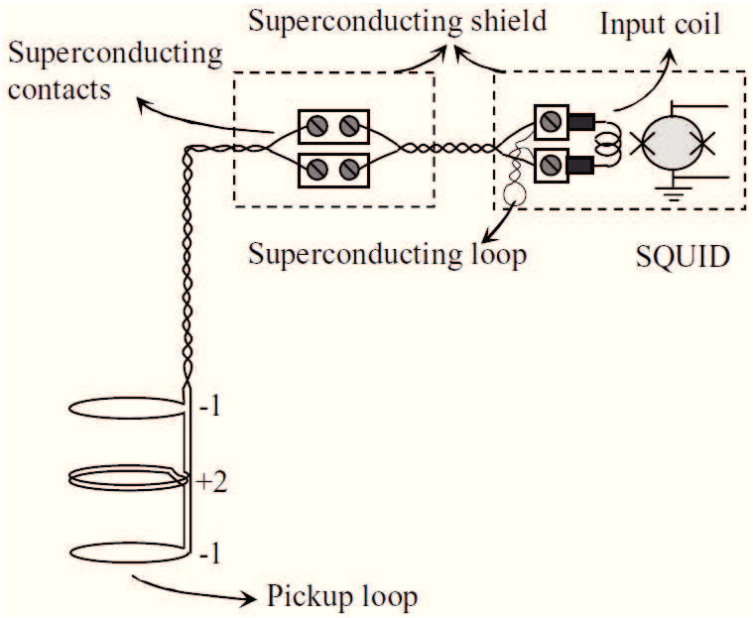

Figure 3.11: (From Ref. [83]) Schematic view of the pickup coil and the SQUID input circuit in a SQUID magnetometer.

3.7 AC susceptibility measurement

AC susceptibility is measured with a mutual inductance configuration where two pancake coils: a drive coil and a pick-up coil, sandwich a thin film sample. Fig.3.12 shows a schematic diagram of the system.

A current power source supplies an alternative current $I = I_0 \exp(i\omega t)$ in the drive coil. A magnetic field induced by the drive coil is given as $H = n_1 \cdot I$, where n_1 is a number of coil turns of the drive coil per unit length. The induced magnetic flux density B at the receive coil is given by $B = \mu(H + M)$, where μ is permeability. Taking account of $M = \chi H$ with χ as a susceptibility, the magnetic flux Φ at the receive coil is given as follows,

$$\Phi = S \times B = S \times \mu(1 + \chi)H, \tag{3.7}$$

where S is a cross-sectional area of the coil. The induced voltage in the receive coil V is given as

$$V = -n_2 \frac{\Delta\Phi}{\Delta t} = -n_1 n_2 S\mu(1 + \chi)\frac{\Delta I}{\Delta t}, \tag{3.8}$$

where n_2 is a number of coil turns of the receive coil. Substituting $I = I_0 \exp(i\omega t) = I_0\{\cos(\omega t) + i\sin(\omega t)\}$, and applying a complex susceptibility $\chi = \chi' + i\chi''$, where χ' indicates Meissner effect and χ'' energy loss, V becomes as follows,

$$\mathrm{Re}(V) = n_1 n_2 S\mu I_0 \omega |\tilde{\chi}| \sin(\omega t + \phi), \tag{3.9}$$

$$\mathrm{Im}(V) = -n_1 n_2 S\mu I_0 \omega |\tilde{\chi}| \cos(\omega t + \phi), \tag{3.10}$$

with $(1 + \chi') = |\tilde{\chi}| \cos\phi$ and $\chi'' = |\tilde{\chi}| \sin\phi$, where ϕ is a phase shift. By measuring the induced voltage V in the Lock-in amplifier, the phase

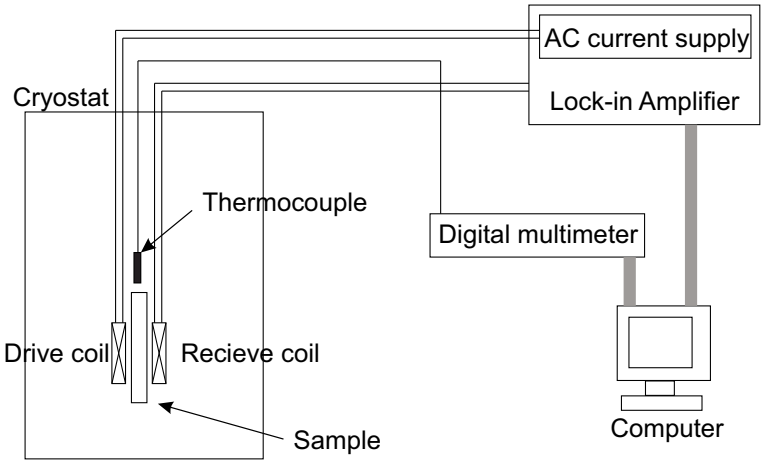

Figure 3.12: Schematic diagram of the mutual inductance setting.

shift ϕ and the amplitude $|\tilde{\chi}|$ can be obtained, and then χ' and χ'' as well. The temperature is measured by the temperature sensor mounted nearby the sample position.

Chapter 4

Results

4.1 Interrelation of epitaxial strain and oxygen deficiency in $La_{0.7}Ca_{0.3}MnO_{3-\delta}$ thin films

4.1.1 Background

Due to scientific interests for the remarkable properties such as the large CMR effect and the high spin-polarization of the conducting electrons, intensive studies were devoted to a fundamental understanding of the nature of the electronic and magnetic properties of LCMO thin films. One of the main topics in the research is the effect of the epitaxial strain on their electronic properties. Using an appropriate substrate it is possible to induce a tensile or compressive strain to epitaxially grown thin films [84, 85]. These strain affects the competition between the double exchange interaction and Jahn-Teller distortions, and leads to a change in the transport and magnetic properties [61, 86–88]. To use the strain is regarded as a straightforward and powerful method to develop the understanding of the nature of the properties of LCMO thin films. Additionally, the oxygen stoichiometry plays an important role in determining the properties of LCMO. Oxygen vacancies drive the Mn valence state from Mn^{4+} to Mn^{3+}, and the functional properties will be modified [89]. In general, the concentration of oxygen vacancies is determined by the growth thermodynamics, growth kinetics, and post-annealing. Several papers dealing with oxygen incorporation and depletion [90, 91] in manganite thin films have already been published. Lattice strain and the oxygen deficiency are considered as the key parameters to tune the properties of the rare earth manganite thin films for a given cation doping level, both, electronically and geometrically.

Here, it should be noted that extrinsic strain (e.x. induced by lattice mismatch between the substrate and the film) and intrinsic strain (e.x. induced by growth-related defects such as oxygen vacancies, stacking

faults, dislocations, and so on) are coupled in the real complex oxide systems and each of their contributions cannot be separated. It was pointed out that the lattice mismatch between film and substrate can impact the oxygen incorporation [26, 27] via minimizing the elastic energy. Therefore, in this section, a systematic study using LCMO thin films are performed to shed light on this interrelation and develop a general view. The lattice strain is intentionally changed by using different substrates: STO, LSAT and LSAO, and the oxygen concentration in the LCMO thin films is altered by using four different oxygen pressures during growth, namely, 0.27, 0.2, 0.13 and 0.1 mbar. Structural and functional measurements are conducted on all samples, and the changes of the properties are discussed in terms of the lattice strain and the oxygen deficiency.

4.1.2 Experiments

Doped manganites thin films $La_{1-x}Ca_xMnO_{3-\delta}$ with x=0.3 were grown by the pulsed laser deposition (PLD) method. For the PLD process a KrF excimer laser with a wave length of 248 nm was used, applying a commercial LCMO target (Lesker) and an energy fluency on the target of 1.5 J/cm^2. We grew 1000 Å LCMO films on (001) STO, (001) LSAO and (001) LSAT substrates. The room temperature in-plane lattice parameter of pseudo-cubic LCMO is 3.86 Å. The lattice constants of STO, LSAO and LSAT substrates are 3.905, 3.75 and 3.87 Å, respectively. The lattice mismatch, m, between the LCMO films and the substrates, calculated as $m = (a_F - a_S)/a_S$, are -1.2, 2.9 and -0.3%, for STO, LSAO and LSAT, respectively, where a_F and a_S are in-plane lattice parameters of the unstrained LCMO layers and the substrates. Therefore the LCMO films deposited on STO substrates are under tensile strain. In contrast, the LCMO films on LSAO substrates are under compressive strain. The lattice mismatch between the LCMO and LSAT substrate is negligible. The deposition temperature was kept at 750 °C in this work. After deposition, the samples were cooled down to 530 °C with 15 °C/min then the oxygen pressure was set to 1 bar. The post-annealing lasted for 1 hour, afterwards the infrared laser heater for the substrate was turned off. The samples cooled down to room temperature within 10 min. For each substrate, four LCMO thin films were deposited with different oxygen pressures, namely, 0.27, 0.2, 0.13 and 0.1 mbar. The combination of two parameters, the controlled lattice mismatch and the oxygen pressure during film growth, enables us to explore the interrelation between the oxygen deficiency in the LCMO films and the lattice strain.

After the LCMO film growth, the surface morphology was investigated by atomic force microscopy (AFM). X-ray diffraction (XRD) as well as reciprocal space mapping (RSM) was used to characterize the

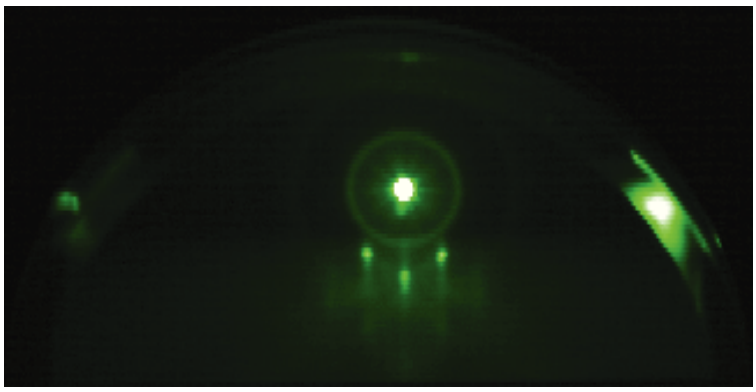

Figure 4.1: RHEED pattern from the LSAT substrate.

crystal structure and the epitaxial strain states. Finally, a Quantum Design system SQUID vibrating sample magnetometer (VSM) and a PPMS Quantum Design system were applied to investigate the magnetic and transport properties. For the transport measurements Au contacts for standard four contact methods were evaporated on the top of the samples.

4.1.3 Results and discussions

RHEED analysis

The RHEED pattern of the cubic LSAT substrate is shown in Fig.4.1. First of all, the spot with the strongest intensity is the direct beam. Then, the specular spot is present in the center, below the direct beam, surrounded by the first order Laue diffractions. The sharpness of the reflection and diffraction spots indicates a flat surface of the substrate. There is noticeable streaking caused by small area of coherence on the surface originating from the step-terrace structure of the substrate.

Fig.4.2 shows the intensity of the specular spot during LCMO deposition on LSAT substrates as a function of the time. Each RHEED intensity curve shows more or less a different behavior. The decrease of the oscillation amplitude with further increase of the film thickness is ascribed to the change of the growth mode from a layer-by-layer to a steady-state regime. The way of damping in the RHEED intensity oscillation is different from a sample to another. Especially in the sample grown at 0.27 mbar, the damping of the RHEED intensity is pronounced, and in the samples grown at lower pressures, the oscillation is more stable. All the curves exhibit one or two maximum in the RHEED intensity

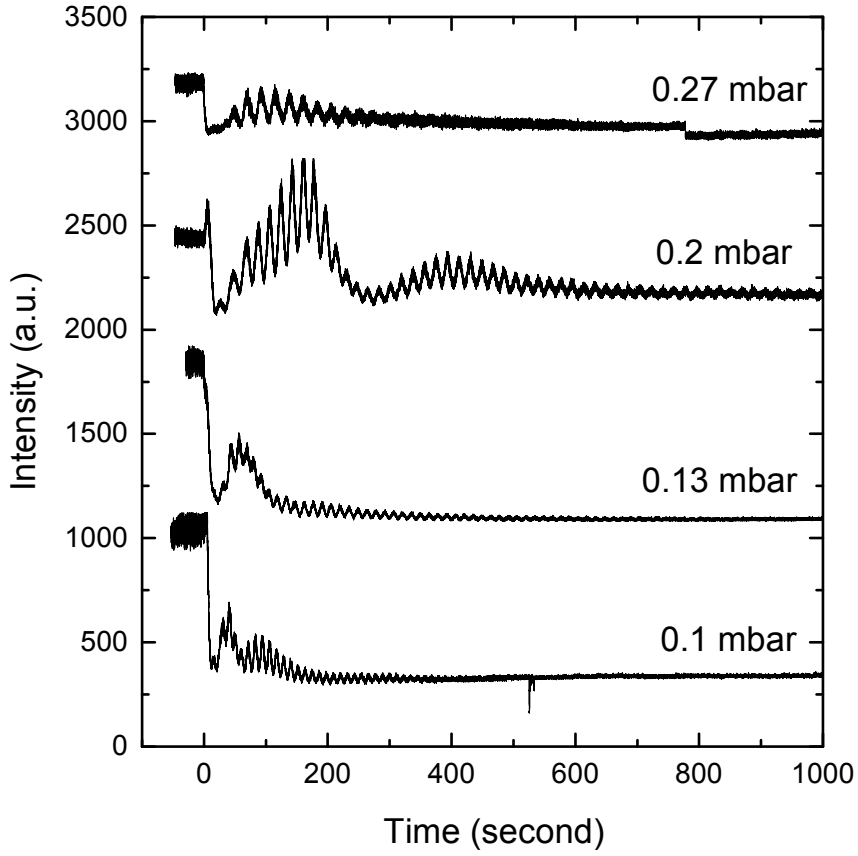

Figure 4.2: Time dependence on the intensity of the specular spot during LCMO deposition on LSAT substrates. The intensity is shifted by a constant for the eye. From the top, each curve indicates the intensity during the growth at 0.27, 0.2, 0.13 and 0.1 mbar.

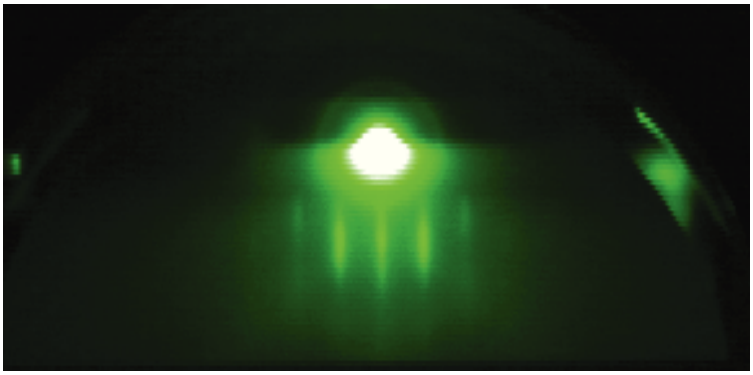

Figure 4.3: RHEED pattern after deposition of 1000 Å LCMO layer on LSAT substrate at the oxygen deposition pressure of 0.27 mbar.

during growth. The origin of those maximums is regarded to arise from a competition between recovery of the initial reconstruction at the interface and roughening during growth. Those maximums appear in the different timing after start of the growth. These facts indicate that the growth mode and thus the microstructure in the film are influenced by the oxygen pressure. From the viewpoint of kinetics, the higher oxygen pressure causes more scattering between ablated species and oxygen ions and thus a reduced kinetic energy of them when impinging the substrate surface. As a result, the moderated adatoms contribute to favor on the island growth mode due to reduced mobility. Accordingly the layer-by-layer growth mode is facilitated and a smooth surface is expected.

Fig.4.3 and Fig.4.4 show the RHEED pattern after 1000 Å LCMO growth on LSAT substrates at 0.27 mbar and 0.1 mbar, respectively. The both patterns denote clear RHEED pattern from the crystalline surfaces, which confirm the nice quality of the surface structure. The spot shapes are stretched compared to the RHEED pattern from the substrate shown in Fig.4.2. This is because the sample surface is rougher than the original substrate and has narrower terraces.

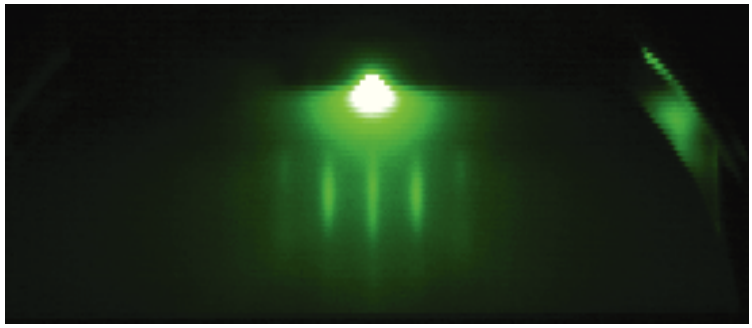

Figure 4.4: RHEED pattern after deposition of 1000 Å LCMO layer on LSAT substrate at the oxygen deposition pressure of 0.1 mbar.

The substrate dependence can be demonstrated by comparing the growth on the different substrate with the same deposition pressure. Fig.4.5 shows the time dependence on the RHEED intensity during growth of LCMO thin film on STO substrate at 0.13 mbar. The growth of LCMO on STO substrate shows continuous oscillation of the RHEED intensity. The quality of the oscillation is similar to the one observed in LCMO on LSAT substrate at 0.13 mbar in Fig.4.2. On the other hand, the RHEED intensity during LCMO growth on LSAO substrate is given in Fig.4.6. The damping of the oscillation is rapid and the oscillation disappears quickly. The result indicates that the layer-by-layer growth mode is strongly suppressed in the LCMO growth on LSAO substrate, most likely, because of the large lattice mismatch m=2.9%.

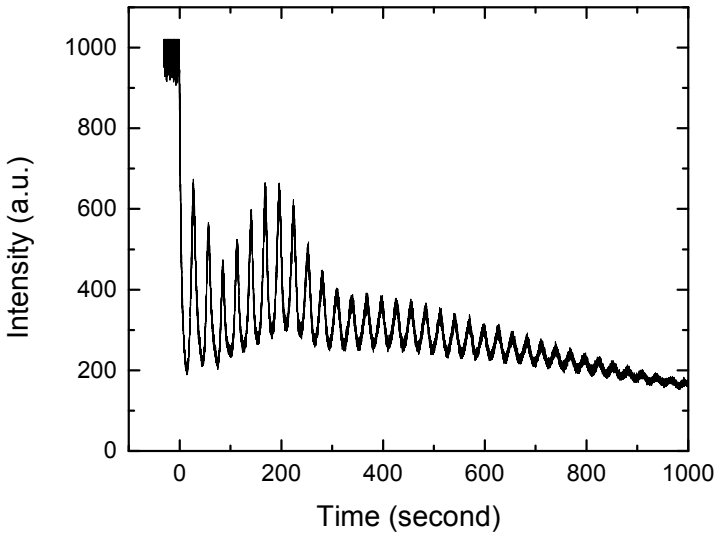

Figure 4.5: Time dependence on the intensity of the specular spot during LCMO deposition on a STO substrate at the oxygen deposition pressure of 0.13 mbar.

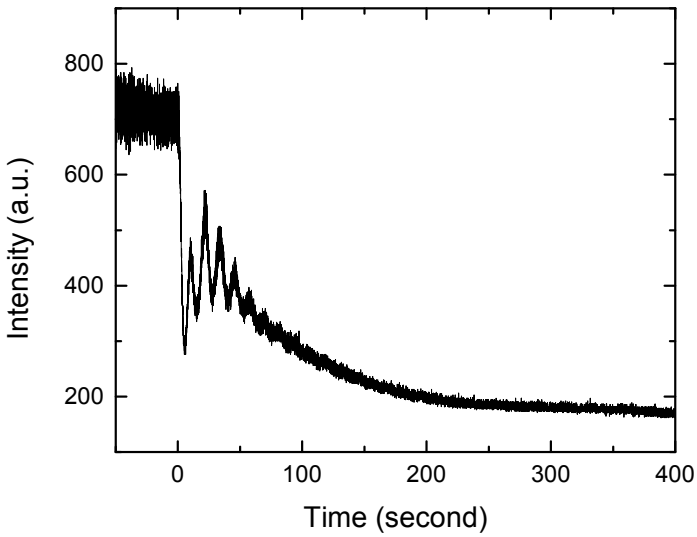

Figure 4.6: Time dependence on the intensity of the specular spot during LCMO deposition on a LSAO substrate at the oxygen deposition pressure of 0.13 mbar.

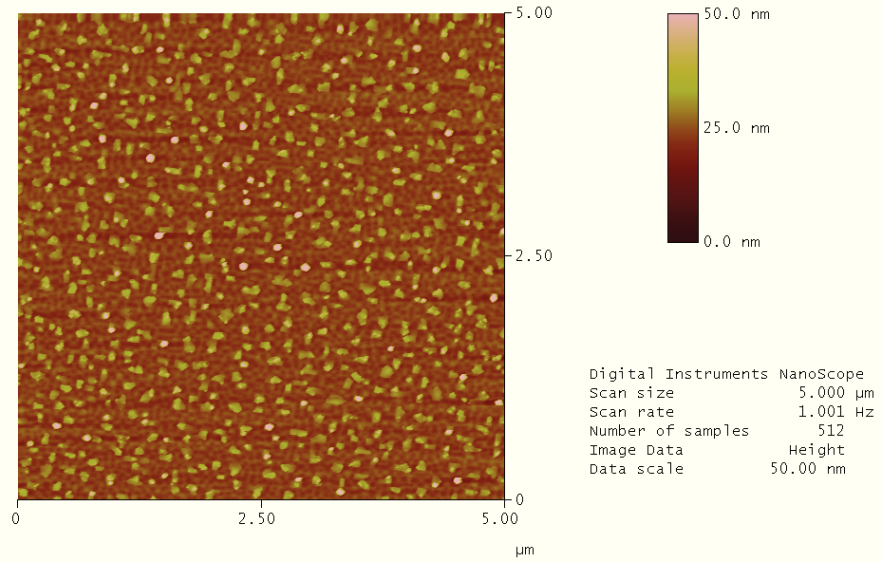

Figure 4.7: AFM image of the 1000 Å LCMO on LSAT grown at 0.27 mbar.

Surface morphology

Fig.4.7 shows the AFM image of the 1000 Å LCMO thin film grown at 0.27 mbar on LSAT substrate. Small grains are present on the surface of the sample and the surface is granular. The AFM image of the 1000 Å LCMO on LSAT grown at the oxygen pressure of 0.2 mbar is shown in Fig.4.8. The small grains are present, however the roughness is improved compared to the sample grown at high pressure 0.27 mbar shown in Fig.4.7. In the 1000 Å LCMO grown at further lower deposition pressure of 0.13 mbar, the AFM image shows further smooth morphology (Fig.4.9). Here, not only the grain size is smaller, but also the step-terrace structure is present. The morphology of the substrate is transferred to the sample surface due to a nice epitaxial and two-dimensional growth. Finally, the AFM image of the 1000 Å LCMO on LSAT grown at 0.1 mbar is shown in Fig.4.10. The image is nearly same as that of the sample grown at 0.13 mbar. The step-terrace structure is present. Additionally, the AFM image of the 1000 Å LCMO thin film on the LSAO substrate grown at 0.13 mbar is given in Fig.4.11. Even in this sample, the step-terrace structure is visible. This result is rather puzzling when taking account of the RHEED oscillation in Fig.4.6, which indicates strong reduction of layer-by-layer growth in this sample. The reason should be discussed later in conjunction with the

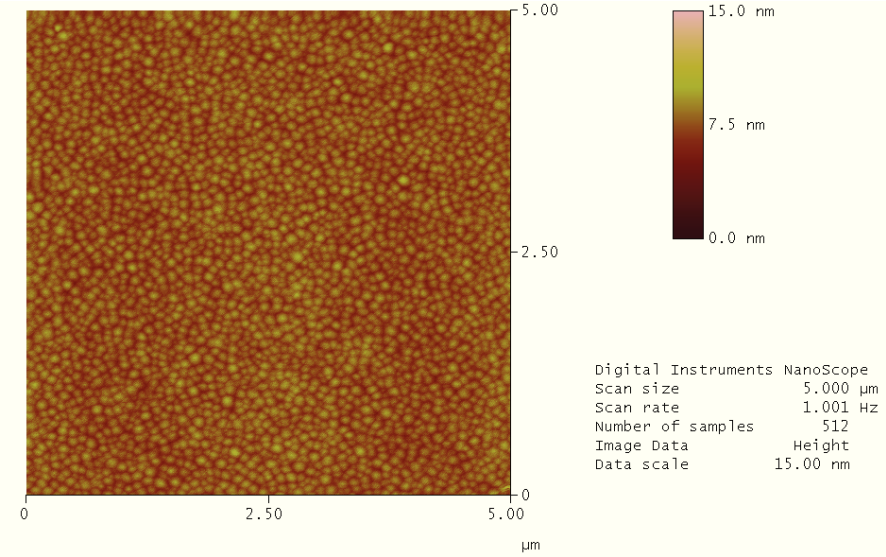

Figure 4.8: AFM image of the 1000 Å LCMO on LSAT grown at 0.2 mbar.

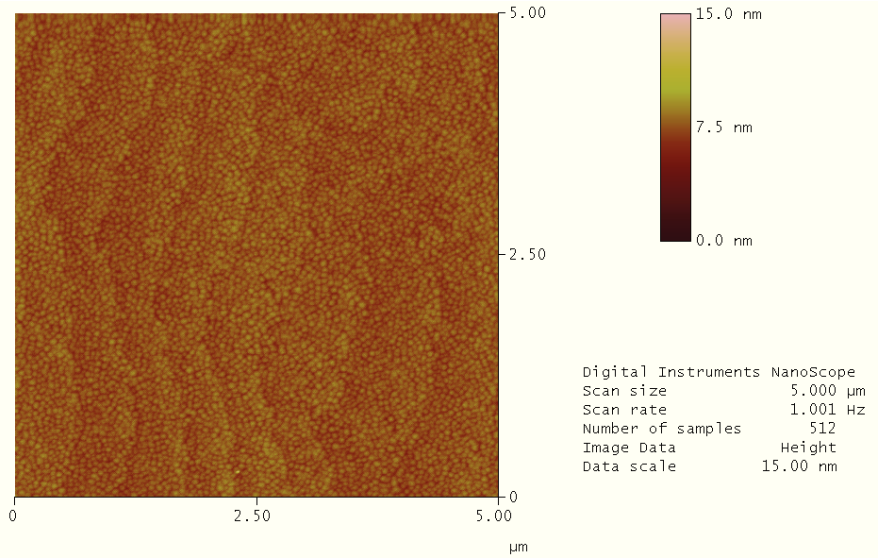

Figure 4.9: AFM image of the 1000 Å LCMO on LSAT grown at 0.13 mbar.

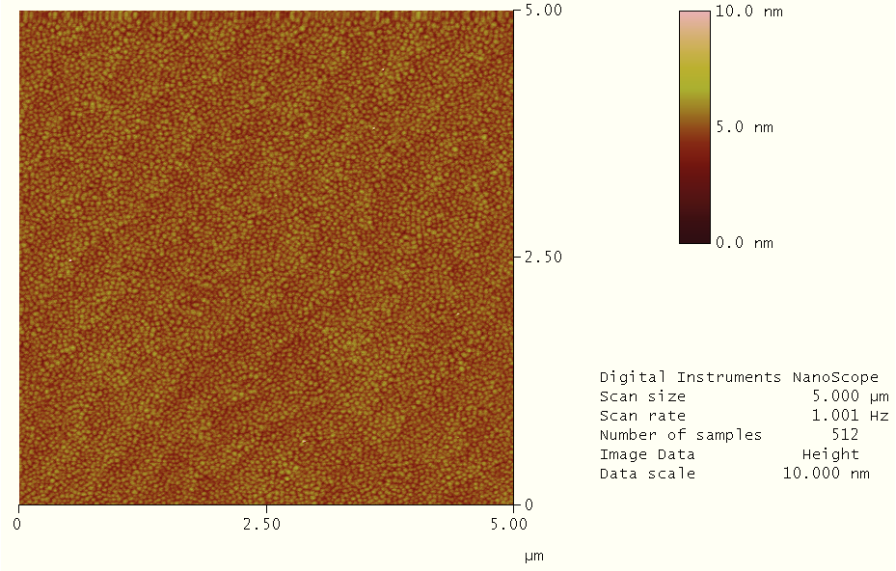

Figure 4.10: AFM image of the 1000 Å LCMO on LSAT grown at 0.1 mbar.

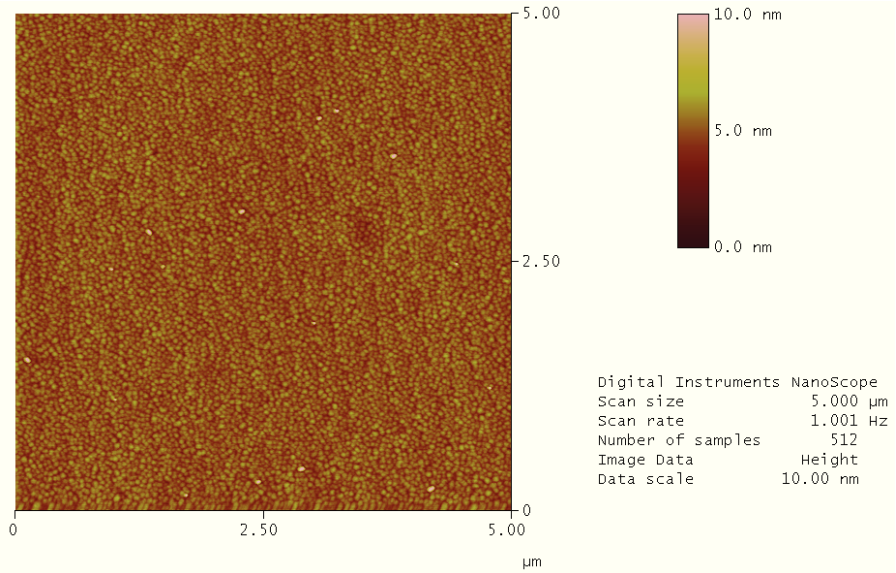

Figure 4.11: AFM image of the 1000 Å LCMO on LSAO grown at 0.1 mbar.

structural analyses via XRD measurements.

Fig.4.12 shows the dependence of the root mean square (RMS) surface roughness measured by AFM versus the oxygen pressure during growth of all our LCMO films. The samples which were deposited at pressures lower than 0.2 mbar showed RMS values less than 1 nm. A higher oxygen pressure (0.27mbar) causes an increase of the RMS values up to 2.7∼4.2 nm. This tendency was observed for the different substrates. We conclude that increase of the oxygen pressure causes a crossover from a layer-by-layer growth mode to an island growth mode. This conjecture follows from the fact that the PLD deposition rate increases with decrease of the oxygen pressure for the same laser fluency and not due to change of the surface mobility of the oncoming species. Increase of the deposition rate with decrease of the oxygen pressure causes the transition from a 3D island growth mode to a 2D layer-by-layer growth mode.

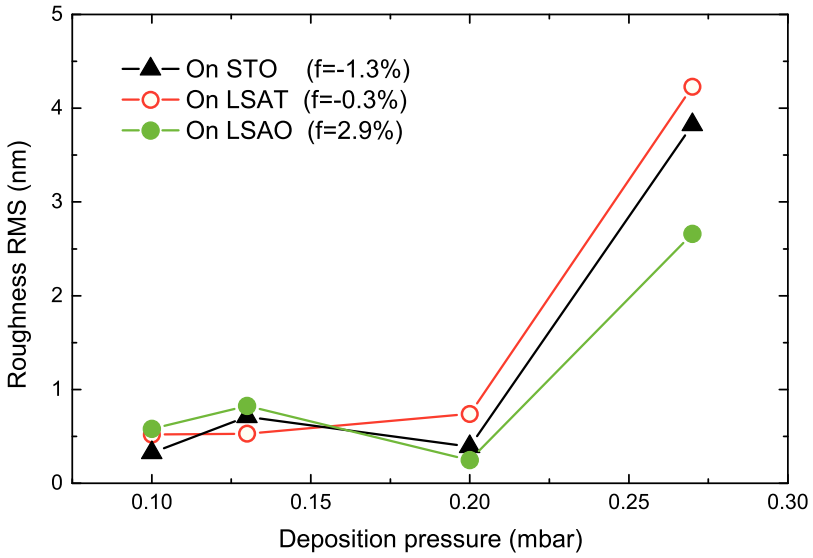

Figure 4.12: Relation between the surface roughness and the deposition pressures of 1000 Å LCMO thin films on the STO substrates (filled triangles), LSAT substrates (open circles), and LSAO substrates (filled circles).

XRD analysis

The results of the XRD $\theta - 2\theta$ scans of all the 1000 Å LCMO thin films are presented in Fig.4.13. Here, the magnification around the LCMO (002) peak is shown. The diffraction intensity is normalized to the peak intensity of the substrates. For the LCMO film grown at 0.27 mbar oxygen pressure on STO substrate the (002) peak position is at higher angle than the bulk value. This corresponds to a reduced out-of-plane lattice constant compared with bulk value. For tensile strain the in-plane lattice constant stretches, while the out-of-plane lattice constant shrinks. For LCMO films deposited at reduced oxygen pressures the (002) peak positions shift to lower angles, what corresponds to the increase of the out-of-plane lattice constant. The elongation of out-of-plane parameter indicates the increase of the oxygen deficiency in the film [89,91,92] since oxygen vacancies cause the increase of the Mn ionic radius due to change of the Mn valence state from Mn^{4+} to Mn^{3+}. The ionic radius of Mn^{3+} is 0.7 Å as compared to 0.5 Å for Mn^{4+} [92]. The shift of the (002) film peak position confirms that the concentration of oxygen vacancies was modified by the change of the oxygen pressure during growth. Note that it is difficult to estimate quantitatively the concentration of oxygen vacancies based on the (002) diffraction peak position since the peak position is determined not only by the concentration of oxygen vacancies but also by the lattice strain and relaxation of it. The high quality of the crystal structure and interface roughness of the LCMO film on STO substrate deposited at low pressures can be judged from the finite-thickness oscillations of X-ray diffraction intensity in the $\theta - 2\theta$ scan. The LCMO film grown at 0.27 mbar oxygen pressure does not show the finite-thickness oscillations. This result is consistent with the fact that the surface of this film measured by AFM is rough compared to films grown at lower oxygen pressures.

The 1000 Å LCMO films grown on LSAT substrates with small lattice mismatch also show the successive shift of the (002) peak position due to generation of oxygen vacancies during films growth at low oxygen pressures. Since the LCMO (002) diffraction peak position of the sample deposited at 0.27 mbar oxygen pressure matches the calculated position 47.06° corresponding to the bulk out-of-plane lattice constant 3.86 Å, this LCMO film is least affected by the strain as expected from the small lattice mismatch. Here again finite-thickness oscillations are visible on the right side of the peaks, except for the sample deposited at 0.27 mbar oxygen pressure, where the film surface is rough.

In 1000 Å LCMO films grown on LSAO substrates, the position of the (002) peak is at a lower angle (see Fig.4.13(c)) compared to the position expected for the bulk, what corresponds to a larger out-of-

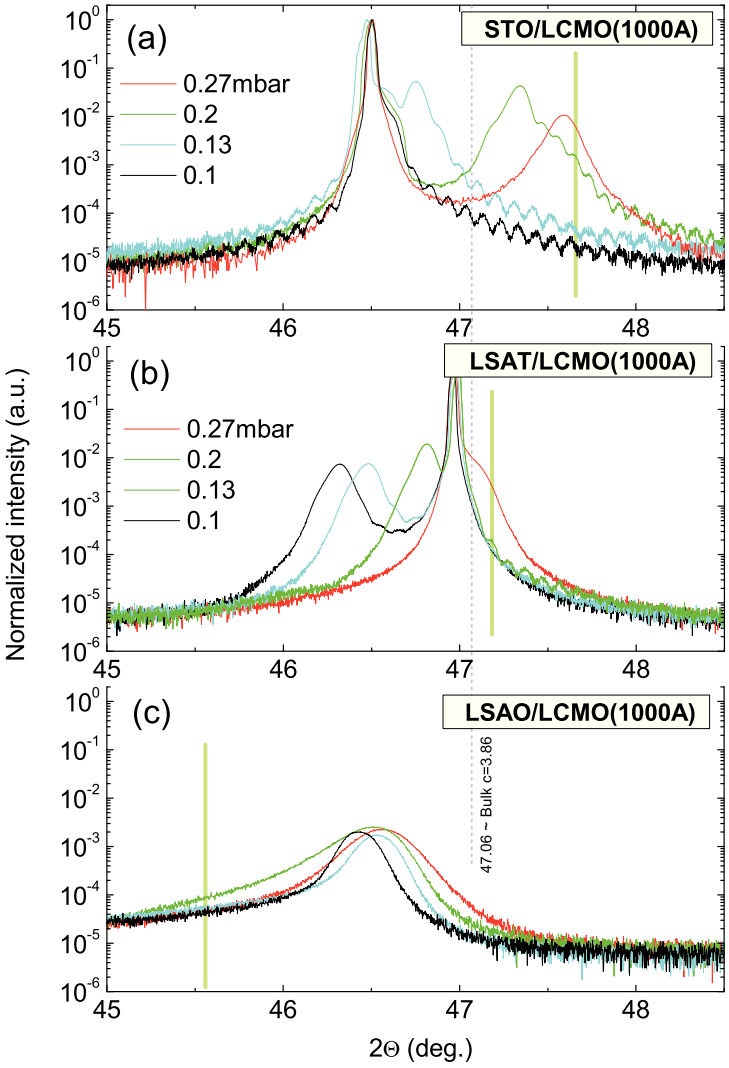

Figure 4.13: XRD scans around LCMO (002) peak of the 1000 Å LCMO films. The diffraction intensity is normalized to STO (002), LSAT (002) and LSAO (006), respectively. The (006) diffraction peak of LSAO substrate is at 42.91°, which is out of the range shown in the figure. The vertical solid lines correspond to the expected positions of fully strained and entirely stoichiometric LCMO films, and the dotted line represents the position of the bulk LCMO (002) peak.

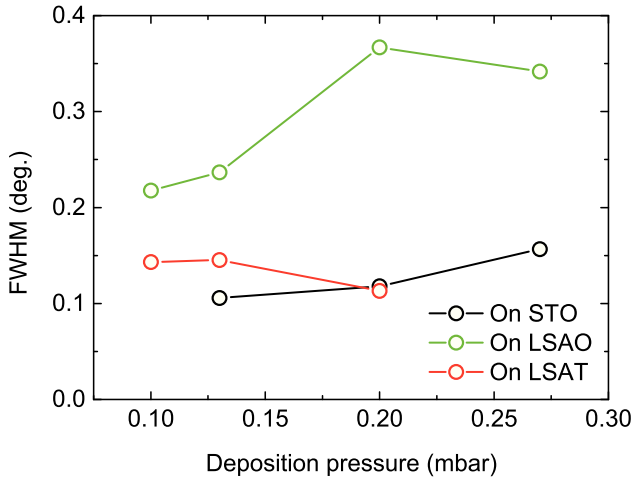

Figure 4.14: Values of full width at half maximum of the LCMO (002) peak of the 1000 Å LCMO films. In some samples, the values are missing since the LCMO peaks overlap with the peaks from the substrate.

plane lattice constant compared with the bulk one. This elongation of the out-of-plane constant could be caused by the compressive strain. In these samples, the shift of the (002) peak position due to the change of the oxygen pressure during growth is not noticeable in contrast to cases of STO and LSAT substrates. Instead of that, there is a large change in the full width at half maximum (FWHM) of the thin film peaks as shown in Fig.4.14. The LCMO films on LSAO substrates have larger FWHM values compared to the values of LCMO films grown on STO and LSAT substrates. The large values of FWHM of the LCMO films on LSAO substrate grown at 0.27 and 0.2 mbar is caused by the large inhomogeneity in terms of the out-of-plane lattice parameter, most likely due to strain relaxation and island growth mode which is fostered by a compressive strain [61].

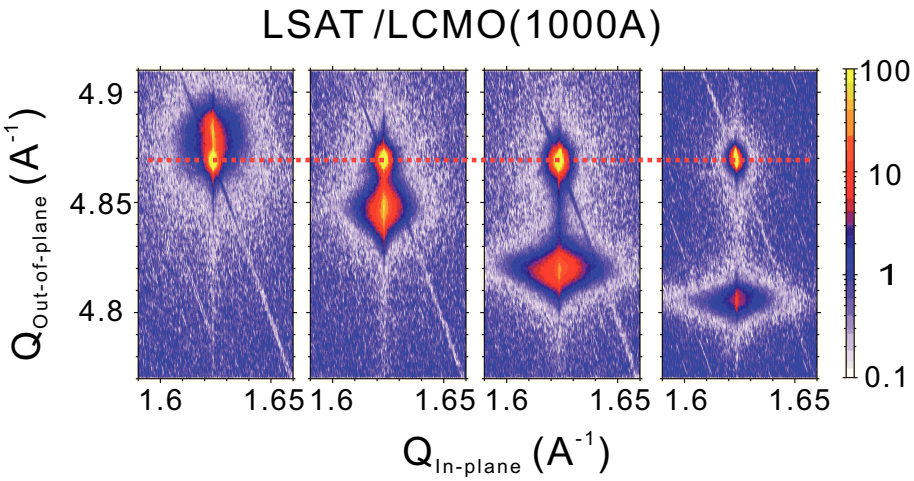

Figure 4.15: Reciprocal space maps of 1000 Å LCMO on LSAT around (013) LSAT diffraction peak. The figures are corresponding to the samples grown at 0.27, 0.2, 0.13 and 0.1 mbar from the left to the right. The dotted line indicates the LSAT (013) diffraction position.

Further analysis of the crystal structure of our LCMO films were done using reciprocal space map (RSM) plots. Fig.4.15 shows the RSM plots of the diffracted X-ray intensity distribution in the vicinity of the (013) Bragg peaks of 1000 Å LCMO films on LSAT substrates. And on STO, shown in Fig.4.16. All LCMO films on these substrates are strained to the substrate and the shift of the out-of-plane Q value is clearly visible. Note that the shift of the out-of-plane Q value corresponds to the change of the out-of-plane lattice constant obtained from the $\theta - 2\theta$ XRD scans. In the 1000 Å LCMO film grown on STO substrate at 0.27 mbar oxygen pressure, the shape of the diffraction peak is distorted in an asymmetric way. This is related to a partial relaxation of the crystal structure in the film. The strain-free island formation takes place earlier in this film compared to the other samples grown at lower oxygen pressures.

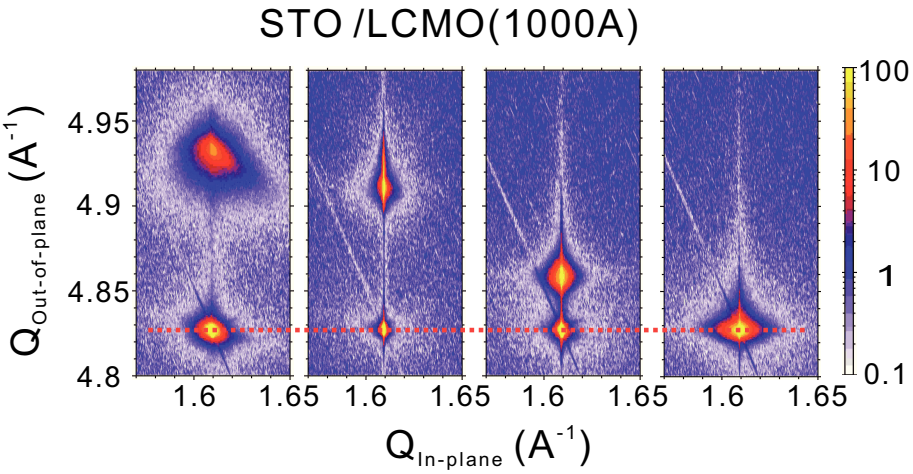

Figure 4.16: Reciprocal space maps of 1000 Å LCMO on STO around (013) STO diffraction peak. The figures are corresponding to the samples grown at 0.27, 0.2, 0.13 and 0.1 mbar from the left to the right. The dotted line indicates the STO (013) diffraction position.

Fig.4.17 shows RSM plots of the (013) LCMO Bragg peak for 1000 Å films grown on LSAO substrates at different oxygen pressures. The in-plane and out-of-plane Qs for the (013) Bragg peak of bulk LCMO are 1.628 Å^{-1} and 4.883 Å^{-1}, respectively, which are far from the (013) Bragg peak in our LCMO films on LSAO. Therefore those films are partially strained compressively and partially relaxed. The out-of-plane Q value of the (013) Bragg peak positions of the samples grown at different growth pressures shows tiny shift from 4.8291 Å^{-1} to 4.8188 Å^{-1}, which is consistent to the small change of out-of-plane lattice constant observed in $\theta - 2\theta$ scan. In addition the shape of the RSM spot changes in the films grown at different oxygen pressures. Paying attention to the change of the shape of the (013) diffraction spots, the broadening of the out-of-plane Q value becomes smaller in the films deposited at lower oxygen pressures. This tendency coincides with the change of the FWHM of the (002) LCMO Bragg peak value presented in Fig.4.14 and is related to the film microstructure. The (013) diffraction spots in the LCMO films deposited at 0.27 and 0.2 mbar oxygen pressures show broadening of both, the in-plane and out-of-plane Q values, indicating the relaxation due to the formation of stress-free or at least stress lean islands. The spots of the atomically smooth films deposited at 0.13 and 0.1 mbar oxygen pressures show a further broadening of the in-plane Q value, but shrinkage of the out-of-plane Q value. This observation indicates that these films have large spread in terms of the in-plane lattice

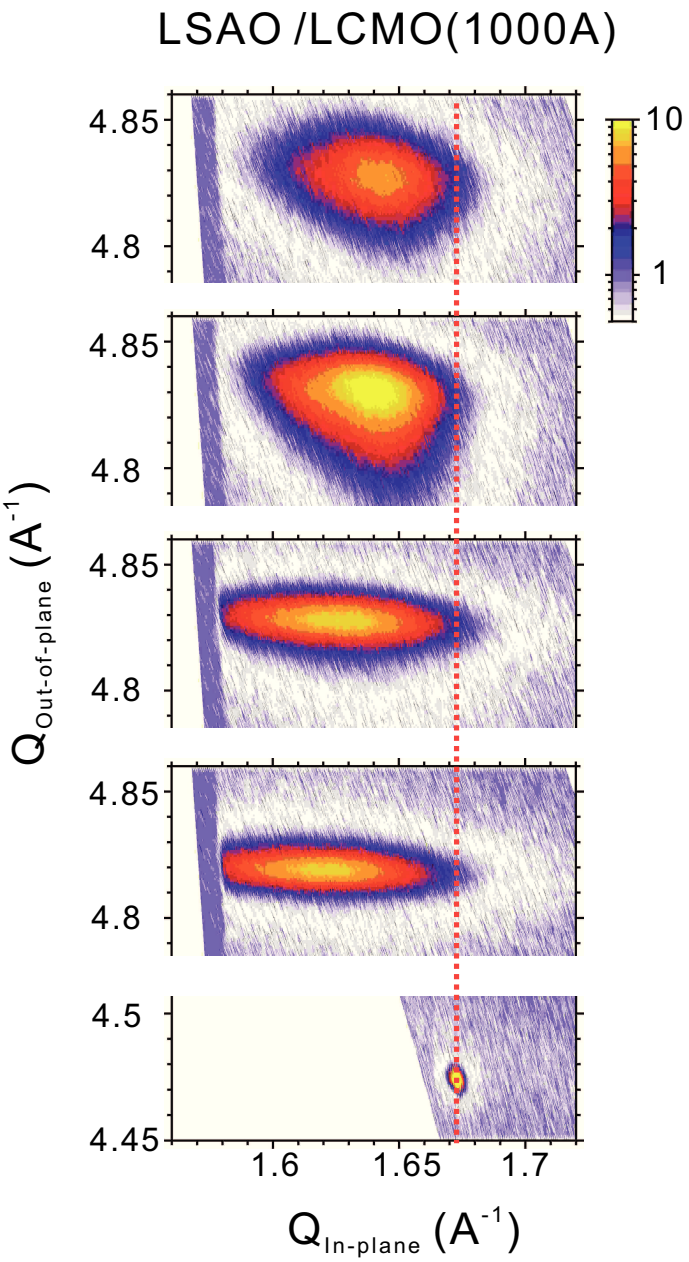

Figure 4.17: Reciprocal space maps of 1000 Å LCMO on LSAO around (013) LCMO diffraction peak. The figures are corresponding to the samples grown at 0.27, 0.2, 0.13 and 0.1 mbar from the left to the right. The dotted line indicates the LSAO (019) diffraction position.

constant but the out-of-plane parameter is more homogeneous. Taking into account the fact that the LCMO films grown on LSAO substrates at low oxygen pressure shows surface steps in the AFM image (shown in Fig.4.11) while films grown at higher oxygen pressure are rough, we conclude that change of the shape of the (013) Bragg spots is caused by the change of the LCMO film microstructure. The compressive strain is accommodated by creating twin domains, which has been observed not only in manganites [93,94] but also in perovskite $LaNiO_3$ [95] when they are in a compressive strain.

Magnetism and transport measurements

The results of transport and magnetism measurements on the samples grown at 0.27 mbar are shown in Fig.4.18. The magnetic moments of the 1000 Å LCMO thin films on LSAT and LSAO show a sharp ferromagnetic transition with high T_{Curie} of 230.4 K and 229.0 K, respectively. On the other hand, the 1000 Å LCMO film on STO substrate shows a broad transition with suppressed T_{Curie} of 171 K compared to the other samples. From the transport measurement, the peak temperatures in the LCMO films on LSAT and LSAO are 241.5 K and 242.1 K, respectively, which are higher than that of the LCMO on STO where T_{Curie} is 206.6 K. The magnetoresistance ratio reaches its peak at the peak temperatures, and the values are about 0.99. This high magnetoresistance ratio indicates a high quality of crystalline structure of the LCMO thin films.

The results on the samples grown at 0.2 mbar are shown in Fig.4.19. The temperature dependence of the magnetic moment shows that T_{Curie} is suppressed in the LCMO on STO and LSAT. On the other hand, the LCMO on LSAO substrate keeps high T_{Curie} of 232.2 K. Peak temperature is also suppressed in the LCMO on STO and LSAT. And in the LCMO on LSAO, the peak temperature was not influenced that much. The magnetoresistance ratios of all the samples are almost 0.99 as a reflection of good crystalline structures.

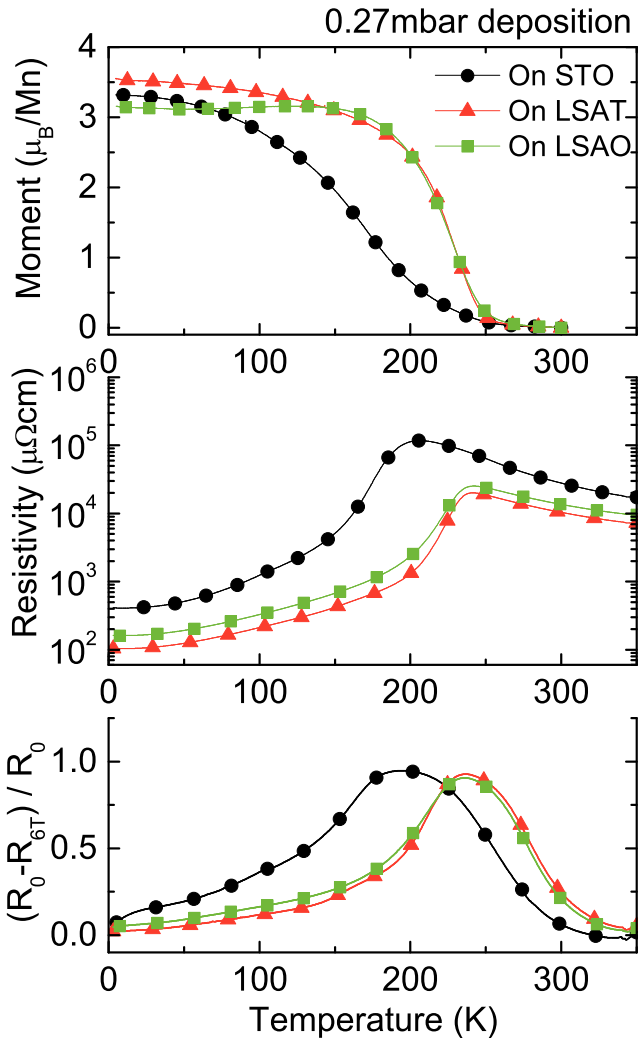

Figure 4.18: Temperature dependence on the magnetic moment, resistivity and magnetoresistance defined by $(R_0 - R_{6\mathrm{T}})/R_0$, where R_0 and $R_{6\mathrm{T}}$ are the resistance without external field and with field of 6 T perpendicular to the sample plane, of the 1000 Å LCMO thin film grown at 0.27 mbar on the different substrate. The magnetic moment was measured in cooling process with the external field of 3000 Oe parallel to the plane.

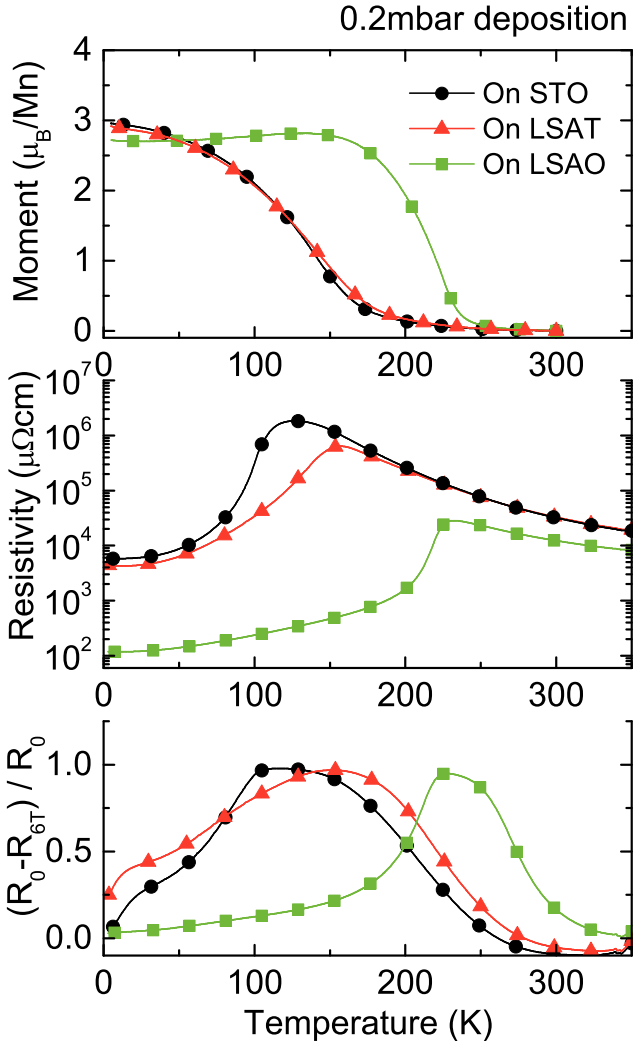

Figure 4.19: Temperature dependence on the magnetic moment, resistivity and magnetoresistance measured with field of 6 T perpendicular to the sample plane, of the 1000 Å LCMO thin film grown at 0.2 mbar on the different substrate. The magnetic moment was measured in cooling process with the external field of 3000 Oe parallel to the plane.

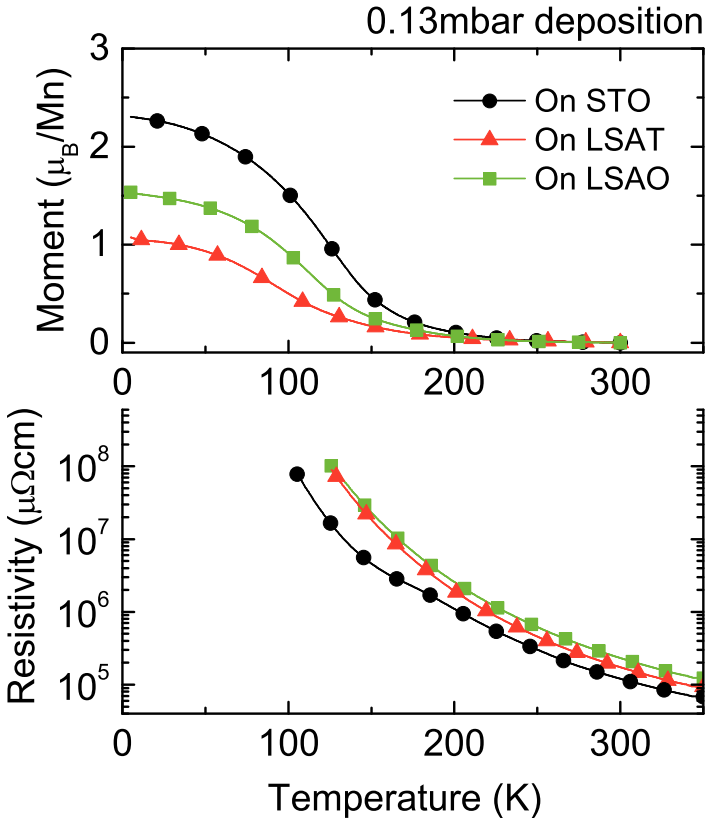

Figure 4.20: Temperature dependence on the magnetic moment and resistivity of the 1000 Å LCMO thin film grown at 0.13 mbar on the different substrate. The magnetic moment was measured in cooling process with the external field of 3000 Oe parallel to the plane.

The samples grown at 0.13 mbar show further suppressed T_{Curie}'s as shown in Fig.4.20. The T_{Curie}'s are 128.0, 93.7 and 114.7 K for the LCMO films on STO, LSAT and LSAO, respectively. The temperature dependences show a granular curve, which indicates an existence of inhomogeneous phases. All samples show semiconductor-like behaviors with an increase of the resistance as the temperature decreases.

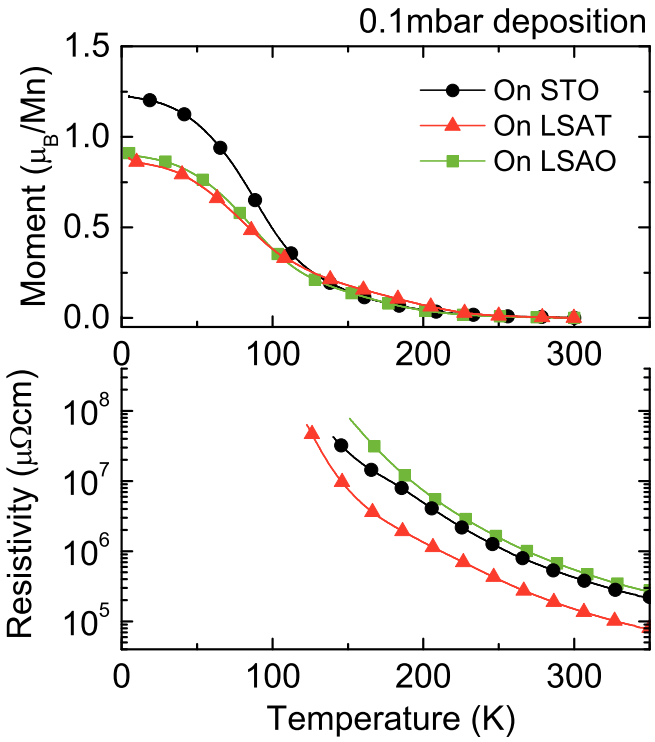

Figure 4.21: Temperature dependence on the magnetic moment and resistivity of the 1000 Å LCMO thin film grown at 0.1 mbar on the different substrate. The magnetic moment was measured in cooling process with the external field of 3000 Oe parallel to the plane.

The magnetic and transport measurements on the samples grown at 0.1 mbar are shown in Fig.4.21. The Curie temperatures are reduced as 91.6, 88.4 and 89.3 K for the LCMO film on STO, LSAT and LSAO, respectively. The inhomogeneity was enhanced, and the magnetic moments are very low. The resistance increases as the temperature decreases.

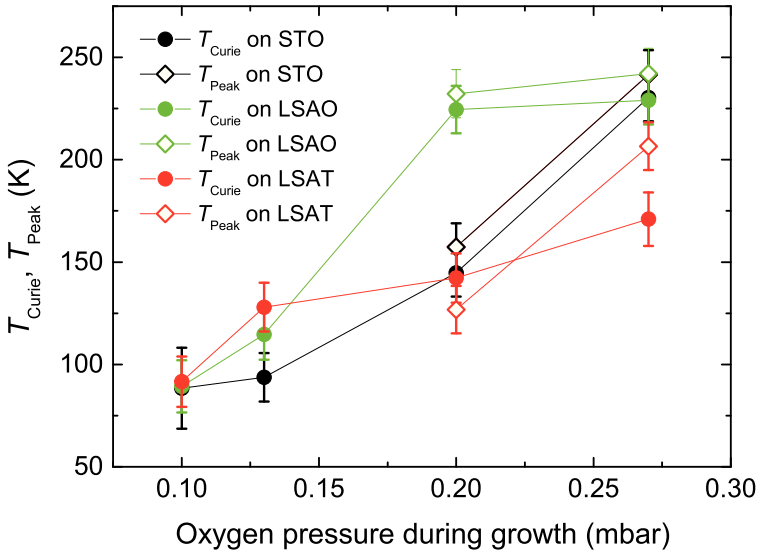

Figure 4.22: Dependence of the Curie temperature and the peak temperature of 1000 Å LCMO films on the oxygen pressure during growth. The error bars take account of a standard error from sample to sample grown at the same condition and a standard error originating from parameter fitting.

In Fig.4.22 the Curie temperatures are summarized as a function of the oxygen pressure during growth. T_{Curie} is determined as the temperature where the derivative, dM/dT of magnetization M measured at 3000 Oe parallel to the film in the field cooling (FC) regime shows the maximum. T_{Peak} is determined from the transport measurement as the temperature where the resistivity has its maximum. The samples grown at oxygen pressures lower than 0.13 mbar show semiconductor-like behavior within the measurable temperature range, therefore no T_{Peak} values are observed for these films (see Fig.4.22). The other physical properties such as saturation magnetization M_{S}, residual resistivity ρ_{R} and coercive field H_{C} are summarized in Table.4.1.

The LCMO film grown on LSAT substrate at 0.27 mbar oxygen pressure has a saturation magnetization of 3.6 μ_{B}/Mn, in good agreement with the value, 3.7 μ_{B}/Mn for a bulk $La_{0.7}Ca_{0.3}MnO_3$. The residual resistivity ρ_{R}, which is related to scattering of carriers due to defects, can be used as an indicator of the quality of the crystallinity [96]. It is 104 $\mu\Omega$cm which is similar to the values of the LCMO films reported in

On STO

P_{Growth}(mbar)	0.27	0.2	0.13	0.1
$M_S(\mu_B/Mn)$	3.3	3.0	2.3	1.2
$\rho_R(\mu\Omega cm)$	411	5867	—	—
H_C(Oe)	254.4	357.3	286.0	547.2

On LSAT

P_{Growth}(mbar)	0.27	0.2	0.13	0.1
$M_S(\mu_B/Mn)$	3.6	2.9	1.1	0.9
$\rho_R(\mu\Omega cm)$	104	4412	—	—
H_C(Oe)	57.6	114.3	375.0	341.0

On LSAO

P_{Growth}(mbar)	0.27	0.2	0.13	0.1
$M_S(\mu_B/Mn)$	3.2	2.7	1.5	0.9
$\rho_R(\mu\Omega cm)$	161	118	—	—
H_C(Oe)	358.2	309.9	472.4	652.4

Table 4.1: List of the physical properties such as saturation magnetization M_S, residual resistivity ρ_R and coercive field H_C of 1000 Å LCMO films.

the literature [96, 97]. The coercive field, H_C, shows a quite small value of 57.6 Oe, indicating a weak pinning of the Bloch walls by intrinsic defects.

The tensile-strained LCMO film on STO substrate grown at 0.27 mbar oxygen pressure shows reduced $T_{\text{Curie}} \simeq 171$ K compared to LCMO films grown on LSAT and LSAO substrates at 0.27 mbar. We consider two possible scenarios for this reduction of T_{Curie}: (i) an extension of the Mn-O bond length due to tensile strain and (ii) the oxygen deficiency. According to the double exchange mechanism stretching of the Mn-O bonds length due to a tensile strain suppresses the probability of electron hopping, then the ferromagnetism is weakened and T_{Curie} is reduced [98]. The oxygen deficiency could also cause a reduction of T_{Curie} since the oxygen vacancies in the crystal modifies the manganese valence from Mn^{4+} to Mn^{3+} by giving additional electrons. The reduction of T_{Curie} due to the extension of the Mn-O bonds length is observed in the thin LCMO films in which the effective tensile strain is strong, and the effect disappears in the thick films with the thickness more than 1000 Å [99, 100]. Therefore, taking account of the thickness of our LCMO films, the reduction of T_{Curie} is related to the oxygen deficiency. In addition, the onset of the magnetic transition shown in Fig.4.23, is at around 250 K in all LCMO films grown at oxygen pressure 0.27 mbar, however the magnetic transition is broad in tensile-strained LCMO film on STO substrate compared with films grown on LSAT and LSAO substrates. Similar broadening of the magnetic transition is observed in the LCMO films grown at lower oxygen pressures. The transition broadening increases as the growth oxygen pressure reduces (see the case of LCMO film on LSAT substrate shown in Fig.4.23). Thus the LCMO film grown on STO substrate at 0.27 mbar oxygen pressure has certain concentration of the oxygen vacancies. Most likely the oxygen vacancies are induced to accommodate the tensile strain [27]. Relatively large residual resistivity 411 $\mu\Omega$cm in this film, which is 4 times larger than in the LCMO film on LSAT substrate, supports this conclusion. Indeed the oxygen vacancies are electronic defects and scatter charge carriers. The Curie temperature also reduces due to the presence of oxygen vacancies in this LCMO film under tensile strain.

The LCMO films grown at 0.2 mbar oxygen pressures on STO and LSAT substrates show reduced T_{Curie} and T_{Peak}, and an increase of the residual resistance. The LCMO films grown at 0.13 and 0.1 mbar oxygen pressures on STO and LSAT substrates are insulating with significantly reduced magnetism. Taking into account that the out-of-plane lattice constant also increase as oxygen pressure decreases, these tendencies are ascribed to increase of the concentration of oxygen vacancies. As the oxygen deficiency increases, the manganese valence changes and causes

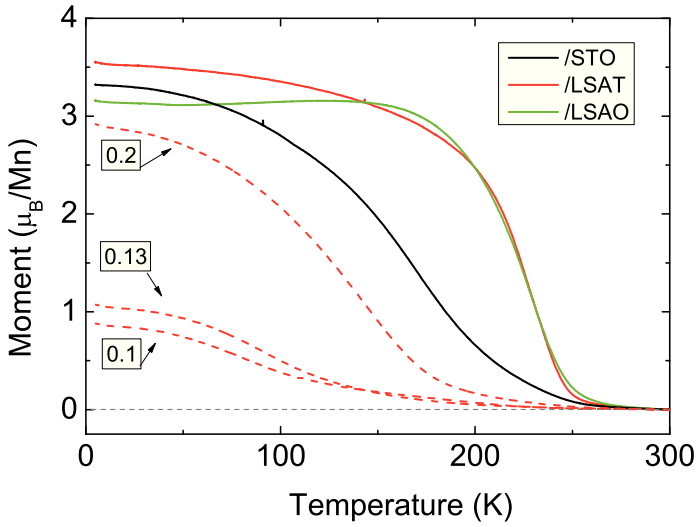

Figure 4.23: Magnetic moments during field cooling process under external field of 3000 Oe. The bold curves indicate the magnetic moments of 1000 Å LCMO films grown at 0.27 mbar on STO, LSAT and LSAO substrates. The broken lines show the moments of 1000 Å LCMO on LSAT grown at 0.2 0.13 and 0.1 mbar from the top line to the bottom one.

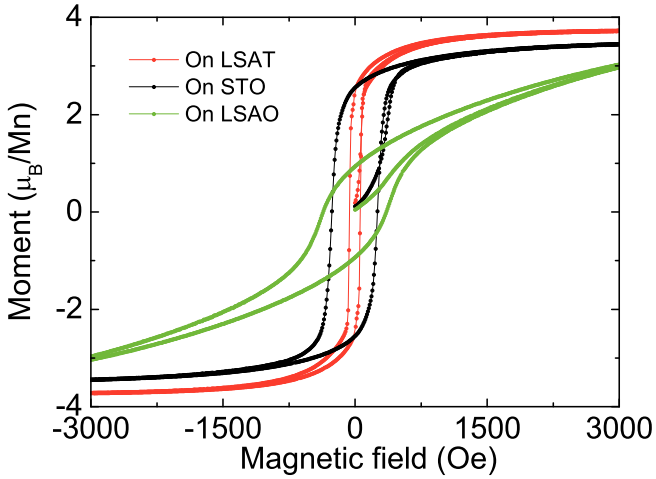

Figure 4.24: Magnetic loop at 5 K on the 1000 Å LCMO samples grown at 0.27 mbar.

the reduction of the magnetic moment together with T_{Curie} as well as T_{Peak} and M_{S}. The residual resistivity also increases significantly.

The Curie temperature of LCMO film on LSAO substrate grown at 0.2 mbar oxygen pressure does not change compared to the film grown at 0.27 mbar. The values of ρ_{R} are 161 and 118 $\mu\Omega$cm for the samples grown at 0.27 and 0.2 mbar, respectively, and those are similar to the one of fully oxygenated LCMO grown on LSAT at 0.27 mbar. This indicates that in the LCMO films grown on LSAO substrate the generation of oxygen vacancies is less favorable than in the films grown on STO and LSAT substrates in the same growth condition. The compressive strain supports the oxidization of LCMO films. The magnetization hysteresis loops at 5 K for LCMO grown at 0.27 mbar on different substrates are shown in Fig.4.24. The magnetic moment for film grown on LSAO substrate is not saturated at the field of 3000 Oe, where LCMO films on STO and LSAT substrates get saturated. This indicates that spins are strongly pinned due to structural distortion caused by a compressive strain.

LCMO films grown on LSAO substrate at 0.13 and 0.1 mbar show the insulating behavior without a characteristic peak of resistivity in the transport measurement. T_{Curie}'s are 115 K and 89 K, respectively, and the ferromagnetic moments are also reduced as shown in Table.4.1. In these cases, there are two possible reasons for the reduction of conductivity and ferromagnetism. One is the oxygen deficiency, similar to the

cases of LCMO on STO and LSAT. Although the out-of-plane lattice parameter does not show a noticeable change, there is distinct spread in the in-plane parameter (Fig.4.17). Therefore a certain amount of oxygen vacancies could be generated in the crystal system despite of the epitaxial compressive strain. The second possible reason is that the creation of twin domains disturbs electron hopping and suppresses the double exchange mechanism. As discussed in RSM of Fig.4.17, the shape of (013) diffraction spot of the samples grown at 0.13 and 0.1 mbar indicates a formation of twin domains, where the domains tilted with each other by an identical angle to accommodate the compressive strain. At the interfaces between tilted domains the connection between adjacent MnO_6 octahedra is distorted. The double exchange interaction gets suppressed and the electrons are localized. Accordingly the conductivity and ferromagnetism are suppressed. It is also likely that both effects are combined, namely, the oxygen vacancies can be accommodated by forming twin domains. In this case, both of the oxygen vacancies and the distortion of octahedral contribute on the suppression of the conductivity and ferromagnetism.

4.1.4 Summary of the section

The 100 Å LCMO thin films were grown on three different substrates, STO, LSAT and LSAO, and four different oxygen pressures for growth, 0.27, 0.2, 0.13 and 0.1 mbar, were used in order to change the concentration of the oxygen vacancies. According to XRD analysis, the quality of crystal structure is good, and the oxygen deficiency becomes larger as the oxygen growth pressure becomes smaller, enabling us to perform a systematic study on the interrelation between strain and oxygen deficiency. The shift of the (002) X-ray diffraction peak due to the change of the oxygen growth pressure is large in the film with tensile strain, and it is suppressed in the film with compressive strain. This clearly indicates the entanglement of the strain and the oxygen deficiency, that is, oxygen vacancies are induced to accommodate tensile strain and compressive strain suppresses the formation of oxygen vacancies. Even in the transport and magnetic measurements, the same tendency was observed. Tensile-strained LCMO film on STO substrate grown at 0.27 mbar shows suppressed T_{Curie} and high residual resistivity because of the induced oxygen vacancies, while LCMO film on LSAT and LSAO substrates showed sharp transition with high T_{Curie} and small ρ_{R}. Changing the oxygen pressure from 0.27 mbar to 0.2 mbar, T_{Curie} and ρ_{R} in compressive-strained LCMO film on LSAO substrate were stable compared to LCMO films on STO and LSAT substrates since the compressive strain suppresses formation of oxygen vacancies.

4.2 Superconductivity in $YBa_2Cu_3O_{7-d}/La_{1-x}Ca_xMnO_3$ bilayers (x=0.3, 0.45, 0.55 and 0.8)

4.2.1 Overview of this section

This section addresses the general problem of the interplay between two different and antagonistic ground states in complex oxides by the special case of YBCO and $La_{1-x}Ca_xMnO_3$ (hereafter, in this section, notation of LCMO is applied for general class of Ca doped Lanthanum manganite $La_{1-x}Ca_xMnO_3$).

In the YBCO compound, high temperature superconductivity is influenced by the various defects such as oxygen vacancies [32], as well as on cation disorder [101, 102] and substitution [103, 104]. In the LCMO material the magnetic and electronic properties are strongly dependent on the Ca concentration x [105]. A comprehensive study of YBCO/LCMO bilayers with a different Ca concentration in LCMO is necessary for further understanding of interface phenomena and T_C enhancement or suppression in the YBCO layer. In this part, a comparative study of electrical transport, magnetic and structural properties of YBCO/LCMO bilayers grown by pulsed laser deposition on $SrTiO_3$ (001) substrates will be presented.

The YBCO and LCMO layer thicknesses were fixed at 4 unit cells (u.c.) $\sim$ 47 Å and 200 Å, respectively, while the Ca doping concentration in the LCMO layer was systematically changed. This YBCO layer thickness was selected because T_C is strongly influenced by an adjacent LCMO layer when the thickness of YBCO layer is 50 Å [73]. The Ca doping, x, in the LCMO layer was changed from one sample to the other with x= 0.3, 0.45, 0.55 and 0.8. According to the phase diagram [106], LCMO with these doping concentrations correspond to the FM state for x=0.3, FM plus CE-type antiferromagnetic (AFM) state for x=0.45, and CE-type AFM and C-type AFM for x=0.55 and x=0.8, respectively. If a charge transfer of spin polarized electrons from LCMO to YBCO is the main mechanism of T_C reduction this effect would be differentiated by the Fermi levels (E_F) in the band diagrams of the layers and the concentration of spin polarized electrons. E_F of LCMO compounds decreases in almost linear manner as Ca concentration increases [107], and E_F is consistently larger in LCMO than in YBCO irrespective of x [108]. Therefore, one expects that the strongest suppression of T_C should be observed at low doping level x=0.3, where LCMO layer is ferromagnetic half-metal with 100% spin polarized electron carriers. The smallest T_C suppression is expected for x=0.8 where the LCMO layer is an AFM insulator. As a result of our analysis, however, we observed that the T_C reduction tendency is opposite to what is expected, namely,

the obvious reduction compared to a single 4 u.c. YBCO was present in the YBCO/LCMO bilayer with x=0.3 and as the Ca concentration increased a suppression of T_C was enhanced. In the bilayers an LCMO layer of x=0.8, the superconducting transition was absent for the entire temperature range down to 4.2K.

In order to explain this finding we must draw attention to the fact that a change of Ca doping x in LCMO modifies not only the magnetic phase but also the lattice parameters of the LCMO unit cell. The largest lattice mismatch between YBCO and LCMO occurs for x=0.8 where no superconductivity was found. We argue that in our YBCO/LCMO bilayers the main mechanism of the T_C suppression is related to the crystal structure. Lattice mismatch is predominantly responsible for a creation of oxygen deficiency in the YBCO layer and an enhancement of Ca intermixing which causes Ca doping into the YBCO and a cation disorder effect.

4.2.2 Experiments

A single layer YBCO thin film and YBCO/LCMO bilayer samples were fabricated by PLD. We used five different targets: the YBCO target was synthesized in TOSHIMA Manufacturing Company (Japan) and four LCMO targets with different Ca concentration x=0.3, 0.45, 0.55 and 0.8 were provided by Kurt Lesker Company (U.K.). STO (001) single crystal substrates from Crystec Company (Germany) with dimensions of $5 \times 5 \times 0.5$ mm^3 were used after TiO_2 termination [109]. For the PLD deposition a KrF excimer laser with a wave length of 248 nm was utilized. The energy density on the target was set to 1.8 J/cm^2. The frequencies of the pulsed laser were 2 and 3 Hz for YBCO and LCMO, respectively.

The thickness of the YBCO layer was fixed at 4 u.c. ($\sim$ 47 Å) in all samples. The *in-situ* reflection high energy electron diffraction (RHEED) of the specular spot was monitored during growth. The RHEED intensity oscillation pattern obtained during deposition of a 4 u.c. YBCO layer is shown in Fig.4.25.

In all YBCO/LCMO bilayers the YBCO layer was deposited first and the LCMO layer was grown on top of YBCO. The thickness of the LCMO layer was kept at 200 Å. We fabricated four different bilayers: (i) YBCO/ $La_{0.7}Ca_{0.3}MnO_3$ (denoted as YL.3), (ii) YBCO/$La_{0.55}Ca_{0.45}MnO_3$ (YL.45), (iii) YBCO/$La_{0.45}Ca_{0.55}MnO_3$ (YL.55) and (iv) YBCO/$La_{0.2}Ca_{0.8}MnO_3$ (YL.8). The substrate was heated by an infrared laser and kept at 760 °C while controlled by a radiation pyrometer. The oxygen pressure during growth of the bilayers and the single YBCO film was 0.27 mbar. After the deposition, all the single film and bilayers were post-annealed: first

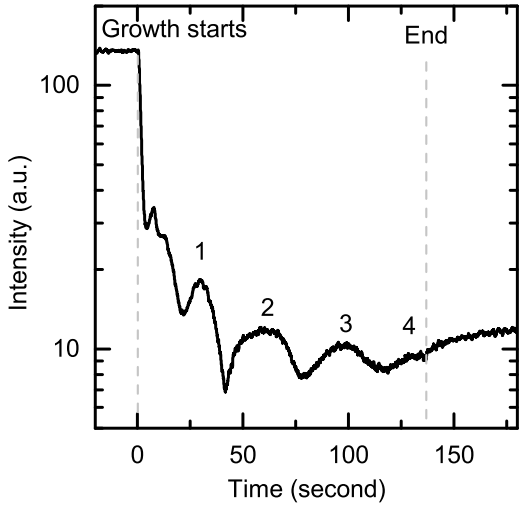

Figure 4.25: Time dependence of the RHEED intensity of the specular spot during growth of the YBCO layer.

they were cooled to 520 °C with ramp rate of 5 °C/min, afterwards the oxygen pressure was increased to 1 bar. In order to fully oxidize YBCO layer the post-annealing time lasted for 20 min in case of single YBCO film and 40 min for all bilayers. The bilayer samples needed longer post-annealing time to provide complete saturation of oxygen content in the bottom YBCO layer because the upper LCMO layer hampers the oxygenation process. When the post-annealing was finished, an infrared laser heater was turned off. The sample ID, the structures, as well as T_{C}, Curie temperature T_{Curie} and saturation magnetization M_{S} at 50 K are summarized in Table 4.2.

Each sample was characterized by different techniques. To determine the phase purity and crystalline orientation we utilized a Bruker AXS-D8 X-ray diffractometer with CuKα radiation (λ=0.1541 nm). The superconducting transition temperature T_{C} was determined by mutual inductance set-up from a room temperature down to 4.2 K with transmission geometry, i.e., the samples were located between the drive and pick-up coils. The AC drive coil current was 60 μA at a frequency of f=1.6 kHz. Taking account of the geometry of the driving coil and the number of turns (300 times), this current corresponds to $\sim$ 0.28 Oe. The temperature dependence on the magnetic moment was measured by a vibrating sample magnetometer (VSM) SQUID in field-cooling (FC) process with

Sample ID	Structure	T_C[K]	T_{Curie}[K]	M_S [μ_B/Mn]
YBCO	Single YBCO	65.1	---	---
YL.3	YBCO / $La_{0.7}Ca_{0.3}MnO_3$	49.2	215.78 ± 2.85	3.07
YL.45	YBCO / $La_{0.55}Ca_{0.45}MnO_3$	44.1	214.49 ± 4.47	0.33
YL.55	YBCO / $La_{0.45}Ca_{0.55}MnO_3$	27.3	---	0.07
YL.8	YBCO / $La_{0.2}Ca_{0.8}MnO_3$	---	---	0.04

Table 4.2: Summary of a sample ID, corresponding structure, and physical properties such as T_C, T_{Curie} and M_S. M_S was taken from the moment at 50 K during FC process under 3000 Oe.

an external field of 3000 Oe parallel to a sample plane. The in-plane transport measurements were performed by a PPMS Quantum Design system from 5 K to 300 K with a four-point contacts configuration.

4.2.3 Results

Fig.4.26 shows a magnification of the x-ray diffraction $\theta - 2\theta$ scans of a single layer YBCO film and four bilayers. The YBCO (005) and STO (002) diffraction peaks appear at $\sim 38.6^\circ$ and $\sim 46.5^\circ$, respectively. A position of the LCMO (002) diffraction peak shifts from $2\theta = 47.2^\circ$ to 48.9° as the doping concentration increases from 0.3 to 0.8. This shift is attributed to a contraction of the out-of-plane lattice parameter upon substitution of La ion by Ca which has a smaller ionic radius [110]. Because the YBCO film is very thin (4 u.c.), the full width at half maximum (FWHM) of the YBCO (005) peak is $\sim 1.7^\circ$, which is consistent with a rough estimation by using Scherrer formula $\Delta = 0.9 \cdot \lambda/(L\cos(\theta))$, where λ and L are the wave length of the X-ray and the thickness of the film, respectively, and Δ is the FWHM of the diffraction peak centered at 2θ. Typically for reference YBCO films with a thickness of 1000 Å the FWHM is $0.2 \sim 0.4^\circ$. Two sharp diffraction peaks at $\sim 38.2^\circ$ and $\sim 44.5^\circ$ are ascribed to diffraction from the sample holder as shown in the bottom of Fig.4.26.

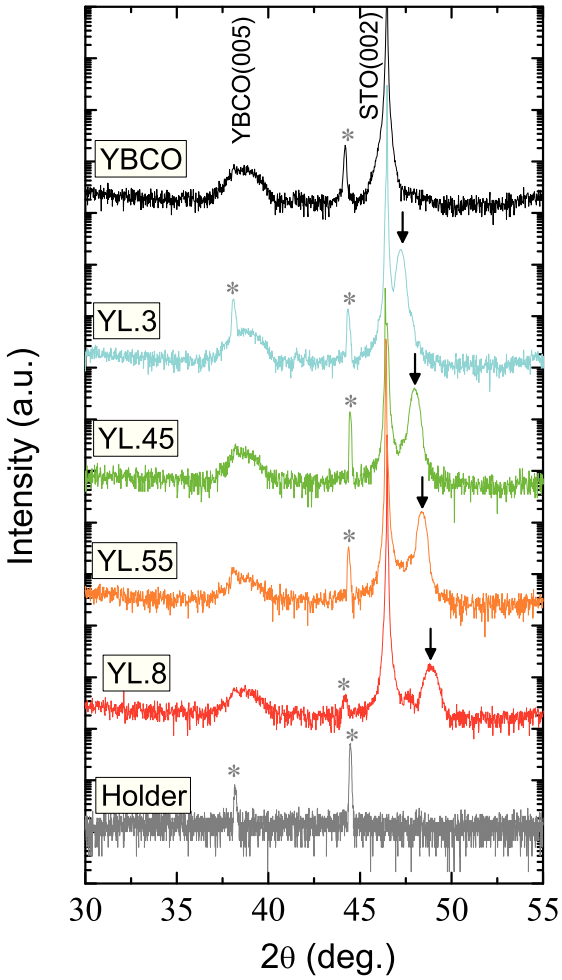

Figure 4.26: XRD $\theta - 2\theta$ scans around YBCO (005) diffraction peak and LCMO (002) peak including STO (002) peak. The lines correspond to single YBCO, YL.3, YL.45, YL.55 and YL.8 from the top to the lowers. The arrow indicates the LCMO (002) peak position which shifts with the change of Ca concentration x. The bottom indicates the background diffraction measured without a sample, where the peaks from the holder are shown. For clarification, asterisk symbols (*) are added on the holder peaks

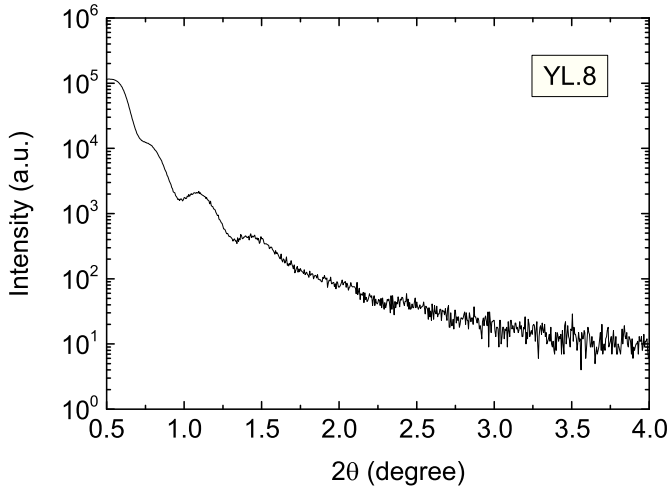

Figure 4.27: Small angle X-ray reflectivity measurement on the bilayer YL.8.

A small angle X-ray reflectivity measurement was performed for each bilayer sample. In Fig.4.27, the result on the bilayer YL.8 is shown. The result exhibits Kiessig oscillations, indicating the smooth sample surface. The thickness obtained from Kiessig oscillations is $\sim$ 250 Å, which is consistent with the expected thickness. The oscillation with similar pattern was confirmed even in the other bilayer samples.

T_C was determined from the AC susceptibility measured by a mutual inductance set-up. A response of a pick-up coil is a complex number with real Re(χ) and imaginary Im(χ) parts corresponding to the in-phase (dissipative) and 90 degrees out-of-phase (inductive) couplings between the coils. This result is shown in Fig.4.28. T_C was determined by the temperature where the Im(χ) signal departs from the value in normal state. The single 4 u.c. YBCO thin film shows T_C of $\sim$ 65.1 K. This value of T_C for a YBCO ultrathin film is consistent with literature [73] and much lower than T_C of bulk YBCO ($\sim$ 92 K). In YBCO/LCMO bilayers T_C is even further reduced as follows: 49.2 K in YL.3, 44.1 K in YL.45, and 27.3 K in YL.55, respectively. The bilayer composed of an LCMO layer with a Ca concentration of 0.8 (YL.8) was not superconducting in the entire temperature range down to 4.2 K.

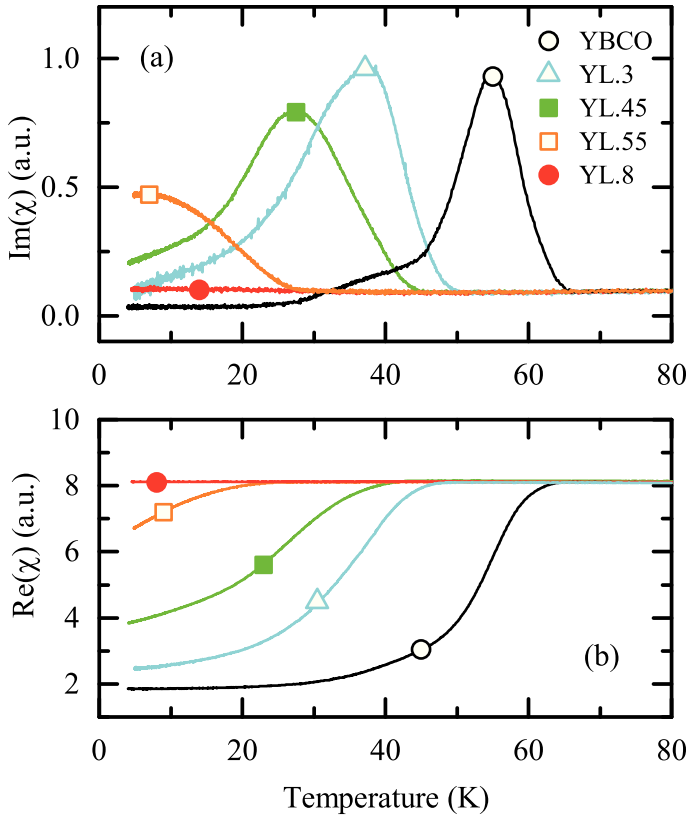

Figure 4.28: Temperature dependence of AC-susceptibility. Im(χ) and Re(χ) are shown in (a) and (b), respectively.

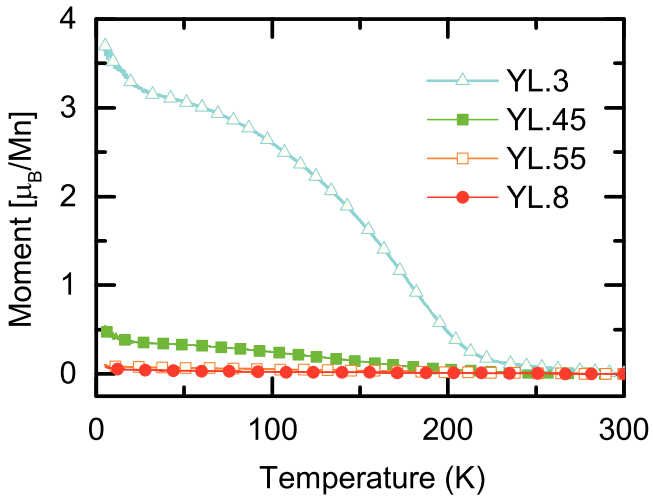

Figure 4.29: Temperature dependence on a magnetic moment of the bilayer samples with an external field of 3000 Oe parallel to a sample plane.

The field cooled temperature dependences of magnetic moments for different YBCO/LCMO bilayers are shown in Fig.4.29. The magnetic moment was converted to Bohr magneton per one Mn atom (μ_B/Mn) based on 200 Å (the thickness of LCMO layer). First, one can clearly see that the ferromagnetic moment is observed only in two bilayers: Ca doping of x=0.3 and 0.45. In bilayers composed of YBCO and LCMO layers with x=0.55 and 0.8, the magnetization is close to zero in the measured temperature range as expected for the AFM ground state. From these temperature dependences we extracted the Curie temperature for two ferromagnetic LCMO layers as a cross-point of a linear extrapolation of $M(T)$ with the highest derivative dM/dT and another extrapolation from the high temperature region where $M(T) = 0$. The saturation magnetization M_S was determined at $T = 50$ K. In comparison with bulk parameters of LCMO with x=0.3 ($T_{Curie} \sim 270$ K and $M_S \sim 3.7$ μ_B/Mn) the YL.3 bilayer shows reduced values of $T_{Curie} \sim 216$ K and $M_S \sim 3.0$ μ_B/Mn. This is a consequence of the small layer thickness and epitaxial tensile strain [66, 97]. For the bilayer YL.45 where the LCMO layer belongs to FM plus CE-type AFM phases, we found $T_{Curie} \sim 214$ K and $M_S \sim 0.33$ μ_B/Mn. The saturation moment is strongly reduced compared with M_S of 3.0∼3.4 μ_B/Mn for polycrys-

talline samples [111, 112]. This reduction could be related to the epitaxial strain via a lattice mismatch with the bottom YBCO. According to the bulk phase diagram for LCMO [113], the compound with x=0.45 is close to a charge-ordered AFM state and this state can be easily induced in thin films due to the tensile strain [114, 115]. The YL.55 and YL.8 bilayers with LCMO layers of x=0.55 and 0.8 respectively did not show any ferromagnetic response as is expected for the AFM ground state for the corresponding doping x. The two superconducting bilayers (YL.3 and YL.45) showed a paramagnetic moment below T_C of the YBCO layer. A similar paramagnetic response was previously reported for YBCO/LCMO superlattices [116,117] and was interpreted as a result of the magnetic flux compression in a superconducting layer caused by the presence of magnetic LCMO layer. The explanation of this effect is still under discussion.

Figs.4.30(a) and (b) plot resistance versus temperature for the four bilayers and one 4 u.c. YBCO film. The superconducting transition temperature for the thin YBCO film, $T_C(R{=}0) \sim 63$ K, is in a good agreement with T_C obtained from mutual inductance measurements. The resistance has a linear temperature dependence above T_C. The $R(T)$ dependence of three bilayers: YL.3, YL.45 and YL.55 are shown in Fig.4.30(a) and YL.8 is presented in Fig.4.30(b).

Due to an interplay between resistances of YBCO and LCMO layers, a metal to insulator transition (T_{MI}) appeared in the $R(T)$ curves for all bilayers except for YL.8. The metal to insulator transition temperature T_{MI} in YL.3 at 233 K is caused by the contribution of the LCMO layer. On the other hand, $T_{MI} \sim 203$ K in YL.55 cannot be ascribed to the LCMO since LCMO with x=0.55 is insulating in this temperature region. Therefore, the metal to insulator transition in YL.55 originated from a change in the dominant contribution on the net resistance. That is, LCMO has a lower resistance than YBCO at high temperatures and other way around in the low temperature region. The resistance peak, $T_{MI} \sim 210$ K, in YL.45 should be between of both features. In YL.8 the resistance increases as the temperature decreases and the superconducting transition was absent down to 5 K. This is consistent with the mutual inductance measurement. Taking into account that the LCMO layer with x=0.8 is insulating this result confirms that the YBCO layer in the bilayer YL.8 is not superconducting. All the other bilayers show superconducting transitions in good agreement with T_C measured by mutual inductance set-up and depends on the doping level of the LCMO layer.

A surprising fact is reduction of T_C with increase Ca concentration in LCMO layer trend is counterintuitive, because the LCMO ground state

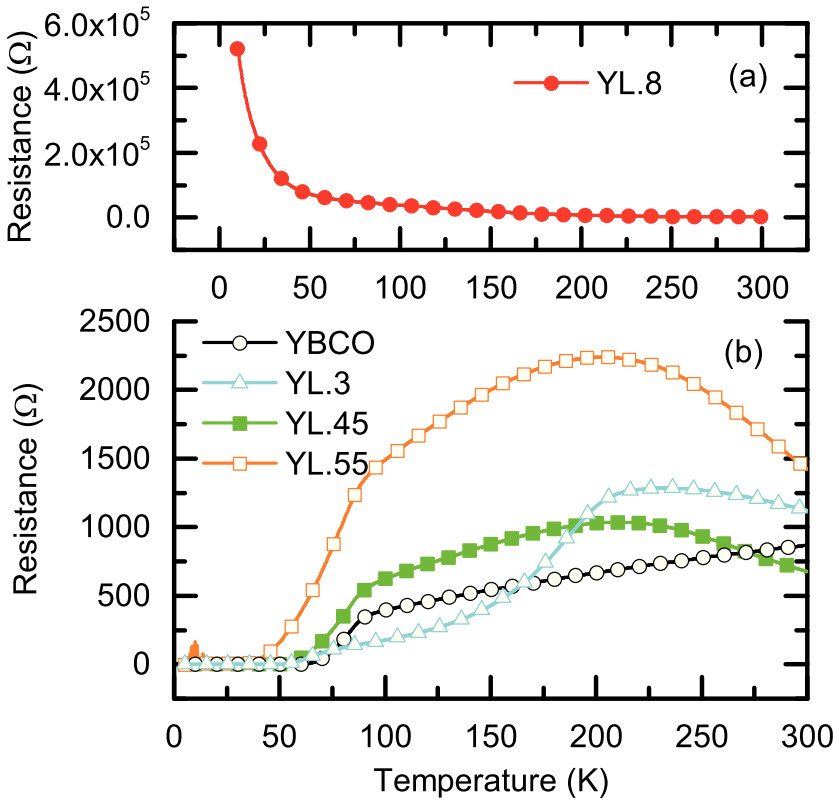

Figure 4.30: Temperature dependence on a resistance of bilayer samples and single YBCO. The result of YL.8 is given in (a). The other samples are shown in (b).

changes from FM half metal to AFM insulator. If the mechanism of the T_C reduction is electronic due to charge transfer of spin-polarized quasiparticles from the LCMO layer into the YBCO and breaking Cooper pairs, the maximum effect should be observed in the YBCO/LCMO bilayer with x=0.3 where the LCMO layer is FM half metallic. The result is robust and opposite, namely, the maximum suppression of the T_C was observed in the bilayer with LCMO (x=0.8) layer which has AFM insulating ground state.

4.2.4 Discussion

Contacting a thin superconducting YBCO layer with other epitaxial oxide layer modifies the interface properties by different mechanisms. First, if Cooper pairs can penetrate and survive in the adjacent layer superconductivity is induced in the proximity of the interface, which is the so-called proximity effect. Simultaneously, the leakage of Cooper pairs weakens the superconductivity near the interface. This effect is called the inverse proximity effect. (Note that, in case of SC/FM junctions, the inverse proximity effect could be affected by magnetism in FM layer.) These phenomena depend on the interface transmission as well as possible pair breaking mechanisms. In case of a junction of YBCO and the FM metal $La_{0.7}Ca_{0.3}MnO_3$, the proximity effect is prohibited due to the of large exchange energy of $La_{0.7}Ca_{0.3}MnO_3$ ($\sim$3 eV) [15]. It is also not likely that proximity effect plays a major role at the YBCO/$La_{0.2}Ca_{0.8}MnO_3$ interface because LCMO with x=0.8 is a charge ordered insulator. In addition, the length scale of the inverse proximity effect is the superconducting coherence length which is small for YBCO (0.1$\sim$0.3 nm) compared to the layer thickness. Accordingly, a conventional proximity effect is not supposed to result in the T_C reduction observed in the YL.8 bilayer. Unconventional proximity effect which could occur due to the interplay of SC and FM states [23, 24] is also incompatible with the T_C reduction observed in YL.8.

The second electronic mechanism is charge transfer driven by a difference in the Fermi levels E_F of neighboring layers. To check the applicability of this approach one needs to know E_F for YBCO and LCMO with different Ca concentration. According to Ref. [108], E_F of the undoped $LaMnO_3$ is $\sim$1 eV larger than that of the optimum doped YBCO. E_F of $La_{1-x}Ca_xMnO_3$ decreases linearly by 0.72 eV as x changes from 0 to 1 [107]. A schematic representation of relative position of E_F for LCMO with x=0.3, 0.45, 0.55 and 0.8 as well as YBCO are depicted in Fig.4.31. Based on this data we can qualitatively consider the impact of this charge transfer mechanism on the superconductivity in YBCO. The larger a difference between E_F in adjacent layers the more electrons

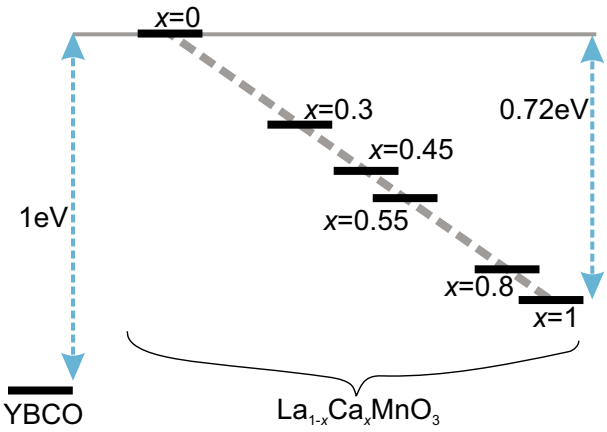

Figure 4.31: Schematic of a relation between E_F of concerned compounds.

are transferred to the YBCO layer and T_C is suppressed. In this picture the largest effect is expected for the YBCO/LCMO bilayer with x=0.3 (YL.3). Surprisingly, we obtained the strongest T_C reduction in YBCO/LCMO bilayer with x=0.8 (YL.8) where the smallest charge transfer is expected from a difference between E_F. Thus the simple charge transfer model cannot be the main mechanism for the reduction of T_C in YL.8. In addition, the carriers in FM LCMO with x=0.3 are fully spin polarized, while in LCMO with x=0.8 the ground state is an AFM insulator. In conjunction with charge transfer mechanism, spin-polarized carriers also do not cause the suppression of T_C in YL.8.

It should be noted that these two mechanisms, proximity effect and charge transfer, are applied for conventional superconducting and semiconducting heterostructures and might be not applicable for complex oxides with strong electronic correlations and lattice structure distortions. Indeed in these materials the crystal structure plays an important role. The properties of the interfacial layers are often determined by several interrelated mechanisms: (i) epitaxial strain due to lattice mismatch between neighboring layers with different lattice parameters, (ii) strong Coulomb interaction between electrons and hybridization of orbitals, and (iii) introduction of different types of defects including oxygen vacancies, intermixing or substituting of cations from an adjacent layer, dislocations and/stacking faults.

First let us compare the lattice parameters for the YBCO and LCMO layers. The in-plane lattice parameters of a strain-free bulk YBCO are 3.823 and 3.887 Å for the a- and b-axis, respectively [32]. To take into account the twinning of YBCO [118], hereafter we take an average

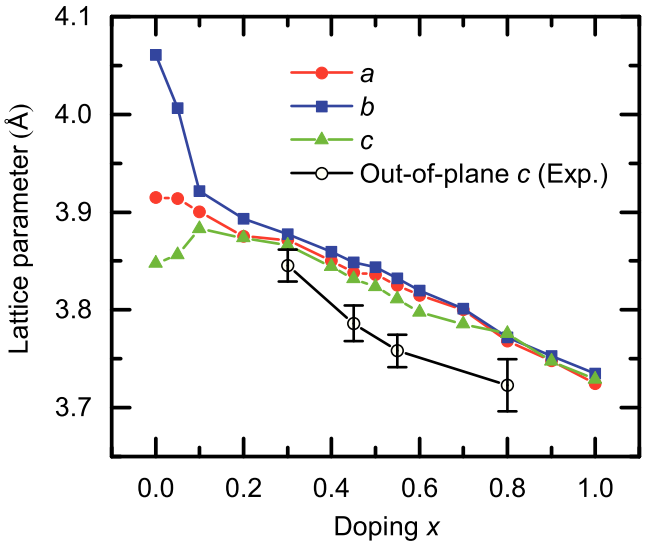

Figure 4.32: Relation of lattice parameters of LCMO and doping x. The lattice parameters of a bulk LCMO are cited from Ref. [119] for x=0 and 0.05, Ref. [120] for x=0.1, Ref. [121] for 0.2, Ref. [122] for x=0.3, Ref. [123] for x=0.4, Ref. [112] for x=0.45, Ref. [124] for x=0.5, Ref. [125] for x=0.55, Ref. [126] for x=0.6, Ref. [127] for x=0.7, Ref. [128] for x=0.8, Ref. [129] for x=0.9 and Ref. [130] for x=1. The out-of-plane lattice parameter of LCMO in bilayer samples are denoted by open circles. The error bar corresponds to FWHM of the LCMO (002) diffraction peak

of a and b, namely 3.855 Å as the in-plane parameter of YBCO. The lattice parameters for bulk LCMO compound as a function of the Ca doping concentration x are presented in Fig.4.32. Here, a, b and c lattice parameters are derived as $a = a_O/\sqrt{2}$, $b = b_O/\sqrt{2}$, and $c = c_O/2$, where a_O, b_O and c_O are the intrinsic orthorhombic lattice parameters cited from references [112, 119–130]. As x approaches 0, the anisotropy of a unit cell is enhanced and a pseudo-cubic approximation of the crystal structure becomes inappropriate. For the region of $x \geq 0.3$, however, a pseudo-cubic approximation is acceptable. The out-of-plane lattice parameters of LCMO in our bilayer samples are derived from LCMO (002) diffraction peak via the Bragg equation, and are also shown in Fig.4.32.

The out-of-plane lattice parameters in the bilayers are smaller than

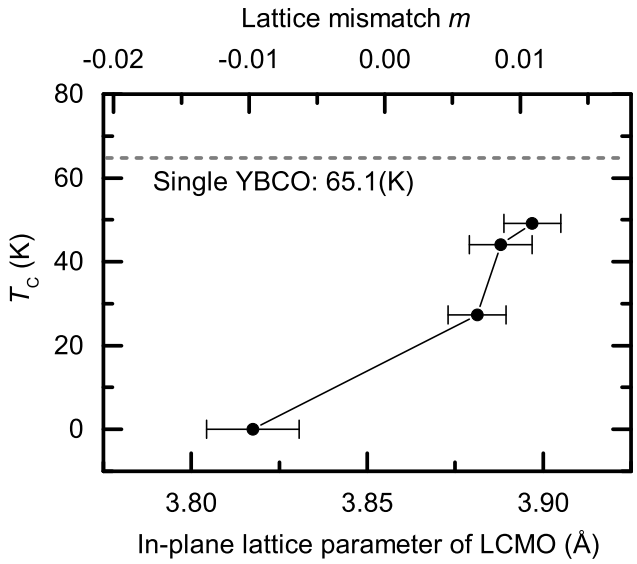

Figure 4.33: Relation of T_C in the bilayer samples and in-plane lattice parameter of LCMO in conjunction with corresponding lattice mismatch m. The error bar originates from the FWHM of LCMO (002) diffraction peak in a XRD measurement.

the c lattice parameter of bulk LCMO. This indicates that all LCMO layers in our bilayers are subjected to an in-plane tensile strain due to lattice mismatch with bottom layer and the unit cell is contracted along out-of-plane lattice direction. This observation has the important implication that the 4 u.c. YBCO layer did not completely reduce the in-plane tensile strain from the STO substrate.

In Fig.4.33, T_C versus in-plane lattice parameter of the LCMO layer in YBCO/LCMO bilayers with different Ca concentration is shown. Here, the in-plane lattice parameter, a_{LCMO}, was derived from the out-of-plane lattice parameter obtained in the XRD measurement with 0.35 as Poisson ratio ν, which is typically $0.3 \leq \nu \leq 0.37$ for manganites [131–135]. In addition an in-plane lattice mismatch m between YBCO and LCMO was calculated as $m = (a_{LCMO} - a_{YBCO})/a_{YBCO}$, where an average bulk value of $a_{YBCO} = 3.855$ Å is adopted since we could not experimentally estimate this parameter due to the small thick-

ness of YBCO. There is a clear correlation between T_C and lattice mismatch m. T_C decreases monotonically with a decrease of the in-plane lattice parameter of LCMO. In the negative m region where YBCO acquires an in-plane compressive strain, the suppression of T_C is significant. From this observation we conclude that the in-plane lattice mismatch between the LCMO and thin YBCO layer has a strong impact on T_C in the YBCO/LCMO bilayers.

Now let us discuss the influence of the in-plane lattice mismatch on the superconductivity in the thin YBCO layer. Here, two possible mechanisms to connect the lattice mismatch and the suppression of superconductivity in YBCO/LCMO bilayers are proposed. The first mechanism is due to defects: oxygen vacancies or Ca intermixing or substitution, and induced disorder in YBCO layer. The other mechanism is electronic, related to a change in the orbital occupancy of the LCMO layer and hybridization of the Cu orbitals in the YBCO layer with increasing Ca doping level. The latter scenario is motivated by the orbital reconstruction and induced nonsuperconducting layer near the interface [74]. Taking into account that the orbital reconstruction in Ref. [74] is driven by tuning the on-site energy on Mn ion and related to charge transfer, this mechanism is not supposed to be responsible for the T_C reduction in YL.8 in an analogous manner to the E_F analysis mentioned above. However, it was pointed out that the origin of orbital reconstruction is not fully understood [73], therefore this scenario cannot be firmly ruled out and requires further experiments.

The defect model, however, is rather plausible since it is hard to believe, from a technological point of view, that defect free bilayers can be synthesized with such a large in-plane lattice mismatch between two layers. T_C in YBCO is determined by several factors. One of them is the oxygen content. It was shown in Ref. [136] that oxygen vacancies are induced in YBCO by a compressive strain from a LSAO substrate and T_C is suppressed more strongly than under a tensile strain from a STO substrate. In our case, a compressive strain is introduced from the top LCMO layer for x=0.3. Unfortunately it is not possible to quantify the strain and oxygen content in ultrathin YBCO layers from simple XRD analysis since the intensities of Bragg peaks are weak and the peaks themselves are broad because of the small thickness. Another possible effect is Ca intermixing from LCMO to YBCO. Chemical intermixing of La and Ba on the interfacial BaO layer or Y and Ca intermixing on the interfacial CuO_2 layer is an open issue [137]. The chemical potential of Ca ions in LCMO with x=0.8 is higher than that of LCMO with x=0.3. Therefore Ca intermixing should be enhanced in YL.8 bilayer compared to YL.3. In addition, the smaller ionic radius of Ca compared to Y ion

facilitates substitution of the Y site by a Ca ion when YBCO undergoes a large compressive strain. Ca intermixing into the YBCO layer is accompanied by various effects such as the creation of oxygen vacancies [103, 138], an enhancement the cation disorder [101] and chemical inhomogeneity [102]. As a result, the reduction of T_C correlates with an increase of Ca concentration in LCMO layer.

The unconventional mechanisms of the interrelation between superconductivity and magnetic ground states are out of scope of this study.

4.2.5 Summary of the section

We systematically studied YBCO(4 u.c.$\sim$ 47 Å)/LCMO(200Å) bilayers fabricated using PLD on STO (001) substrates with different Ca doping concentration x=0.3, 0.45, 0.55 and 0.8 in the LCMO layer. We observed that the superconductivity in the YBCO layers is correlated with the Ca concentration in the LCMO layers and is suppressed as the Ca doping level increases. This dependence cannot be explained in terms of traditional charge transfer of spin-polarized quasiparticles based on difference of the Fermi levels in adjacent layers. We found that this T_C suppression is correlated with the change of the in-plane lattice mismatch between YBCO and LCMO layers as well as Ca concentration. We discussed the structural heterogeneity as an origin of the T_C reduction in our bilayers. We did not rule out the orbital reconstruction caused by a change of the orbital occupancy in the LCMO layer with Ca doping concentration and hybridization of the orbitals in the YBCO layer. However, to confirm this scenario further experiments are required. Another mechanism originates from the defects induced by the lattice mismatch. The in-plane lattice mismatch between YBCO and LCMO layers cause different types of defects including oxygen vacancies (see Sec.4.1), cationic substitution (intermixing) and disorder, and suppresses superconductivity in thin YBCO layer.

4.3 Persistent photoconductivity in oxygen deficient YBCO/LCMO superlattices

Oxide heterostructures and superlattices combining materials with different collective electronic ordering phenomena, especially increased in popularity due to the possibility to explore the interactions between the long-range order of electrons and the modification of their spin and orbital states by artificial architectures [16, 74, 76, 139]. They offer an unique opportunity to externally control their electrical, magnetic, and optical properties based on the coupled charge, spin, orbital, and lattice interactions of the constituents by exposing them either to elastic, electrical, or magnetic fields or to subject them to a pulsed or continuous-wave photon flux. The physics behind is seen in the subtle balance of a rich set of coexisting electronic phases with comparable ground state energies. Novel architectures can be constructed, showing functions well beyond charge density manipulations determining the functionality of conventional semiconductor heterostructures. Interface engineering, currently a flourishing field, enables the tuning of the properties of such heterostructures and might pave the way to access new quantum phases. To explore these opportunities, a fundamental understanding of the modifications of the electronic structure at the interface is required. Photon exposure of complex oxides is one possibility to achieve this goal, it alters the charge carrier density, thus change the interplay between different phases. Especially, samples with oxygen vacancies can lead to new photo-generated effects based on photo-doping and may guide to novel device applications. Reciprocally, photo-doping can be used as an analytical tool to detect oxygen vacancies in such systems. Tailored changes of the electronic properties of complex oxides by intrinsic photo-induced doping have been observed in many perovskite-type materials, amongst them the superconducting cuprates [140, 141] and the colossal magneto-resistance manganites are the most prominent examples [142, 143]. Here, the overview of the photoconductivity in YBCO and LCMO will be presented first, followed by a research of photoconductivity in YBCO/LCMO heterostructures.

4.3.1 Background of the photoconductivity in YBCO and LCMO

Photoconductivity in YBCO

Photoconductivity in YBCO was first reported by G. Yu et al. [144]. Here, the author illuminated insulating single crystal YBCO with an oxygen content of 6.3 with a pulsed Nitrogen laser with duration of 600 picoseconds. The illuminated YBCO showed a large decrease of the re-

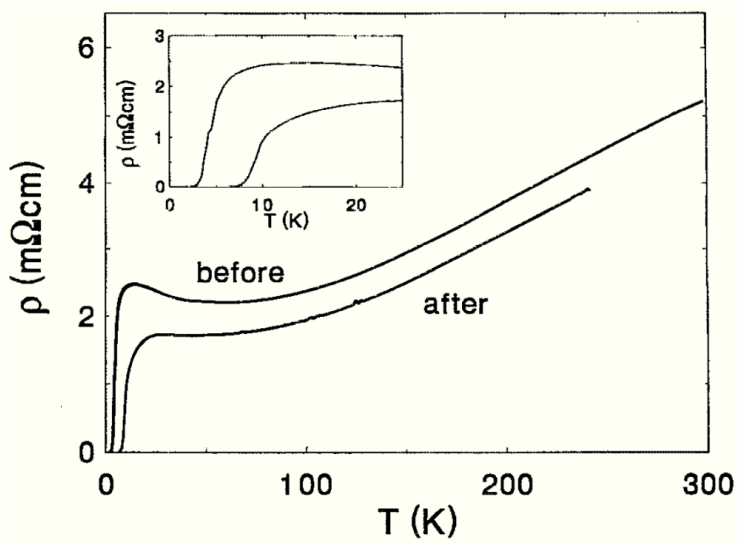

Figure 4.34: Typical PPC effect observed in 1000 Å YBCO thin film. The figure was taken from Ref. [141].The temperature dependences on the resistivity of the YBCO thin film before and after illumination are shown. The inset gives a magnification of the region of the superconducting transition.

sistance by more than 14 orders of magnitude at 50 K, and after the illumination the resistance recovered to the original value with a power law decay of $t^{-0.75}$. Shortly after the discovery of this transient photoconductivity (TPC), an impact of the persistent photoconductivity (PPC) was announced. Kirilyuk et al. reported that a YBCO thin film with oxygen content of around 6.45, which is insulating but close to the boundary to the superconducting state, showed large PPC effect when the illumination was carried out at 2 K [140, 145]. Fig.4.34 shows a typical PPC effect observed in YBCO thin film. Not only the conductivity, but also T_C increases persistently. Following this finding, large amount of researches were performed on this issue [146–149]. Here the brief summary of them is as follows.

- The photoconductivity is persistent as far as the sample is at a low temperature, and the PPC effect starts relaxing when the temperature increases to higher than ~ 270 K.
- The magnitude of the photoconductivity is enhanced as the oxygen content decreases [141, 150, 151]. In highly doped YBCO sample with an oxygen content of 7, the photoconductivity effect is absent.

- The effect is fostered as the amount of photon dose increases. Higher photon dose gives rise to a stronger effect [152] and the time to get saturation is reduced. The spectral dependence on the efficiency of the PPC effect was also investigated, and the excitation efficiency is strongly enhanced for a photon energy of 4.1 eV [153].

- Due to photo-doping, an increase of hole concentration and carrier mobility was observed [154]. A contraction of c lattice parameter also occurs [155]. It was observed that the contraction of the c parameter is accompanied by the change of the resistivity, and their behaviors are consistent.

- The CuO chain layer plays an important role in the PPC effect [156].

Two models are mainly utilized to explain the PPC in oxygen deficient YBCO. One is so-called oxygen vacancy trapping [150], and the other is photo-induced oxygen ordering [141, 151]. In oxygen vacancy trapping model, photo-induced electrons are trapped in oxygen vacancies in the CuO chains. The trapped electrons cause a lattice distortion and the distortion creates an energy barrier to disturb the recombination of them. The remaining holes are transferred to the neighboring CuO_2 plane and enhance the conductivity. In photo-induced oxygen ordering model, photons assist the diffusion of oxygen by inducing local electric fields in the chains, resulting in an increase of CuO chain length and enhancement of the conductivity and T_C. There is a report suggesting that the photoconductivity in YBCO cannot be demonstrated by only one model, and both mechanisms are convoluted [157–160]. Despite intensive researches, the microscopic mechanism is not clear yet.

Photoconductivity in LCMO

LCMO is also known as a material which shows a noteworthy photoconductivity. The photoconductivity experiment on LCMO is originally motivated by the following reasons. (1) LCMO is known by CMR effect and its functional properties are quite sensitive and unpredictable to a doping because of a nature of strongly correlated system. (2) LCMO has a perovskite structure same like YBCO. Taking account of the fact that YBCO shows the extrinsic PPC effect, it is worth to do photo-doping on LCMO. As a matter of fact, a similar compound $Pr_{0.7}Ca_{0.3}MnO_3$ was shown to have an anomalous PPC effect [161]. $Pr_{0.7}Ca_{0.3}MnO_3$ is an antiferromagnetic charge-ordered insulator at a low temperature. An illumination of X-ray at 4K induced a persistent transition from the original phase to a ferromagnetic metal as shown in Fig.4.35. This transition

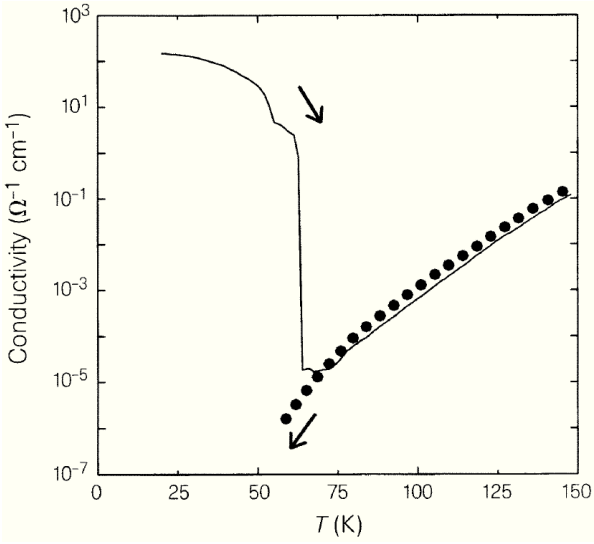

Figure 4.35: (From Ref. [161]) Conductivity measured on cooling before X-ray illumination (dotted curve) and on heating after illumination with X-rays for a moderate amount of time (solid curve).

is attributed to a relaxation of the lattice due to the X-ray. This finding highlighted the photoconductivity effect on manganites films. Then the PPC on $La_{0.7}Ca_{0.25}Ba_{0.05}MO_3$ and $La_{0.7}Ca_{0.2}Ba_{0.1}MnO_3$ thin films on STO substrates were reported [162]. Shortly after this report, it was demonstrated that oxygen vacancies play a role in the photoconductivity effect of manganite [142,143,163]. Very briefly, the PPC effect is present in oxygenated $La_{0.7}Sr_{0.3}MO_3$ (LSMO) and LCMO. When LSMO and LCMO acquire oxygen deficiency, the transport properties change from a metal to an insulator. These oxygen deficient manganites films show a TPC effect accompanied by photo-induced insulator to metal transition. The mechanism is supposed to be similar to the cuprate, that is, the photo-electrons are trapped at the defects, most likely oxygen vacancies, and the capturing energy becomes an energy barrier against recombination, resulting in the PPC effect. The TPC might be related to a weak localization of electronic wave functions in band tails due to the disorder generated by deoxygenation [143]. In contrast, photo-induced increase of resistance at $T < T_{\rm Curie}$ was also reported [164,165]. Here the increase of resistance was attributed to the effect that double exchange interaction which is responsible for the metallic transport was disturbed by the illumination. Except this, a reduction of resistance at $T > T_{\rm Curie}$ due to photo-ionized Jahn-Teller small polaron [166], demagnetization in (NdSm)SrMnO [167], and photo-induced COI/AFM

to FM metal transition [168, 169] are reported. The existence of several kinds of photo-induced effects is a reflection of complicated electronic mechanisms which determine the physical properties of the manganites. Situation is not simple and there is no general understanding of the microscopic mechanisms of photo-induced phenomena in manganites. It is important to note that the contribution of the STO substrate can play a role [170].

Photoconductivity in YBCO/LCMO heterostructure

When YBCO and LCMO thin films are combined, the heterostructure showed a completely different photoconductivity from a single YBCO or LCMO thin film [171]. Here, an oxygen deficient YBCO/LCMO bilayer showed an large transient photoconductivity with an enhanced increase of T_C (Fig.4.36). The transient enhancement of T_C due to illumination is 23 K which is much larger than the persistent enhancement of T_C found in single YBCO with the same oxygen content $d = 0.3$, where the increase of T_C due to illumination is 3.6 K. Fig.4.37 shows the time dependence of the resistance of the YBCO/LCMO bilayer sample. In Fig.4.37, the rapid decrease of the resistance occurs as soon as the light is turned on. Then, when the light is turned off, the resistance goes back to the original value with a time scale of ~ 100 seconds. The photoconductivity is not persistent, but transient. The relaxation times for the

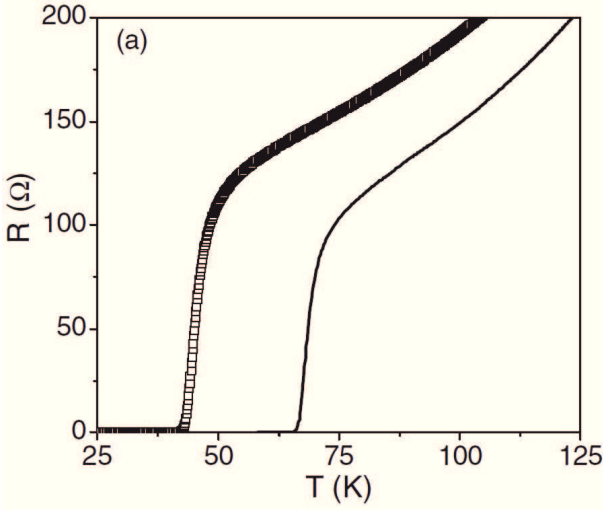

Figure 4.36: (From Ref. [171]) Resistance curves vs temperature for a bilayer with 12 u.c. YBCO($d = 0.3$)/ 40 u.c. LCMO, in the dark (open symbols) with $T_C = 43$ K, and under illumination (solid line).

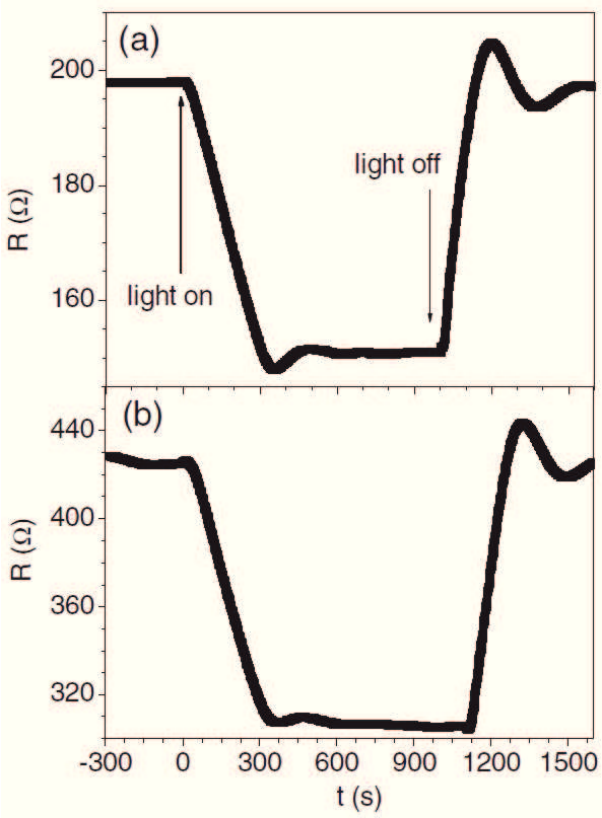

Figure 4.37: (From Ref. [171]) Time dependence of the resistance when the light is switched on (t=0 s) and off for (a) a 12 u.c. YBCO($d = 0.3$)/ 40 u.c. LCMO bilayer, and (b) a 60 u.c. LCMO film, both at T=100 K.

bilayer and the single LCMO film are similar, therefore the relaxation of the photoconductivity is supposed to be related to the relaxation mechanism in LCMO. The origin of the waving, which is observed after the saturation and relaxation, is unclear. The authors discussed their findings in terms of light-induced charge transfer through the interface and enhanced recombination of photo-generated holes in LCMO. This indicates, the photo-induced effect can be a tool to extract the charge transfer at the interface of YBCO and LCMO. From the other aspect, the photoconductivity effect is significantly influenced by the oxygen deficiency. The photoconductivity experiment should support our understanding of the role of oxygen deficiency in YBCO/LCMO heterostructures. Due to these interests, the photo-induced effects are investigated systematically in oxygen reduced PLD grown $YBa_2Cu_3O_{7-d}/La_{0.7}Ca_{0.3}MnO_{3-\delta}$ superlattices (SLs).

4.3.2 Sample preparation

Single YBCO thin films and superlattices consisting of YBCO and LCMO were deposited by conventional pulsed laser deposition techniques. For the PLD process, a KrF excimer laser with a wave length of 248 nm was used adjusting the photon fluence to 1.6 J/cm^2, and the pulse frequencies to 2 Hz and 3 Hz for YBCO and LCMO, respectively. All samples were deposited on 5×5mm^2 single crystal (001)-oriented $SrTiO_3$ substrates. The thickness of single layer YBCO samples is fixed to 100 nm, and the LCMO/YBCO SLs are composed of 20 nm of LCMO and 20 nm of YBCO on top with 8 repetitions of them. The superlattice structure is chosen rather than the bilayer structure ot highlight the contribution of the interface. For the deposition, the substrates were heated to 720 °C in an oxygen partial pressure of 0.2 mbar. All the single YBCO and SLs are grown at this condition. After the deposition, the films are cooled down to 520 °C at the ramping rate of 5 °C/min, and subsequently the oxygen partial pressure was increased to 1 bar. The samples were annealed for 1hour to obtain complete oxygenation. To systematically adjust different levels of oxygenation, the samples were then cooled down to 400 °C at a rate of 10 °C/min, and then exposed to a reduced oxygen atmosphere with the partial pressure ranging from 1 bar to 10^{-3} mbar. The annealing times were 2.5 and 16 hours for single YBCO and SLs, respectively. After annealing, the infrared laser heater was turned off and the samples were cooled down to room temperature.

4.3.3 Structural analysis

X-ray diffraction was performed using a Bruker AXS-D8 X-ray diffractometer with CuK_α radiation (λ=0.1541 nm). The XRD result of single

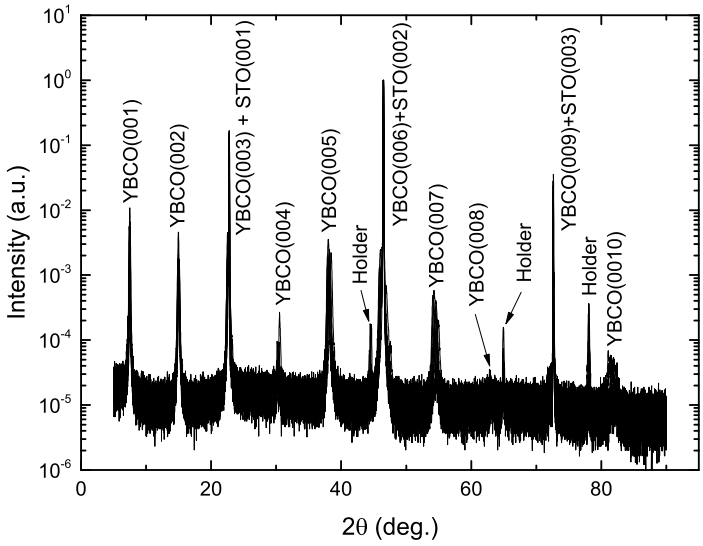

Figure 4.38: XRD $\theta - 2\theta$ scan of the 1000 Å YBCO thin films.

YBCO thin films is shown in Fig.4.38. YBCO (00l) diffraction peaks as well as the peaks from the STO substrate are present. The YBCO (003), (006) and (009) diffraction peaks overlap with those of STO diffraction peaks. There are some additional diffraction peaks from the sample holder. The magnification around YBCO (005) diffraction peak is shown in Fig.4.39. The peak position shifts from higher to lower angles according to the change of the pressure of post-annealing from 1 bar to 10^{-3} mbar. The shift of the diffraction peak position to the lower angles is interpreted as a prolongation of the out-of-plane lattice parameter due to the oxygen deficiency. According to Bragg equation, the longer spacing leads the smaller diffraction angle.

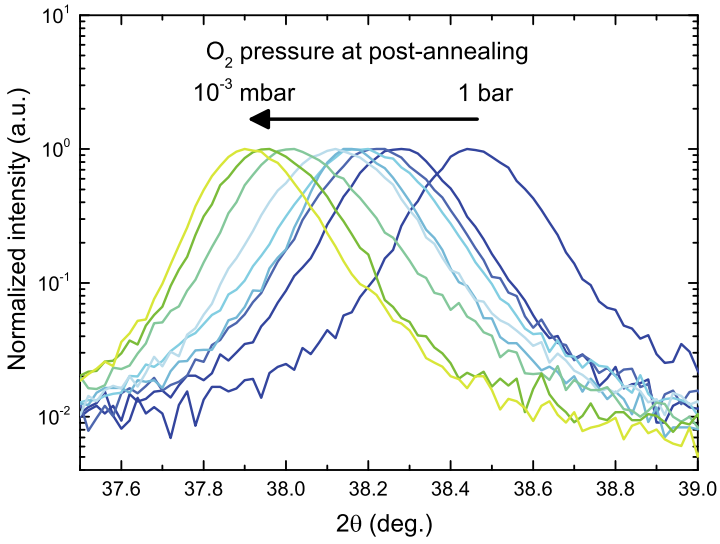

Figure 4.39: Magnification around the YBCO (005) diffraction peaks in the 1000 Å YBCO thin films.

Then, the XRD result of the SL samples is shown in Fig.4.40. First of all, YBCO (00l) diffraction peaks are clearly visible. In addition, LCMO (00l) diffraction peaks are observed, slightly overlapping with the STO diffraction peaks because of the similar out-of-plane lattice parameter. The magnification around YBCO (005) is given in Fig.4.41. The shift of YBCO (005) diffraction peak due to the change of oxygen deficiency is present.

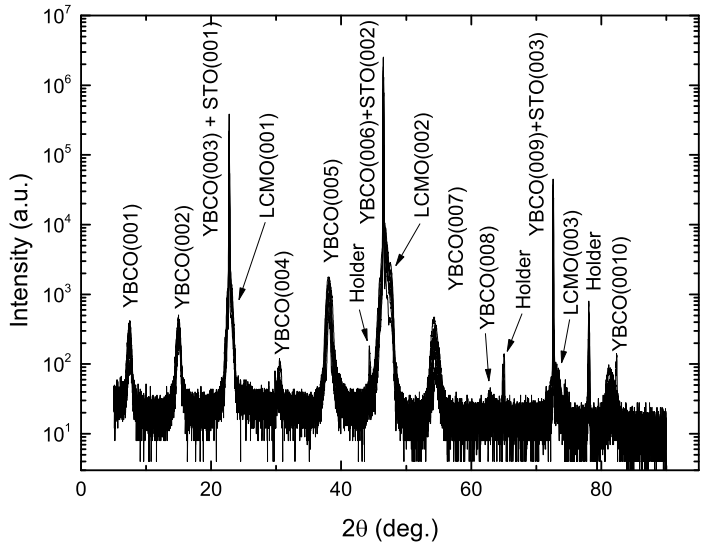

Figure 4.40: XRD $\theta - 2\theta$ scan of the SL samples.

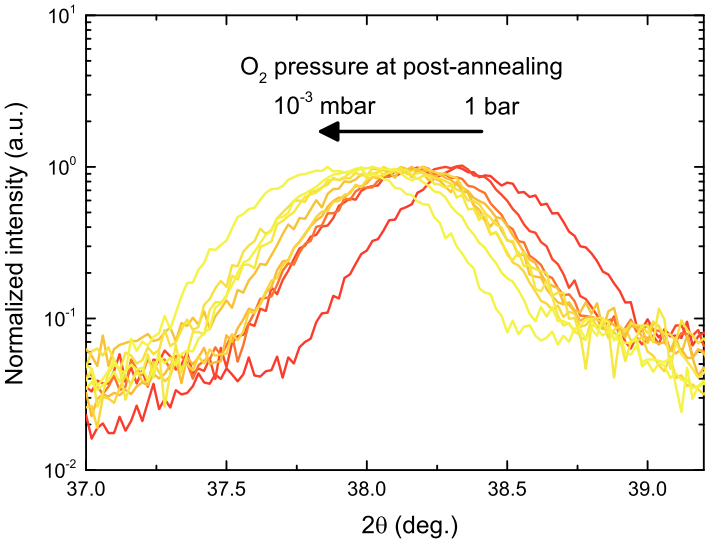

Figure 4.41: Magnification around the YBCO (005) diffraction peaks in the SL samples.

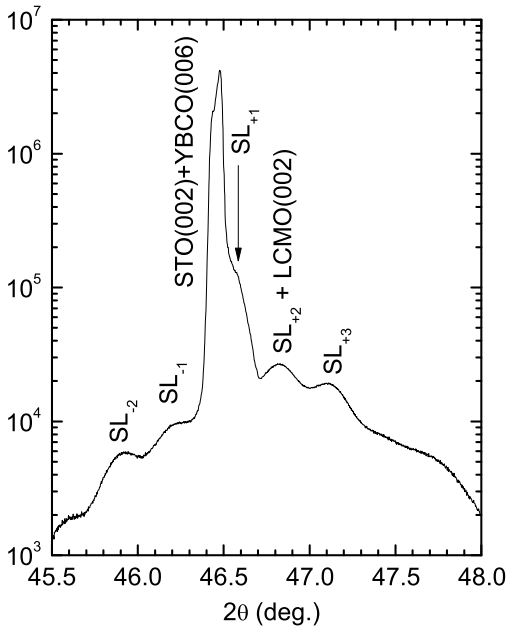

Figure 4.42: Magnification around the STO (002) diffraction peak in a representative SL sample.

Fig.4.42 shows the magnification around the STO (002) diffraction peak of one of the superlattice samples. Except for a strong STO (002) diffraction, an oscillation of the diffraction intensity exists. This oscillation is so-called superlattice peaks, which originate from a multi-layered structure of the sample. The existence of those superlattice peaks confirms the high quality of the SL structure with the chemically abrupt interfaces between different layers. The X-ray pole figure around YBCO (117) diffraction peak on the SL sample is shown in Fig.4.43. The sharp (117), (-117), (1-17) and (-1-17) diffraction peaks are present. These sharp peaks indicate the mosaicity of the YBCO layers in the SL sample is small and a nice epitaxial growth.

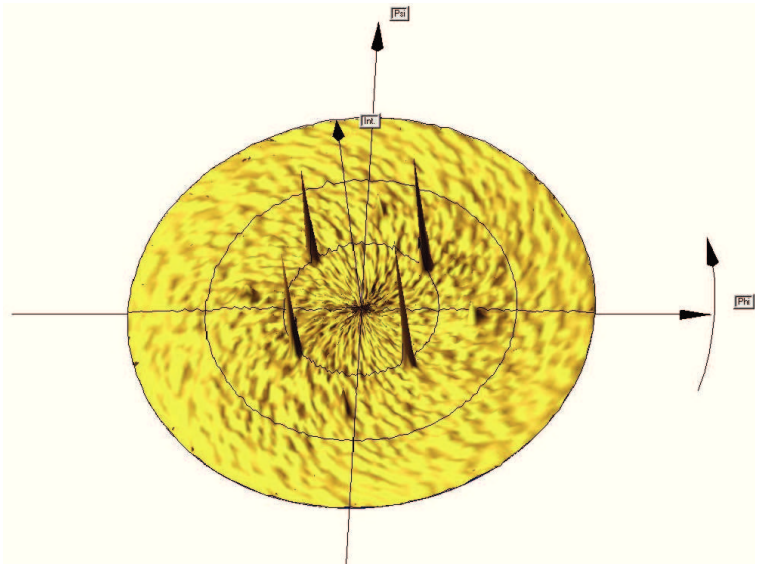

Figure 4.43: X-ray pole figure around YBCO (117) on the SL sample.

4.3.4 Persistent photoconductivity in oxygen deficient YBCO/LCMO superlattices

The result of a standard transport measurement on single YBCO layers without illumination is shown in Fig.4.44. In single YBCO, T_C decreases with decrease of the oxygen pressure during post-annealing. The YBCO thin films post-annealed at lower than 5×10^{-3} mbar were not superconducting and insulating.

The result of transport measurements on the SL samples without illumination is shown in Fig.4.45. In the SL samples, a similar decrease of T_C was observed. T_C decreases with the increase of oxygen deficiency in YBCO. Here, the deoxygenated SL samples show a metallic transport property accompanied by a resistance peak at $\sim$ 200 K. This peak in the resistance corresponds to an insulator to metal transition in LCMO, and the peak temperature is related to T_{Curie}. It is interesting to note that, in the well-deoxygenated SL samples, the YBCO layers are not superconducting because of the induced oxygen deficiency. On the other hand, the LCMO layers in these SL samples are still metallic with the peak temperature of $\sim$ 200 K.

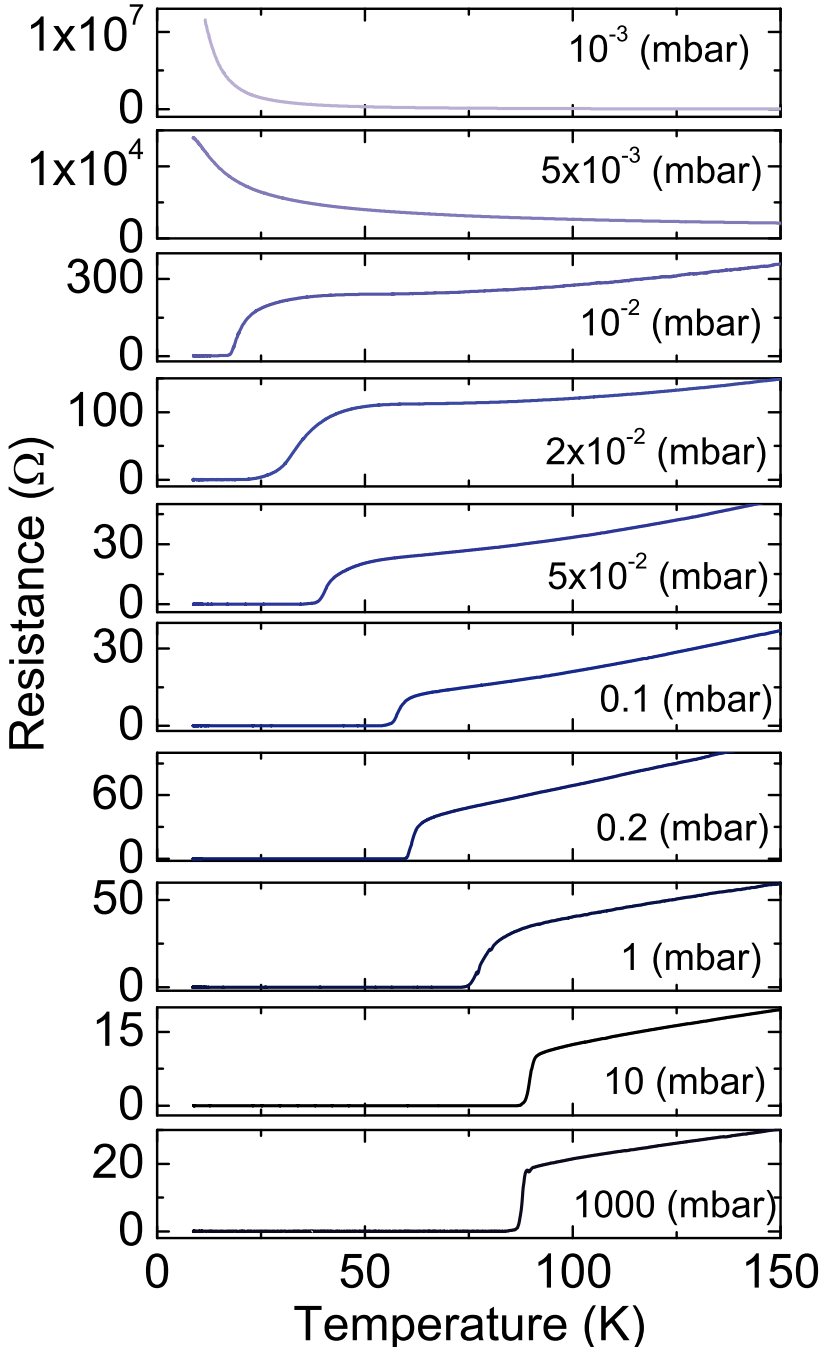

Figure 4.44: Temperature dependence on the resistance of 1000 Å YBCO thin films with different oxygen contents. The oxygen pressures used in post-annealing are shown.

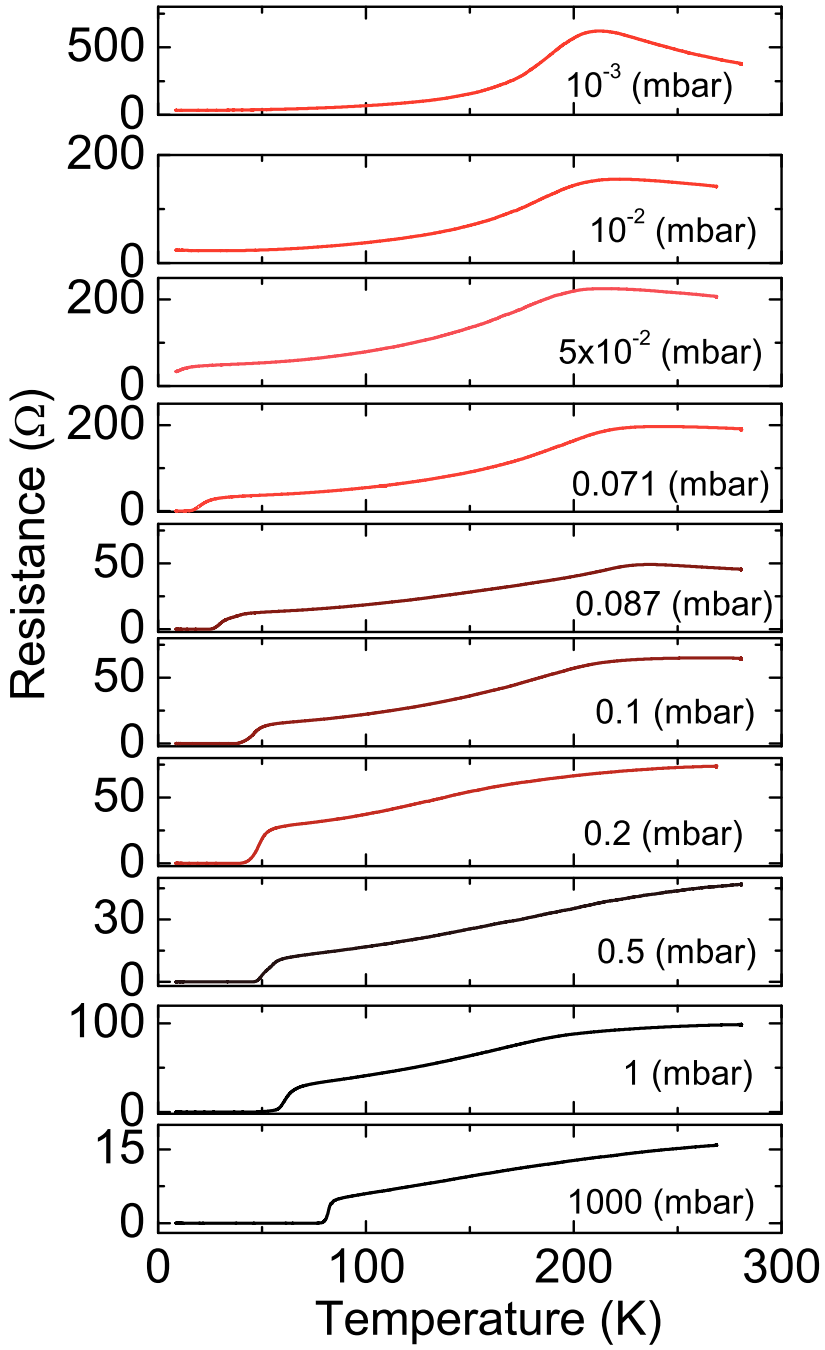

Figure 4.45: Temperature dependence on the resistance of the SL samples with different oxygen contents. The oxygen pressures used in post-annealing are shown.

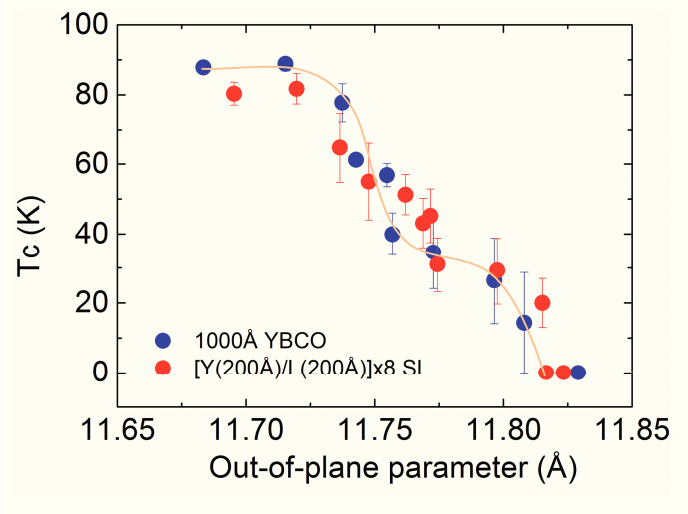

Figure 4.46: Relation between the out-of-plane parameter and T_C. The error bar corresponds to the onset and off of the superconducting transition. The solid line was added for the eye.

T_C of all samples are determined from the transport result. Thus a relation of T_C and the out-of-plane lattice parameters is summarized in Fig.4.46. Here, the out-of-plane parameter of YBCO in the single YBCO thin films as well as the superlattice samples were calculated by a use of Nelson-Riley function. T_C vs. the out-of-plane parameter curve in the single YBCO film shows two plateaus which are characteristic of YBCO [32]. The superlattice samples also shows a similar tendency which is not pronounced as single YBCO.

Next, the result of the photoconductivity measurement is going to be presented. The result of the illumination on a deoxygenated YBCO thin film with T_C of 36.0 K is given in Fig.4.47. Fig.4.47 shows the resistance of a representative singly YBCO thin film sample during the illumination as a function of time. The measurement was performed at 95 K. This temperature was chosen to measure the photoconductivity in the normal state of the YBCO thin films. When the illumination is turned on, the resistance starts decreasing in an asymptotic way. The illumination was lasted for 5 hours, then the ramp was turned off. With turning off the ramp, a small jump is observed. This jump is attributed to a heating effect due to the illumination. After turning off the illumination, the resistance is stable, therefore the photoconductivity effect is persistent.

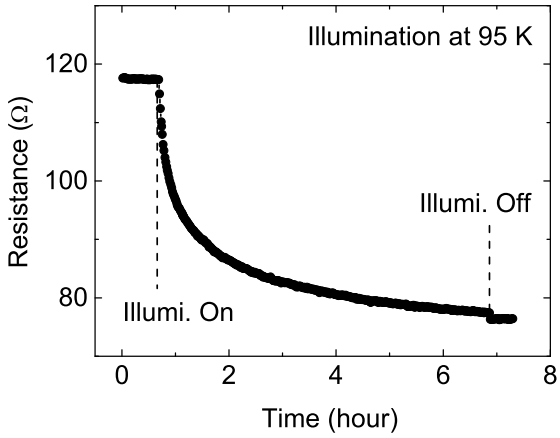

Figure 4.47: Time dependence of the resistance of a 1000 Å YBCO thin film during illumination measured at 95 K.

Fig.4.48 is the resistance vs. temperature before and after illumination. A temperature dependence of the resistance under the illumination is also added. Comparing the temperature dependences of the resistance in the dark and after the illumination, T_C was enhanced by the illumination persistently from 36.0 K to 40.5 K. The two temperature dependences of the resistance in the dark and under the illumination are overlapping, that is, the photoconductivity is saturated and there is no transient photoconductivity in single YBCO samples.

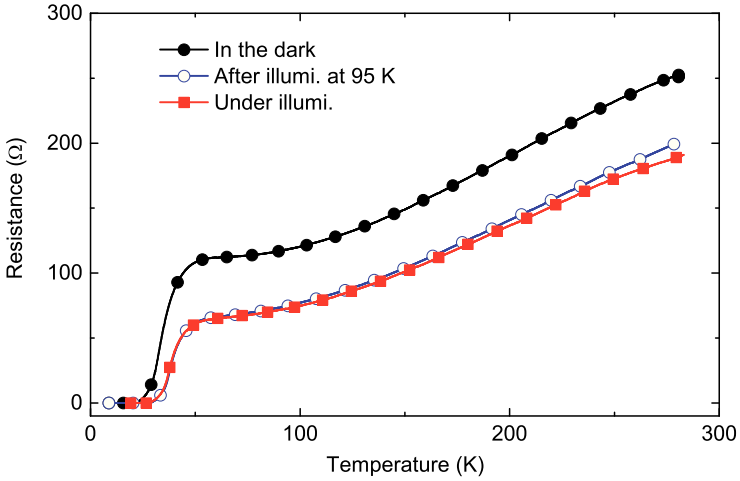

Figure 4.48: Resistance vs. temperature of a 1000 Å YBCO thin film before and after illumination. The other curve shows temperature dependence of the resistance under illumination.

The photoconductivity measurement was performed in the same way on the SL samples. Fig.4.49 shows the result on one of the deoxygenated SL samples, which has T_C of 22.1 K. The resistance decreases monotonically during illumination. The heating effect is obvious compared to the single YBCO because the magnitude of the photoconductivity is smaller than single YBCO and relatively heating effect is pronounced. After the illumination, the resistance was stable and the effect was persistent as in the case of single YBCO. Fig.4.50 shows the temperature dependences of the resistance before and after illumination, as well as under illumination measured in a heating process. T_C changes from 22.1 K in the dark to 28.4 K after the illumination. Similar to single YBCO, the resistance curves after and under illumination are overlapping at a lower temperature region, indicating an absence of a contribution of the transient photoconductivity. Above 200 K a transient contribution of ~ 4 % is observed, tentatively ascribed to the extended exposure to light during a heating process of the measurement, or a transient structural reconfiguration of the oxygen ion positions.

The photoconductivity measurement was performed on all the samples: single YBCO films and the SL samples with different oxygen content. A magnitude of the photo-induced effect was estimated from the reduction ratio of resistance due to illumination for 5 hours at 95 K. Here, the reduction ratio is defined by $\Delta R/R_0$, where R_0 is the initial resistance at 95 K and ΔR is the reduced value due to illumination for

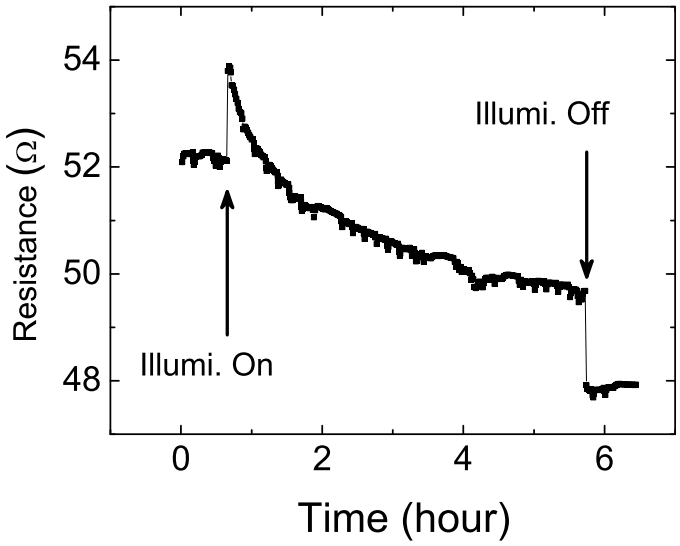

Figure 4.49: Time dependence of the resistance during illumination measured on a representative SL sample with T_C of 22.1 K. The illumination was done at 95 K.

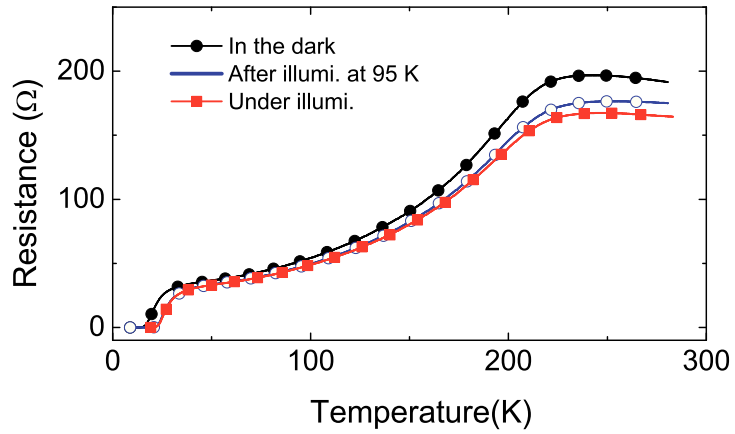

Figure 4.50: Temperature dependences of the resistance in a representative SL sample before and after illumination, as well as under illumination.

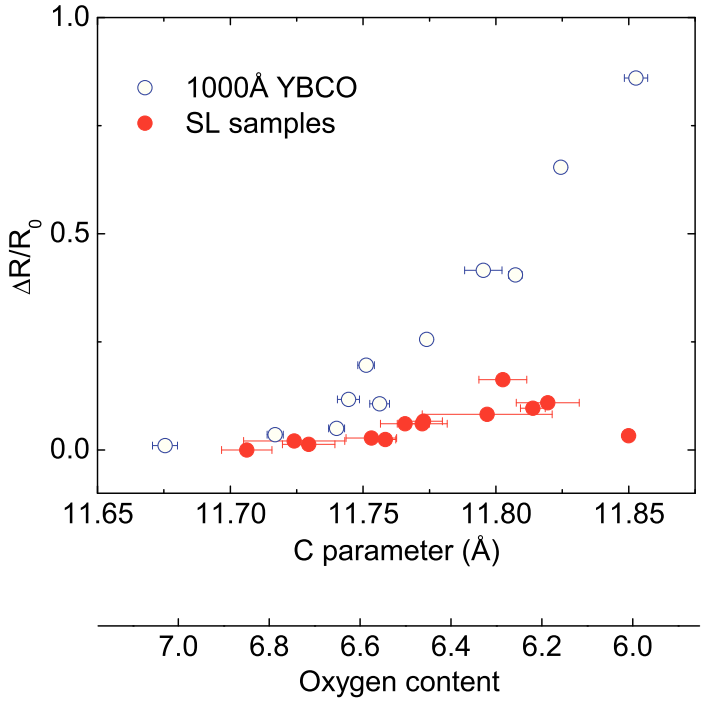

Figure 4.51: Reduction ratio $\Delta R/R_0$ vs. c parameter of the YBCO lattice of the 1000 Å YBCO (open circle) and the SL samples (closed circle). $\Delta R/R_0$, where R_0 is the initial resistance at 95 K and ΔR is the reduced value due to illumination for 5 hours. The additional x-axis of oxygen content was derived from c lattice parameter according to Ref. [47]. The error bar originates from the FWHM of the Bragg diffraction peak of YBCO.

5 hours. The reduction ratio of all the single YBCO and SL samples are summarized in Fig.4.51. The oxygen content in Fig.4.51 was derived from R. Liang *et al.* [47]. In single YBCO, the effect is enhanced as the oxygen deficiency becomes larger. With the largest oxygen deficiency, the reduction ratio reached nearly 90%. On the other hand, the ratio $\Delta R/R_0$ in the SL samples is moderate in all region. Especially with the oxygen content less than 6.2, the effect is suppressed. This is because the resistance of the oxygen deficient YBCO layers is predominantly higher than that of the LCMO layers, even if the resistance was reduced by the illumination. Thus, the contribution of the LCMO layers is dominant and the net photoconductivity disappeared.

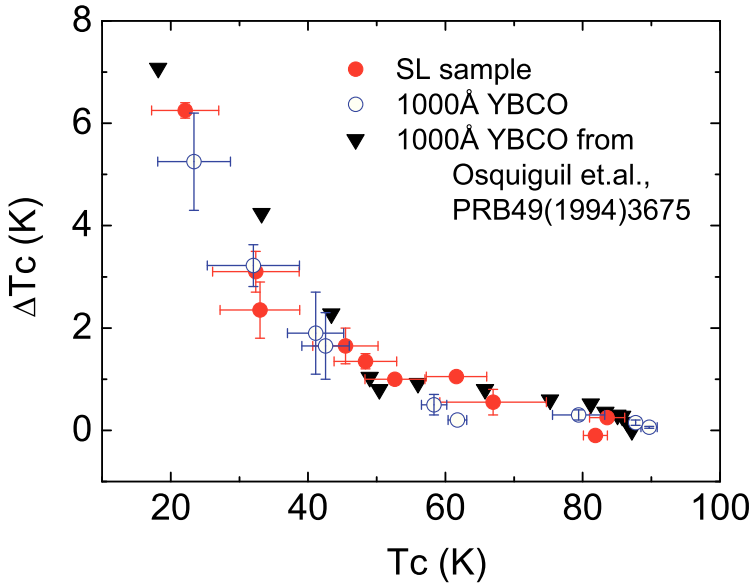

Figure 4.52: Photo-induced persistent enhancement of T_C, in a ΔT_C vs. T_C plot. The superlattice data (filled circles) are compared with 1000 Å YBCO films of this work (open circles) and literature values (filled triangles).

The persistent enhancement of T_C due to illumination, ΔT_C, is summarized as a function of T_C in Fig.4.52, together with a data for single layer YBCO films taken from a reference [150]. The error bars in Fig.4.52 are drawn from the onset of the superconducting transition to the zero resistance values in the corresponding $R(T)$ curves. Fig.4.52 clearly shows a PPC effect in the superlattices and its increase with decreasing T_C that coincides within the error bars with that of single layer YBCO films.

To discriminate the T_C reduction due to oxygen depletion and the subsequent increase by photon illumination from that due to superlattice formation we prepared a set of fully oxygenated SL films with different YBCO layer thicknesses, namely, [$LCMO_{20nm}/YBCO_{xnm}$]×10 ranging from x= 8, 4.5 and 3.5 nm, respectively. The resulting $R(T)$ data are represented in Fig.4.53 where the open symbols correspond to the data taken in the dark and the full symbols the ones after illumination measured in the dark (squares correspond to $x = 8$, dots to $x = 4.5$ and triangles to $x = 3.5$). The resistances in the dark show the large reduction of the midpoint of the transition to superconductivity as the

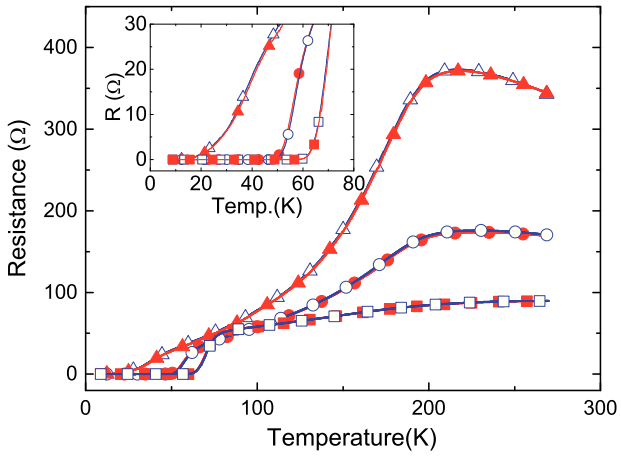

Figure 4.53: Temperature dependences on the resistance of SL samples $[LCMO_{20}/YBCO_x]_{10}$ with $x = 8, 4.5, 3.5$ nm, respectively. The open and filled symbols refer to the data before and after the illumination. The inset shows the magnification of the low temperature region.

YBCO layer becomes thinner, i.e. T_C = 70.2 K, 58 K and 35.3 K for x=8, 4.5 and 3.5, respectively. The data clearly show the absence of a photo-induced resistance change. The reduction of T_C for films with decreasing YBCO layer thickness is due to the electronic reconstruction at the YBCO/LCMO interface as discussed previously [74, 76, 139].

Comparing our results for oxygen depleted YBCO/LCMO superlattices grown at 720 °C by PLD and those of Peña *et al.* [171] for YBCO/LCMO bilayer sputtered at 900 °C, several differences occur. First, the bilayers grown by sputtering show no PPC effect, and single layer YBCO films do. Second, the T_C enhancement amounts up to 23 K in the sputtered bilayers, values about 6 times larger than those measured in sputtered single layer films of identical degree of oxygenation. In contrast to this, PLD grown superlattices show a persistent photoconductivity with ΔT_C up to $\sim$ 6 K depending on the degree of oxygenation; the T_C dependence of the PPC effect matches nicely with that of single layer YBCO films. Following the arguments given by Peña *et al.* [171], the transient photoconductivity and absent PPC observed in sputtered bilayer YBCO/LCMO structures are due to interfacial and/or electron transfer effects. The enhancement of T_C must arise from the YBCO layer where a surplus of holes appears during photon exposure. An increased relaxation compared to single layer YBCO films occurs, induced by the

LCMO layer. The similarity of the time scales of the relaxation time for the bilayer and single layer LCMO in Peña's experiments suggest, that charge transfer must be the driving force for the transient photoconductivity and is determined by the LCMO layer. On the other hand, this implies that the absence of a transient photoconductivity and the presence of a persistent photoconductivity in the PLD grown superlattices together with the quantitative agreement of ΔT_C for single layers and superlattices is caused by the lack of or drastically reduced charge transfer. The reason for the difference between sputtered and PLD grown films may rest in details of the microstructure of the films especially the structure of the interface, probably caused by the different energy of impinging atoms due to different deposition parameters and the deposition method. Careful TEM analysis of PLD grown YBCO-LCMO-YBCO trilayer systems by Zhang *et al.* [172] reveal that the layers are epitaxial, atomically smooth, and uniform across the entire specimen captured by the TEM experiments. The atomic stacking sequence at the interface of the LCMO layer grown on YBCO is different from that of the YBCO layer grown on LCMO. Both sequences, however, are different from the configuration previously identified in YBCO/LCMO superlattices prepared by sputtering using conditions identical to those used by Peña *et al.* [173].

4.3.5 Summary of the section

PLD grown oxygen depleted YBCO/LCMO superlattices show a persistent photoconductivity scaling nicely with those of single layer YBCO thin films. This is interpreted as a consequence of the lack of massive charge transfer from YBCO to LCMO and an enhanced recombination there. An electronic transparency at the interface is related to the quality of the interface [73]. Therefore, it is suggested our SL samples have chemically abrupt interfaces, resulting in the suppression of charge transfer between YBCO and LCMO layers. This conclusion is consistent with the result in Sec.4.2, where the YBCO/$La_{0.7}Ca_{0.3}MnO_3$ bilayer shows the better interface quality than YBCO/$La_{0.2}Ca_{0.8}MnO_3$ because of a smaller lattice mismatch. It was shown that the photoconductivity effects are sensitive to the microstructures of the films and the interfaces, and depend on the deposition conditions finely. Consequently, at the current stage of even advanced complex oxide deposition technologies it is difficult to generalize results without in depth knowledge of the structure of interfaces at the atomistic level and the role of process-induced defects in films and interfaces.

Chapter 5

Conclusion

In order to understand the precise mechanisms responsible for the intriguing properties of the YBCO/LCMO heterostructures, one has to discuss the following issues occurring simultaneously: (1) the electronic and magnetic properties at the interface, (2) the crystalline defects as represented by the oxygen vacancies which can have an impact on the property of complex oxides, and (3) the interface heterogeneity causing the lattice strain and the chemical intermixing in conjunction with strain-induced crystalline defects. Nevertheless, in the real system these issues are entangled with each other, and this fact made the oxide heterostructure as a subject hard to resolve. To address this problem, the YBCO and LCMO thin films as well as the heterostructures composed of these layers were investigated in respect of not only conventional SC/FM interplay, but also the crystalline defects and the interface heterogeneity.

In Sec.4.1, the interrelation of the oxygen deficiency and the lattice strain in LCMO thin films was investigated. For this purpose, the LCMO thin films were grown on three different substrates, STO, LSAT and LSAO, and four different oxygen pressures for growth, namely, 0.27, 0.2, 0.13 and 0.1 mbar were used. The XRD analysis confirmed the nice crystalline structure and the change of the oxygen content of the LCMO thin films. The shift of the (002) diffraction peak due to the change of the oxygen growth pressure was large in the film with tensile strain and was suppressed in the film with compressive strain, indicating oxygen vacancies are induced to accommodate tensile strain and compressive strain suppressed the formation of oxygen vacancies. Due to the systematic analysis, the entanglement of the strain and the oxygen deficiency in the LCMO thin films was clearly shown.

In Sec.4.2, the YBCO/LCMO bilayers were grown on STO substrates. The purpose was to investigate a role of the interface heterogeneity and induced crystalline defects at the YBCO/LCMO interfaces, in conjunction with the SC/FM interplay. In these bilayers, the Ca con-

centration of the LCMO layers was intentionally changed as Ca doping x=0.3, 0.45, 0.55 and 0.8, resulting in the change of the magnetism from the FM state (x=0.3) to the C-type AFM state (x=0.8) simultaneously accompanied by a contraction of the unit cell parameter of LCMO. The thickness of the YBCO layer was fixed to 4 u.c. to highlight the reduction of T_{C} due to the adjacent layer. This method was appropriate to estimate the magnitude of the FM/SC interplay and that of the heterogeneity of the interface.

As a consequence, the impact of the interface heterogeneity on the superconducting property of the YBCO layer was clearly shown. That is, the bilayer composed of the YBCO and ferromagnetic metal LCMO with x=0.3 showed the highest T_{C}, and the superconductivity was drastically suppressed in the bilayer of the YBCO and LCMO with x=0.8, where the LCMO layer is an antiferromagnetic insulator. The change of T_{C} was monotonic along the change of Ca doping x in the LCMO layer. This counterintuitive result indicates the interface heterogeneity has a strong influence on the superconductivity of adjacent YBCO layer. The mechanism of the T_{C} suppression was ascribed to the crystalline defects induced by the lattice mismatch and the cationic intermixing and related disorder driven by the difference in chemical potential.

In Sec.4.3, the single YBCO thin films and the YBCO/LCMO superlattices (SL) were studied via the photoconductivity measurement. This analysis allows us to approach the role of the oxygen deficiency in these samples and the role of the YBCO/LCMO interface. The SL samples and single YBCO thin films, where the oxygen content in YBCO was systematically altered by the controlled post-annealing process, were deposited by PLD. In the XRD analysis, both the single YBCO thin films and SL samples showed a systematic change of YBCO (005) diffraction peak position, indicating successful control of the oxygen deficiency in YBCO. In addition, the XRD on the SL samples showed the SL peaks corresponding to the repetition of YBCO/LCMO bilayers, which means, the chemically abrupt interfaces and the nice superlattice structures are guaranteed.

After the structural analyses by using the XRD measurement, the photoconductivity measurement was conducted on all the single YBCO and SL samples. The single YBCO thin films showed persistent photoconductivity (PPC) and the magnitude of the PPC was well consistent to the previous report. On the other hand, the SL samples showed the PPC effect, which is contradict to the previous publication [171]. In Ref. [171], the YBCO/LCMO bilayer showed a transient photoconductivity (TPC), and the effect was interpreted that the relaxation of photoconductivity was induced via charge transfer at the YBCO/LCMO interface. The

result suggests that in our SL samples the electronic transparency of the YBCO/LCMO interfaces was predominantly suppressed compared to the bilayer samples previously reported, due to the high quality of the interfaces with low electronic transparency. This consequence is consistent with the result in Sec.4.2, where the YBCO/$La_{0.7}Ca_{0.3}MnO_3$ bilayer shows higher T_C than YBCO/$La_{0.2}Ca_{0.8}MnO_3$ because of a smaller lattice mismatch, indicating the better quality can be obtained at the YBCO/$La_{0.7}Ca_{0.3}MnO_3$ interface. Consequently, it was shown that the interface quality, which is related to interface heterogeneity, influences the properties of the YBCO/LCMO heterostructures significantly.

In this thesis, the comprehensive study of the YBCO/LCMO heterostructures had been presented. As a result, it was shown that the quality of the hetero interfaces between the complex oxides has a strong impact on the physical properties and the crystalline structures. The interface heterogeneity induces creation of the crystalline defects: oxygen vacancies and cation intermixing, which strongly influence these properties. The accomplishment is important for fast developing field of the functional complex oxide heterostructure and interfaces.

Acknowledgement

This thesis is based on the tremendous favors of the people around me.

I would like to thank Professor Hidekazu Tanaka, who tolerated my inexperience and warmly watched out my activities for this long time. I am very much pleased to report this accomplishment finally to him.

I am sincerely grateful to Professor Hideomi Koinuma, my life saver. He gave me a rare opportunity to continue a scientific research, and this opportunity offers a breakthrough of my life. Without his courtesy and generosity, this thesis should have never existed.

I would like to express my cordial gratitude to Hanns-Ulrich Habermeier, the previous head of Technology group. He gave me a scientifically interesting task, which is the basement of my successive works, and introduced the exciting field of the oxide thin film to me. I am pleased that I could have his supervision and a lot of fruitful discussions as well as the meaningful results.

I would like to offer my special thanks to Gennady Logvenov, who is the new head of Technology group. He encouraged my projects aggressively at any time. His positive suggestions and deep insight have facilitated my motivation and understanding of the solid state physics.

I would like to appreciate Georg Christiani for his individualistic suggestions and ideas based on not only the scientific knowledge but also technical standpoint. And, special thanks to Birgit Lemke, Yvonne Link, Stephan Schmid, Peter Specht and Benjamin Stuhlhofer for the fundamental, scientific and technical supports as well as personal favors I received. I felt great about the welcoming atmosphere of Technology group produced by those people.

Many thanks go to the past and present scientific members in Technology group: Dimitry Kukuruznyak, Luqman Mustafa, Denitsa Shopova-Gospodinova, Petar Yordanov, Ingo Fritsche, Yuze Gao, Soltan Soltan, and special thanks to my long-term roommate Stefan Heinze. I have been very much motivated by their existences. They contribute much on the fulfilling period during my stay in Technology group.

I would like to close by saying thanks to my wife Akiko and my children Mitane and Maya for being by my side.

Publication list

Publications related to this thesis

- *"Long-range transfer of electron-phonon coupling in oxide superlattices"*

  N. Driza, S. Blanco-Canosa, M. Bakr, S. Soltan, M. Khalid, L. Mustafa, K. Kawashima, G. Logvenov, H.-U. Habermeier, G. Khaliullin, C. Ulrich, M. Le Tacon and B. Keimer

  Nature Materials **11**, 675 (2012)

- *"Persistent photoconductivity in oxygen deficient $YBa_2Cu_3O_{7-\delta}$/ $La_{2/3}Ca_{1/3}MnO_{3-x}$ superlattices grown by pulsed laser deposition"*

  K. Kawashima, S. Soltan, G. Logvenov and H.-U. Habermeier

  Applied Physics Letters **103**, 122603 (2013)

- *"Interrelation of epitaxial strain and oxygen deficiency in $La_{0.7}Ca_{0.3}MnO_{3-\delta}$"*

  K. Kawashima, G. Logvenov, G. Christiani and H.-U. Habermeier

  Journal of Magnetism and Magnetic Materials **378**, 539 (2015)

- *"Superconductivity in $YBa_2Cu_3O_{7-d}/La_{0.7}Ca_{0.3}MnO_{3-\delta}$ bilayers (x=0.3, 0.45, 0.55 and 0.8)"*

  K. Kawashima, G. Christiani, G. Logvenov and H.-U. Habermeier

  Journal of Superconductivity and Novel Magnetism (DOI) 10.1007/s10948-015-3014-9

Other publications

- *"High-temperature phase transition in RbH_2PO_4"*

  M. Komukae, K. Kawashima and K. Osaka

  Journal of the Physical Society of Japan **69**, 2076 (2000)

- *"Phase transitions in monoclinic RbH_2PO_4"*

  M. Komukae, K. Kawashima and T. Osaka

  Ferroelectrics **272**, 291 (2002)

- *"Infrared behavior of the attractive di-quark channel in the QCD model"*

  K. Kawashima

  International Journal of Modern Physics A **25**, 2023 (2010)

Bibliography

[1] M. Eschrig. *Physics Today*, 64(1):43–49, 2011.

[2] G. A. Prinz. *Science*, 282(5394):1660–1663, 1998.

[3] H. Y. Hwang, S. W. Cheong, P. G. Radaelli, M. Marezio, and B. Batlogg. *Physical Review Letters*, 75(5):914–917, 1995.

[4] H. Y. Hwang, Y. Iwasa, M. Kawasaki, B. Keimer, N. Nagaosa, and Y. Tokura. *Nature Materials*, 11(2):103–113, 2012.

[5] P. Zubko, S. Gariglio, M. Gabay, P. Ghosez, and J. M. Triscone. *Annual Review of Condensed Matter Physics, Vol 2*, 2:141–165, 2011.

[6] N. Reyren, S. Thiel, A. D. Caviglia, L. F. Kourkoutis, G. Hammerl, C. Richter, C. W. Schneider, T. Kopp, A. S. Ruetschi, D. Jaccard, M. Gabay, D. A. Muller, J. M. Triscone, and J. Mannhart. *Science*, 317(5842):1196–1199, 2007.

[7] A. Ohtomo and H. Y. Hwang. *Nature*, 427(6973):423–426, 2004.

[8] S. Thiel, G. Hammerl, A. Schmehl, C. W. Schneider, and J. Mannhart. *Science*, 313(5795):1942–1945, 2006.

[9] N. Nakagawa, H. Y. Hwang, and D. A. Muller. *Nature Materials*, 5(3):204–209, 2006.

[10] P. R. Willmott, S. A. Pauli, R. Herger, C. M. Schleputz, D. Martoccia, B. D. Patterson, B. Delley, R. Clarke, D. Kumah, C. Cionca, and Y. Yacoby. *Physical Review Letters*, 99(15):155502, 2007.

[11] W. Siemons, G. Koster, H. Yamamoto, W. A. Harrison, G. Lucovsky, T. H. Geballe, D. H. A. Blank, and M. R. Beasley. *Physical Review Letters*, 98(19):196802, 2007.

[12] A. Kalabukhov, R. Gunnarsson, J. Borjesson, E. Olsson, T. Claeson, and D. Winkler. *Physical Review B*, 75(12):121404, 2007.

[13] J.M.D. Coey, M. Viret, and S. von Molnar. *Advances in Physics*, 48(2):167–293, 1999.

[14] C. Bernhard, J. L. Tallon, C. Niedermayer, T. Blasius, A. Golnik, E. Brucher, R. K. Kremer, D. R. Noakes, C. E. Stronach, and E. J. Ansaldo. *Physical Review B*, 59(21):14099–14107, 1999.

[15] Z. Sefrioui, D. Arias, V. Pena, J. E. Villegas, M. Varela, P. Prieto, C. Leon, J. L. Martinez, and J. Santamaria. *Physical Review B*, 67(21):214511–1–214511–5, 2003.

[16] H. U. Habermeier, G. Cristiani, R. K. Kremer, O. Lebedev, and G. van Tendeloo. *Physica C*, 364:298–304, 2001.

[17] T. Holden, H. U. Habermeier, G. Cristiani, A. Golnik, A. Boris, A. Pimenov, J. Humlicek, O. I. Lebedev, G. Van Tendeloo, B. Keimer, and C. Bernhard. *Physical Review B*, 69(6):064505, 2004.

[18] N. Driza, S. Blanco-Canosa, M. Bakr, S. Soltan, M. Khalid, L. Mustafa, K. Kawashima, G. Christiani, H. U. Habermeier, G. Khaliullin, C. Ulrich, M. Le Tacon, and B. Keimer. *Nature Materials*, 11(8):675–681, 2012.

[19] J. G. Lin, S. L. Cheng, C. R. Chang, and D. Y. Xing. *Journal of Applied Physics*, 98(2):023910–1–023910–4, 2005.

[20] N. C. Yeh, R. P. Vasquez, C. C. Fu, A. V. Samoilov, Y. Li, and K. Vakili. *Physical Review B*, 60(14):10522–10526, 1999.

[21] S. Soltan, J. Albrecht, G. Cristani, and H. U. Habermeier. *Physica Status Solidi C: Magnetic and Superconducting Materials, Proceedings*, 1(7):1836–1839, 2004.

[22] S. Soltan, J. Albrecht, and H. U. Habermeier. *Solid State Communications*, 135(7):461–465, 2005.

[23] V. Pena, Z. Sefrioui, D. Arias, C. Leon, J. Santamaria, M. Varela, S. J. Pennycook, and J. L. Martinez. *Physical Review B*, 69(22):224502–1–224502–4, 2004.

[24] N. G. Pugach and A. I. Buzdin. *Applied Physics Letters*, 101(24):242602–1–242602–4, 2012.

[25] H. L. Tuller and S. R. Bishop. *Annual Review of Materials Research*, 41(9):369–398, 2011.

[26] J. R. Sun, C. F. Yeung, K. Zhao, L. Z. Zhou, C. H. Leung, H. K. Wong, and B. G. Shen. *Applied Physics Letters*, 76(9):1164–1166, 2000.

[27] Bing Li, Lei Yang, JinZeng Tian, XiaoPing Wang, Hong Zhu, and Tamio Endo. *Journal of Applied Physics*, 109(7):073922, 2011.

[28] I. Bozovic, G. Logvenov, I. Belca, B. Narimbetov, and I. Sveklo. *Physical Review Letters*, 89(10):107001–1–107001–4, 2002.

[29] K. Kawashima, S. Soltan, G. Logvenov, and H.-U. Habermeier. *Applied Physics Letters*, 103(12):122603, 2013.

[30] K. Kawashima, G. Logvenov, Christiani. G, and H.-U. Habermeier. *Journal of Magnetism and Magnetic Materials*, 378:539, 2015.

[31] K. Kawashima, Christiani. G, G. Logvenov, and H.-U. Habermeier. *Journal of Superconductivity and Novel Magnetism*, (DOI) 10.1007/s10948-015-3014-9, 2015.

[32] J. D. Jorgensen, B. W. Veal, A. P. Paulikas, L. J. Nowicki, G. W. Crabtree, H. Claus, and W. K. Kwok. *Physical Review B*, 41(4):1863–1877, 1990.

[33] R. J. Cava, B. Batlogg, R. B. Vandover, D. W. Murphy, S. Sunshine, T. Siegrist, J. P. Remeika, E. A. Rietman, S. Zahurak, and G. P. Espinosa. *Physical Review Letters*, 58(16):1676–1679, 1987.

[34] R. J. Cava, R. B. Vandover, B. Batlogg, and E. A. Rietman. *Physical Review Letters*, 58(4):408–410, 1987.

[35] M. Gurvitch and A. T. Fiory. *Physical Review Letters*, 59(12):1337–1340, 1987.

[36] T. Timusk and B. Statt. *Reports on Progress in Physics*, 62(1):61–122, 1999.

[37] J. L. Tallon and J. W. Loram. *Physica C*, 349(1-2):53–68, 2001.

[38] H. Alloul, T. Ohno, and P. Mendels. *Physical Review Letters*, 63(16):1700–1703, 1989.

[39] W. W. Warren, R. E. Walstedt, G. F. Brennert, R. J. Cava, R. Tycko, R. F. Bell, and G. Dabbagh. *Physical Review Letters*, 62(10):1193–1196, 1989.

[40] J. Rossatmignod, L. P. Regnault, C. Vettier, P. Bourges, P. Burlet, J. Bossy, J. Y. Henry, and G. Lapertot. *Physica C*, 185:86–92, 1991.

[41] J. M. Tranquada, P. M. Gehring, G. Shirane, S. Shamoto, and M. Sato. *Physical Review B*, 46(9):5561–5575, 1992.

[42] H. Takagi, B. Batlogg, H. L. Kao, J. Kwo, R. J. Cava, J. J. Krajewski, and W. F. Peck. *Physical Review Letters*, 69(20):2975–2978, 1992.

[43] B. Bucher, P. Steiner, J. Karpinski, E. Kaldis, and P. Wachter. *Physical Review Letters*, 70(13):2012–2015, 1993.

[44] H. Y. Hwang, B. Batlogg, H. Takagi, H. L. Kao, J. Kwo, R. J. Cava, J. J. Krajewski, and W. F. Peck. *Physical Review Letters*, 72(16):2636–2639, 1994.

[45] W. Y. Liang, J. W. Loram, K. A. Mirza, N. Athanassopoulou, and J. R. Cooper. *Physica C*, 263(1-4):277–281, 1996.

[46] J. M. Harris, Z. X. Shen, P. J. White, D. S. Marshall, M. C. Schabel, J. N. Eckstein, and I. Bozovic. *Physical Review B*, 54(22):15665–15668, 1996.

[47] R. X. Liang, D. A. Bonn, and W. N. Hardy. *Physical Review B*, 73(18):180505, 2006.

[48] Werner Martienssen. *Springer handbook of condensed matter and materials data*. Springer, Berlin; Heidelberg, 2005.

[49] S. K. Malik and S. S. Shah. *Physical and Material Properties of High Temeprature Superconductors*. Nova Publishers, 1994.

[50] X. X. Xi, J. Geerk, G. Linker, Q. Li, and O. Meyer. *Applied Physics Letters*, 54(23):2367–2369, 1989.

[51] J. Garcia-Barriocanal, A. M. Perez-Munoz, Z. Sefrioui, D. Arias, M. Varela, C. Leon, S. J. Pennycook, and J. Santamaria. *Physical Review B*, 87(24):245105, 2013.

[52] I. N. Chan, D. C. Vier, O. Nakamura, J. Hasen, J. Guimpel, S. Schultz, and I. K. Schuller. *Physics Letters A*, 175(3-4):241–245, 1993.

[53] S. Jin, T. H. Tiefel, M. Mccormack, R. A. Fastnacht, R. Ramesh, and L. H. Chen. *Science*, 264(5157):413–415, 1994.

[54] J. Blasco, J. Garcia, J. M. deTeresa, M. R. Ibarra, P. A. Algarabel, and C. Marquina. *Journal of Physics-Condensed Matter*, 8(40):7427–7442, 1996.

[55] S. W. Cheong and H. Y. Hwang. *Ferromagnetism vs. Charge/Orbital Ordering in Mixed-Valent Manganites*. Colossal Magnetoresistive oxides (Advances in Condensed Matter Science). Gordon and Breach Science Publishers.

[56] A. M. Haghiri-Gosnet and J. P. Renard. *Journal of Physics D-Applied Physics*, 36(8):R127–R150, 2003.

[57] C. Zener. *Physical Review*, 82(3):403–405, 1951.

[58] P. W. Anderson and H. Hasegawa. *Physical Review*, 100(2):675–681, 1955.

[59] M. Bibes, L. Balcells, S. Valencia, J. Fontcuberta, M. Wojcik, E. Jedryka, and S. Nadolski. *Physical Review Letters*, 87(6):067210, 2001.

[60] A. Moreo, M. Mayr, A. Feiguin, S. Yunoki, and E. Dagotto. *Physical Review Letters*, 84(24):5568–5571, 2000.

[61] V. Pena, Z. Sefrioui, D. Arias, C. Leon, J. Santamaria, M. Varela, S. J. Pennycook, M. Garcia-Hernandez, and J. L. Martinez. *Journal of Physics and Chemistry of Solids*, 67(1-3):472–475, 2006.

[62] R. M. Kusters, J. Singleton, D. A. Keen, R. McGreevy, and W. Hayes. *Physica B*, 155(1-3):362–365, 1989.

[63] N. Furukawa. *Journal of the Physical Society of Japan*, 64(8):2734–2737, 1995.

[64] M. Viret, L. Ranno, and J. M. D. Coey. *Physical Review B*, 55(13):8067–8070, 1997.

[65] G. Alvarez and E. Dagotto. *Journal of Magnetism and Magnetic Materials*, 272:15–20, 2004.

[66] M. Bibes, S. Valencia, L. Balcells, B. Martinez, J. Fontcuberta, M. Wojcik, S. Nadolski, and E. Jedryka. *Physical Review B*, 66(13):134416–1–134416–9, 2002.

[67] T. Y. Chien, L. F. Kourkoutis, J. Chakhalian, B. Gray, M. Kareev, N. P. Guisinger, D. A. Muller, and J. W. Freeland. *Nature Communications*, 4:1, 2013.

[68] V. Pena, C. Visani, J. Garcia-Barriocanal, D. Arias, Z. Sefrioui, C. Leon, J. Santamaria, and C. A. Almasan. *Physical Review B*, 73(10):104513, 2006.

[69] S. Soltan, J. Albrecht, and H. U. Habermeier. *Physical Review B*, 70(14):144517, 2004.

[70] F. Chen, B. Gorshunov, G. Cristiani, H. U. Habermeier, and M. Dressel. *Solid State Communications*, 131(5):295–299, 2004.

[71] V. Pena, Z. Sefrioui, D. Arias, C. Leon, J. Santamaria, J. L. Martinez, S. G. E. te Velthuis, and A. Hoffmann. *Physical Review Letters*, 94(5):057002–1–057002–4, 2005.

[72] A. Hoffmann, S. G. E. te Velthuis, Z. Sefrioui, J. Santamaria, M. R. Fitzsimmons, S. Park, and M. Varela. *Physical Review B*, 72(14):140407–1–140407–4, 2005.

[73] R. Werner, C. Raisch, A. Ruosi, B. A. Davidson, P. Nagel, M. Merz, S. Schuppler, M. Glaser, J. Fujii, T. Chasse, R. Kleiner, and D. Koelle. *Physical Review B*, 82(22):2245091–2245091–7, 2010.

[74] J. Chakhalian, J. W. Freeland, H. U. Habermeier, G. Cristiani, G. Khaliullin, M. van Veenendaal, and B. Keimer. *Science*, 318(5853):1114–1117, 2007.

[75] J. Stahn, J. Chakhalian, C. Niedermayer, J. Hoppler, T. Gutberlet, J. Voigt, F. Treubel, H. U. Habermeier, G. Cristiani, B. Keimer, and C. Bernhard. *Physical Review B*, 71(14):140509–1–140509–4, 2005.

[76] J. Chakhalian, J. W. Freeland, G. Srajer, J. Strempfer, G. Khaliullin, J. C. Cezar, T. Charlton, R. Dalgliesh, C. Bernhard, G. Cristiani, H. U. Habermeier, and B. Keimer. *Nature Physics*, 2(4):244–248, 2006.

[77] M. A. Uribe-Laverde, D. K. Satapathy, I. Marozau, V. K. Malik, S. Das, K. Sen, J. Stahn, A. Ruhm, J. H. Kim, T. Keller, A. Devishvili, B. P. Toperverg, and C. Bernhard. *Physical Review B*, 87(11):115105–1–115105–11, 2013.

[78] C. B. Cai, L. Peng, B. Holzapfel, X. M. Xie, Z. Y. Liu, Y. M. Lu, and C. Z. Chen. *Superconductor Science and Technology*, 23(3):034010–1–034010–5, 2010.

[79] S. Heinze, H. U. Habermeier, G. Cristiani, S. B. Canosa, M. Le Tacon, and B. Keimer. *Applied Physics Letters*, 101(13):131603, 2012.

[80] S. Fahler and H. U. Krebs. *Applied Surface Science*, 96-8:61–65, 1996.

[81] H. U. Habermeier. *Materials Today*, 10(10):34–43, 2007.

[82] R. Feenstra, T. B. Lindemer, J. D. Budai, and M. D. Galloway. *Journal of Applied Physics*, 69(9):6569–6585, 1991.

[83] R. Nagendran, N. Thirumurugan, N. Chinnasamy, M. P. Janawadkar, and C. S. Sundar. *Review of Scientific Instruments*, 82(1):015109, 2011.

[84] A. Vailionis, H. Boschker, W. Siemons, E. P. Houwman, D. H. A. Blank, G. Rijnders, and G. Koster. *Physical Review B*, 83(6):064101, 2011.

[85] S. J. May, J. W. Kim, J. M. Rondinelli, E. Karapetrova, N. A. Spaldin, A. Bhattacharya, and P. J. Ryan. *Physical Review B*, 82(1):014110, 2010.

[86] T. Y. Koo, S. H. Park, K. B. Lee, and Y. H. Jeong. *Applied Physics Letters*, 71(7):977–979, 1997.

[87] S. El Helali, K. Daoudi, A. Fouzri, M. Oumezzine, M. Oueslati, and T. Tsuchiya. *Applied Physics a-Materials Science and Processing*, 108(2):379–384, 2012.

[88] L. Ranno, A. Llobet, R. Tiron, and E. Favre-Nicolin. *Applied Surface Science*, 188(1-2):170–175, 2002.

[89] T. Petrisor, M. S. Gabor, A. Boulle, C. Bellouard, C. Tiusan, O. Pana, and T. Petrisor. *Journal of Applied Physics*, 109(12):123913, 2011.

[90] P. Orgiani, A. Guarino, C. Aruta, C. Adamo, A. Galdi, A. Yu Petrov, R. Savo, and L. Maritato. *Journal of Applied Physics*, 101(3):033904, 2007.

[91] M. Kanai, H. Tanaka, and T. Kawai. *Physical Review B*, 70(12):125109, 2004.

[92] Y. S. Du, B. Wang, T. Li, D. B. Yu, and H. Yan. *Journal of Magnetism and Magnetic Materials*, 297(2):88–92, 2006.

[93] U. Gebhardt, N. V. Kasper, A. Vigliante, P. Wochner, H. Dosch, F. S. Razavi, and H. U. Habermeier. *Physical Review Letters*, 98(9):096101, 2007.

[94] Arturas Vailionis, Hans Boschker, Evert Houwman, Gertjan Koster, Guus Rijnders, and Dave H. A. Blank. *Applied Physics Letters*, 95(15):152508, 2009.

[95] et al. A. Frano. *Advanced Materials*, 26:1, 2013.

[96] O. Moran, R. Hott, K. Grube, D. Fuchs, R. Schneider, E. Baca, W. Saldarriaga, and P. Prieto. *Journal of Applied Physics*, 95(11):6239–6244, 2004.

[97] M. Ziese, H. C. Semmelhack, K. H. Han, S. P. Sena, and H. J. Blythe. *Journal of Applied Physics*, 91(12):9930–9936, 2002.

[98] T. Kanki, H. Tanaka, and T. Kawai. *Physical Review B*, 64(22):224418, 2001.

[99] B. Vengalis, A. Maneikis, F. Anisimovas, R. Butkute, L. Dapkus, and A. Kindurys. *Journal of Magnetism and Magnetic Materials*, 211(1-3):35–40, 2000.

[100] R. B. Praus, B. Leibold, G. M. Gross, and H. U. Habermeier. *Applied Surface Science*, 138:40–43, 1999.

[101] J. P. Attfield. *Chemistry of Materials*, 10(11):3239–3248, 1998.

[102] H. Eisaki, N. Kaneko, D. L. Feng, A. Damascelli, P. K. Mang, K. M. Shen, Z. X. Shen, and M. Greven. *Physical Review B*, 69(6):064512–1–064512–8, 2004.

[103] A. Manthiram and J. B. Goodenough. *Physica C*, 159(6):760–768, 1989.

[104] R. Jones, P. P. Edwards, M. R. Harrison, T. Thanyasiri, and E. Sinn. *Journal of the American Chemical Society*, 110(20):6716–6720, 1988.

[105] P. K. Siwach, H. K. Singh, and O. N. Srivastava. *Journal of Physics-Condensed Matter*, 20(27):273201–1–273201–43, 2008.

[106] J. B. Goodenough. *Physical Review*, 100(2):564–573, 1955.

[107] J. H. Park, C. T. Chen, S. W. Cheong, W. Bao, G. Meigs, V. Chakarian, and Y. U. Idzerda. *Physical Review Letters*, 76(22):4215–4218, 1996.

[108] S. Yunoki, A. Moreo, E. Dagotto, S. Okamoto, S. S. Kancharla, and A. Fujimori. *Physical Review B*, 76(6):064532–1–064532–11, 2007.

[109] T. Ohnishi, K. Shibuya, M. Lippmaa, D. Kobayashi, H. Kumigashira, M. Oshima, and H. Koinuma. *Applied Physics Letters*, 85(2):272–274, 2004.

[110] R. D. Shannon. *Acta Crystallographica Section A*, 32(SEP1):751–767, 1976.

[111] W. S. Khan and S. K. Hasanain. *Physica Scripta*, 81(6):065702–1–065702–7, 2010.

[112] I. G. Deac and I. Balasz. *Materials Chemistry and Physics*, 136(2-3):850–857, 2012.

[113] P. Schiffer, A. P. Ramirez, W. Bao, and S. W. Cheong. *Physical Review Letters*, 75(18):3336–3339, 1995.

[114] C. Aruta, G. Ghiringhelli, V. Bisogni, L. Braicovich, N. B. Brookes, A. Tebano, and G. Balestrino. *Physical Review B*, 80(1):014431–1–014431–8, 2009.

[115] Z. Fang, I. V. Solovyev, and K. Terakura. *Physical Review Letters*, 84(14), 2000.

[116] M. A. L. de la Torre, V. Pena, Z. Sefrioui, D. Arias, C. Leon, J. Santamaria, and J. L. Martinez. *Physical Review B*, 73(5):052503, 2006.

[117] C. Z. Chen, C. B. Cai, L. Peng, Z. Y. Liu, Y. M. Lu, H. W. Wang, and X. M. Xie. *Epl*, 89(3):37005, 2010.

[118] N. Didier, C. Dubourdieu, A. Rosova, B. Chenevier, V. Galindo, and O. Thomas. *Journal of Alloys and Compounds*, 251(1-2):322–327, 1997.

[119] J. B. A. Elemans, B. Vanlaar, Vanderve.Kr, and B. O. Loopstra. *Journal of Solid State Chemistry*, 3(2):238–242, 1971.

[120] A. I. Shames, E. Rozenberg, G. Gorodetsky, M. I. Tsindlekht, I. Felner, D. Mogilyansky, A. Pestun, and Y. M. Mukovskii. *Journal of Applied Physics*, 101(10):103921–1–103921–6, 2007.

[121] S. J. Hibble, S. P. Cooper, A. C. Hannon, I. D. Fawcett, and M. Greenblatt. *Journal of Physics-Condensed Matter*, 11(47):9221–9238, 1999.

[122] J. C. Debnath, R. Zeng, J. H. Kim, and S. X. Dou. *Journal of Applied Physics*, 107(9):09A916–1–09A916–3, 2010.

[123] M. Mori, N. M. Sammes, E. Suda, and Y. Takeda. *Solid State Ionics*, 164(1-2):1–15, 2003.

[124] P. G. Radaelli, D. E. Cox, M. Marezio, and S. W. Cheong. *Physical Review B*, 55(5):3015–3023, 1997.

[125] H. Wakai, F. Munakata, and E. Iguchi. *Materials Science and Engineering B-Solid State Materials for Advanced Technology*, 103(1):26–31, 2003.

[126] E. Rozenberg, M. Auslender, A. I. Shames, D. Mogilyansky, I. Felner, E. Sominskii, A. Gedanken, and Y. M. Mukovskii. *Physical Review B*, 78(5):052405–1–052405–4, 2008.

[127] T. Sudyoadsuk, R. Suryanarayanan, P. Winotai, and L. E. Wenger. *Journal of Magnetism and Magnetic Materials*, 278(1-2):96–106, 2004.

[128] V. Markovich, J. Wieckowski, M. Gutowska, A. Szewczyk, A. Wisniewski, C. Martin, and G. Gorodetsky. *Journal of Applied Physics*, 107(6):063907–1–063907–5, 2010.

[129] H. Taguchi, M. Sonoda, M. Nagao, and H. Kido. *Journal of Solid State Chemistry*, 126(2):235–241, 1996.

[130] W. Paszkowicz, J. Pietosa, S. M. Woodley, P. A. Dluzewski, M. Kozlowski, and C. Martin. *Powder Diffraction*, 25(1):46–59, 2010.

[131] H. Yamada, M. Kawasaki, T. Lottermoser, T. Arima, and Y. Tokura. *Applied Physics Letters*, 89(5):052506–1–052506–3, 2006.

[132] B. R. K. Nanda and S. Satpathy. *Physical Review B*, 78(5):054427–1–054427–12, 2008.

[133] I. C. Infante, F. Sanchez, J. Fontcuberta, M. Wojcik, E. Jedryka, S. Estrade, F. Peiro, J. Arbiol, V. Laukhin, and J. P. Espinos. *Physical Review B*, 76(22):224415–1–224415–12, 2007.

[134] X. J. Chen, H. U. Habermeier, H. Zhang, G. Gu, M. Varela, J. Santamaria, and C. C. Almasan. *Physical Review B*, 72(10):104403–1–104403–7, 2005.

[135] C. Adamo, X. Ke, H. Q. Wang, H. L. Xin, T. Heeg, M. E. Hawley, W. Zander, J. Schubert, P. Schiffer, D. A. Muller, L. Maritato, and D. G. Schlom. *Applied Physics Letters*, 95(11):112504–1–112504–3, 2009.

[136] H. U. Habermeier, P. X. Zhang, T. Haage, and J. Q. Li. *Physica C*, 282:661–662, 1997.

[137] V. K. Malik, I. Marozau, S. Das, B. Doggett, D. K. Satapathy, M. A. Uribe-Laverde, N. Biskup, M. Varela, C. W. Schneider,

C. Marcelot, J. Stahn, and C. Bernhard. *Physical Review B*, 85(5):054514–1–054514–13, 2012.

[138] T. Hikita and M. Ogasawara. *Japanese Journal of Applied Physics Part 1-Regular Papers Short Notes and Review Papers*, 32(11A):4950–4955, 1993.

[139] Z. Sefrioui, M. Varela, V. Pena, D. Arias, C. Leon, J. Santamaria, J. E. Villegas, J. L. Martinez, W. Saldarriaga, and P. Prieto. *Applied Physics Letters*, 81(24):4568–4570, 2002.

[140] V. I. Kudinov, A. I. Kirilyuk, N. M. Kreines, R. Laiho, and E. Lahderanta. *Physics Letters A*, 151(6-7):358–364, 1990.

[141] G. Nieva, E. Osquiguil, J. Guimpel, M. Maenhoudt, B. Wuyts, Y. Bruynseraede, M. B. Maple, and I. K. Schuller. *Applied Physics Letters*, 60(17):2159–2161, 1992.

[142] A. Gilabert, R. Cauro, M. G. Medici, J. C. Grenet, H. S. Wang, Y. F. Hu, and Q. Li. *Journal of Superconductivity*, 13(2):285–290, 2000.

[143] R. Cauro, A. Gilabert, J. P. Contour, R. Lyonnet, M. G. Medici, J. C. Grenet, C. Leighton, and I. K. Schuller. *Physical Review B*, 63(17):174423, 2001. Times Cited: 41.

[144] G. Yu, A. J. Heeger, G. Stucky, N. Herron, and E. M. Mccarron. *Solid State Communications*, 72(4):345–349, 1989.

[145] A. I. Kirilyuk, N. M. Kreines, and V. I. Kudinov. *Jetp Letters*, 52(1):49–54, 1990.

[146] A. Hoffmann, D. Reznik, and I. K. Schuller. *Advanced Materials*, 9(3):271, 1997.

[147] V. I. Kudinov, I. L. Chaplygin, A. I. Kirilyuk, N. M. Kreines, R. Laiho, E. Lahderanta, and C. Ayache. *Physical Review B*, 47(14):9017–9028, 1993.

[148] J. F. Federici, D. Chew, B. Welker, W. Savin, J. GutierrezSolana, T. Fink, and W. Wilber. *Physical Review B*, 52(21):15592–15597, 1995.

[149] K. Tanabe, S. Kubo, F. H. Teherani, H. Asano, and M. Suzuki. *Physical Review Letters*, 72(10):1537–1540, 1994.

[150] J. Hasen, D. Lederman, I. K. Schuller, V. Kudinov, M. Maenhoudt, and Y. Bruynseraede. *Physical Review B*, 51(2):1342–1345, 1995.

[151] E. Osquiguil, M. Maenhoudt, B. Wuyts, and Y. Bruynseraede. *Physical Review B*, 49(5):3675–3678, 1994.

[152] V. I. Kudinov, I. L. Chaplygin, A. I. Kirilyuk, N. M. Kreines, R. Laiho, and E. Lahderanta. *Physics Letters A*, 157(4-5):290–294, 1991.

[153] T. Endo, A. Hoffmann, J. Santamaria, and I. K. Schuller. *Physical Review B*, 54(6):R3750–R3752, 1996.

[154] G. Nieva, E. Osquiguil, J. Guimpel, M. Maenhoudt, B. Wuyts, Y. Bruynseraede, M. B. Maple, and I. K. Schuller. *Physical Review B*, 46(21):14249–14252, 1992.

[155] D. Lederman, J. Hasen, I. K. Schuller, E. Osquiguil, and Y. Bruynseraede. *Applied Physics Letters*, 64(5):652–654, 1994.

[156] K. Tanabe, S. Kubo, F. H. Teherani, H. Asano, and M. Suzuki. *Japanese Journal of Applied Physics Part 2-Letters*, 32(2B):L264–L267, 1993.

[157] W. Markowitsch, C. Stockinger, W. Gob, W. Lang, W. Kula, and R. Sobolewski. *Physica C*, 265(3-4):187–193, 1996.

[158] W. Markowitsch, P. Brantner, C. Stockinger, W. Lang, K. Siraj, J. D. Pedarnig, and D. Bauerle. *Journal of Non-Crystalline Solids*, 352(42-49):4500–4504, 2006.

[159] W. Markowitsch, P. Brantner, W. Lang, K. Siraj, A. Moser, and J. D. Pedarnig. *Superconductor Science and Technology*, 21(7):075017, 2008.

[160] W. Markowitsch, W. Lang, J. D. Pedarnig, and D. Bauerle. *Superconductor Science and Technology*, 22(3), 2009.

[161] V. Kiryukhin, D. Casa, J. P. Hill, B. Keimer, A. Vigliante, Y. Tomioka, and Y. Tokura. *Nature*, 386(6627):813–815, 1997.

[162] R. Cauro, J. C. Grenet, A. Gilabert, and M. G. Medici. *International Journal of Modern Physics B*, 13(29-31):3786–3791, 1999.

[163] J. H. Hao, G. G. He, D. X. Lu, and H. K. Wong. *Materials Letters*, 46(4):225–228, 2000.

[164] V. Moshnyaga, A. Giske, K. Samwer, E. Mishina, T. Tamura, S. Nakabayashi, A. Belenchuk, O. Shapoval, and L. Kulyuk. *Journal of Applied Physics*, 95(11):7360–7362, 2004.

[165] X. J. Liu, Y. Moritomo, A. Machida, A. Nakamura, H. Tanaka, and T. Kawai. *Physical Review B*, 63(11):115105, 2001.

[166] Y. G. Zhao, J. J. Li, R. Shreekala, H. D. Drew, C. L. Chen, W. L. Cao, C. H. Lee, M. Rajeswari, S. B. Ogale, R. Ramesh, G. Baskaran, and T. Venkatesan. *Physical Review Letters*, 81(6):1310–1313, 1998.

[167] K. Matsuda, A. Machida, Y. Moritomo, and A. Nakamura. *Physical Review B*, 58(8):R4203–R4206, 1998.

[168] K. Miyano, T. Tanaka, Y. Tomioka, and Y. Tokura. *Physical Review Letters*, 78(22):4257–4260, 1997.

[169] Y. Okimoto, Y. Ogimoto, M. Matsubara, Y. Tomioka, T. Kageyama, T. Hasegawa, H. Koinuma, M. Kawasaki, and Y. Tokura. *Applied Physics Letters*, 80(6):1031–1033, 2002.

[170] H. Katsu, H. Tanaka, and T. Kawai. *Journal of Applied Physics*, 90(9):4578–4582, 2001.

[171] V. Pena, T. Gredig, J. Santamaria, and I. K. Schuller. *Physical Review Letters*, 97(17):177005, 2006.

[172] Z. L. Zhang, U. Kaiser, S. Soltan, H. U. Habermeier, and B. Keimer. *Applied Physics Letters*, 95(24):242505, 2009.

[173] M. Varela, A. R. Lupini, S. J. Pennycook, Z. Sefrioui, and J. Santamaria. *Solid-State Electronics*, 47(12):2245–2248, 2003.